Control of Hox transcription factor concentration and cell-to-cell variability by an auto-regulatory switch

Dimitrios K. Papadopoulos[1,2,*], Kassiani Skouloudaki[1], Ylva Engström[3], Lars Terenius[4], Rudolf Rigler[5,6], Christoph Zechner[1,7], Vladana Vukojević[4] and Pavel Tomancak[1,*]

[1]Max-Planck Institute of Molecular Cell Biology and Genetics, 01307 Dresden, Germany
[2]Current address: MRC Human Genetics Unit, Institute of Genetics and Molecular Medicine, University of Edinburgh, Edinburgh EH4 2XU, UK
[3]Department of Molecular Biosciences, The Wenner-Gren Institute, Stockholm University, 10691 Stockholm, Sweden
[4]Center for Molecular Medicine (CMM), Department of Clinical Neuroscience, Karolinska Institutet, 17176 Stockholm, Sweden
[5]Department of Medical Biochemistry and Biophysics, Karolinska Institutet, 17177 Stockholm, Sweden
[6]Laboratory of Biomedical Optics, Swiss Federal Institute of Technology, 1015 Lausanne, Switzerland
[7]Center for Systems Biology Dresden, 01307, Dresden, Germany

[*]Correspondence: dpapado2@ed.ac.uk and tomancak@mpi-cbg.de

Abstract

The variability in transcription factor concentration among cells is an important developmental determinant, yet how variability is controlled remains poorly understood. Studies of variability have focused predominantly on monitoring mRNA production noise. Little information exists about transcription factor protein variability, since this requires the use of quantitative methods with single-molecule sensitivity. Using Fluorescence Correlation Spectroscopy (FCS), we characterized the concentration and variability of 14 endogenously tagged TFs in live *Drosophila* imaginal discs. For the Hox TF Antennapedia we investigated whether protein variability results from random stochastic events or is developmentally regulated. We found that Antennapedia transitioned from low concentration/high variability early, to high concentration/low variability later, in development. FCS and temporally resolved genetic studies uncovered that Antennapedia itself is necessary and sufficient to drive a developmental regulatory switch from auto-activation to auto-repression, thereby reducing variability. This switch is controlled by progressive changes in relative concentrations of preferentially activating and repressing Antennapedia isoforms, which bind chromatin with different affinities. Mathematical modelling demonstrated that the experimentally supported auto-regulatory circuit can explain the increase of Antennapedia concentration and suppression of variability over time.

Introduction

In order to understand the mechanisms that control pattern formation and cell fate specification in developing organisms, the intranuclear concentration, DNA-binding kinetics and cell-to-cell variability of relevant transcription factors (TFs) need to be quantified. TF concentration variability at the tissue level is thought to arise from

54 diverse processes, including mRNA transcription, translation and protein degradation.
55 For example, transcription in a given tissue is noisy. Intrinsic noise is due to stochastic
56 binding and interactions of proteins involved in transcriptional activation of a specific
57 gene (Blake et al., 2003; Elowitz et al., 2002). Extrinsic noise arises from inter-cellular
58 differences in abundance of the transcriptional and post-transcriptional machinery and
59 affects the efficiency of transcriptional activation in general (Swain et al., 2002).

60 In undifferentiated tissue or cells, TF cell-to-cell variability can be the driving
61 force for differentiation. For example, progressive establishment of a Nanog salt-and-
62 pepper expression pattern leads to the formation of primitive endoderm in the mouse
63 preimplantation embryo, whereas loss of the variability results in embryos lacking
64 primitive endoderm entirely (Kang et al., 2013). In Drosophila, the Senseless (Sens)
65 TF is required for the establishment of the proper number of sensory organ precursors
66 in the ectodermal proneural cluster of cells and unequal Sens concentration among
67 cells is required for their specification (Li et al., 2006). Moreover, variability in
68 concentration (rather than its overall average concentration) of the Yan TF drives the
69 transition of developing photoreceptor cells to a differentiated state during Drosophila
70 eye development (Pelaez et al., 2015).

71 Conversely, in already differentiated tissue or cells, TF expression variability
72 among cells may need to be counteracted to ensure homogeneity of gene expression
73 patterns and robustness of commitment to a certain transcriptional regime. Examples
74 are the Snail (Sna) TF, which is required for the invagination of the mesoderm during
75 Drosophila gastrulation (Boettiger and Levine, 2013), or the Bicoid (Bcd) and
76 Hunchback (Hb) TFs during early embryogenesis (Gregor et al., 2007a; Gregor et al.,
77 2007b; Little et al., 2013). These studies have quantified the tolerable degrees of

concentration variability that allow establishment of gene expression territories with remarkable precision in the developing embryo.

In addition, differential cell fates within the same developmental territory may be specified by TFs deploying different DNA-binding dynamics despite the existence of very similar concentrations (i.e. low variability). For example, studies on the Oct4 TF in early mouse embryos have shown that differential kinetic behavior of DNA binding, despite equal Oct4 concentration among blastomeres, ultimately dictates an early developmental bias towards lineage segregation (Kaur et al., 2013; Plachta et al., 2011).

So far, studies of gene expression variability have focused predominantly on monitoring the noise of mRNA production (Holloway et al., 2011; Holloway and Spirov, 2015; Little et al., 2013; Lucas et al., 2013; Pare et al., 2009). Little information exists about TF variability at the protein level within a tissue. Such studies require the use of quantitative methods with single-molecule sensitivity.

We have previously used fluorescence microscopy and Fluorescence Correlation Spectroscopy (FCS), to quantitatively characterize Hox TF interactions with nuclear DNA in living salivary gland cells (Papadopoulos et al., 2015; Vukojevic et al., 2010). FCS has also been instrumental for quantifying TF dynamics in living cells or tissue (Clark et al., 2016; Kaur et al., 2013; Lam et al., 2012; Mistri et al., 2015; Papadopoulos et al., 2015; Perez-Camps et al., 2016; Szaloki et al., 2015; Tiwari et al., 2013; Tsutsumi et al., 2016). However, in these studies, mobility has only been measured for overexpressed proteins. However, to understand TF behavior *in vivo*, proteins need to be quantified at endogenous levels (Lo et al., 2015).

In this study, we take advantage of the availability of fly toolkits, in which TFs have been endogenously tagged by different methodologies: fosmid (Baumgartner et

103 al., 1996), BAC (deposition of lines of Rebecca Spokony and Kevin White to Flybase
104 and the Bloomington Stock Center), FlyTrap (Buszczak et al., 2007; Kelso et al., 2004;
105 Morin et al., 2001; Quinones-Coello et al., 2007) and MiMIC lines (Nagarkar-Jaiswal
106 et al., 2015; Venken et al., 2011), to measure the intranuclear concentration of various
107 TFs *in vivo* by FCS, and their cell-to-cell variability in fly imaginal discs. Imaginal discs
108 are flat, single-layered epithelia comprised of small diploid cells and many TFs are
109 expressed in defined regions within these tissues during development. Here, we found
110 that Antp, a well-characterized homeotic selector gene, responsible for specification
111 of thoracic identity in fly tissues, displays high cell-to-cell variability during early disc
112 development and this variability was suppressed at later developmental stages.
113 Through a combination of genetics, single-molecule measurements of TF dynamics
114 by FCS and mathematical modeling, we uncovered a mechanism that controls Antp
115 concentration and variability in developing discs.
116
117 **Results**
118
119 Characterization of average protein concentrations and cell-to-cell variability of
120 *Drosophila* TFs
121 Average concentrations of TFs in neighboring nuclei of third instar imaginal
122 discs were measured by FCS (Fig. 1A-J and Supplemental Fig. S1A-P). FCS is a non-
123 invasive method with single molecule sensitivity, in which a confocal arrangement of
124 optical elements is used to generate a small (sub-femtoliter) detection volume inside
125 living cells, from which fluorescence is being detected (Fig. 1C,D; green ellipsoid).
126 Fluorescent molecules diffuse through this observation volume, yielding fluorescence
127 intensity fluctuations that are recorded over time by detectors with single-photon

128 sensitivity (Fig. 1E). These fluctuations are subsequently subjected to temporal
129 autocorrelation analysis, yielding temporal autocorrelation curves (henceforth referred
130 to as FCS curves, Fig. 1F), which are then fitted with selected models to extract
131 quantitative information about the dynamic processes underlying the generation of the
132 recorded fluctuations. In the case of molecular movement of TFs (Supplement 1),
133 information can be obtained regarding: a) the absolute TF concentrations (Fig. 1F), (b)
134 TF dynamic properties, such as: diffusion times, differences in their interactions with
135 chromatin and fractions of free-diffusing *versus* chromatin-bound TFs (Fig. 1G); and
136 c) cell-to-cell TF concentration variability (Fig. 1H).

137 We selected 14 TF based on the availability of homozygous, endogenously
138 tagged transgenes and generation of robust fluorescence in distinct patterns in various
139 imaginal discs. For the 14 TFs, we measured average concentrations ranging about
140 two orders of magnitude among different TFs, from $\sim 30\ nM$ to $\sim 1.1\ \mu M$ (~400 to 15500
141 molecules per nucleus, respectively) (Fig. 1I, Supplemental Fig. S1A-Q and
142 Supplement 2). We also obtained various diffusion times and fractions of slow and fast
143 diffusing TF molecules (Fig. 1J), indicating differential mobility and degree of DNA-
144 binding among different TFs (Vukojevic et al., 2010). Comparison of the y-axis
145 amplitudes at the zero lag time of the FCS curves, which are inversely proportional to
146 the concentration of fluorescent molecules (Fig. 1F), gives information about
147 concentration variability (heterogeneity) among different cell nuclei, i.e. reflects
148 heterogeneity of protein concentration at the tissue level (Fig. 1H). For all 14 TFs
149 studied, the variability, expressed as the variance over the mean squared, $CV^2 = \frac{s^2}{m^2}$,
150 was determined to be in the range $7 - 37\%$ (Fig. 1K and Supplemental Fig. S1Q).

151 In biological systems, the Fano factor, expressed as the variance over the mean
152 ($F_f = \frac{s^2}{m}$, in concentration units), is a commonly used index to quantify variability. It has

153 been proposed that Fano factor values that increase with average concentrations
154 indicate that the underlying transcriptional processes cannot be sufficiently explained
155 by a simple one-step promoter configuration with purely intrinsic Poissonian noise and
156 that extrinsic noise is likely to contribute significantly to the overall variability (Newman
157 et al., 2006; Schwanhausser et al., 2011; Taniguchi et al., 2010). For all TFs
158 measured, Fano factor values from 0 to 20 were obtained (Supplemental Fig. S1R), in
159 line with Fano factor values of other TFs determined previously to lie between 0 and
160 30 (Sanchez et al., 2011). Moreover, the majority of TFs examined show Fano factor
161 values, $\mathrm{F_f} > 1$, suggesting that transcriptional bursting is likely to be a significant
162 source of the observed cell-to-cell variability. For Eyeless, the Fano factor value $\mathrm{F_f} \approx$
163 1 suggests that the transcription of this gene is likely to be a continuous process that
164 occurs with a constant probability and according to the statistics of a Poisson process.
165 In contrast, Salm, which was the only TF characterized by $\mathrm{F_f} < 1$, exhibits a pattern of
166 occurrence that is more regular than the randomness associated with a Poissonian
167 process. We used this dataset as a starting point for studying the control of variability
168 during imaginal disc development.

169 The average concentration and variability of the investigated TFs showed no
170 obvious interdependence (Fig. 1K), suggesting that if variability is controlled, there is
171 not one control mechanism that is common to all investigated TFs. Among the studied
172 TFs, the Hox protein Antennapedia (Antp), showed low variability ($CV^2 < 0.2$) in high
173 average concentrations, in particular in the leg disc (Fig. 1K). Since low variability at
174 the tissue level is likely to be achieved through regulatory mechanisms, we
175 investigated Antp variability further by FCS. Because FCS performs best at low to
176 moderate expression levels (Supplement 1), we performed this analysis in the wing
177 disc where expression levels are lower than in the leg disc (Fig. 1K,L). We first

178 established that the observed fluorescence intensity fluctuations were caused by
179 diffusion of TF molecules through the detection confocal volume (Supplemental Fig.
180 S2 and Supplement 1). FCS showed that different clusters of neighboring cells along
181 the Antp expression domain in the wing disc display different average expression
182 levels (Fig. 1L). Moreover, FCS showed that Antp cell-to-cell variability decreased with
183 increasing Antp concentration (Fig. 1M) whereas the Fano factor increased
184 (Supplemental Fig. S1R). Such behavior is indicative of complex transcriptional
185 regulatory processes (Franz et al., 2011; Smolander et al., 2011) that we further
186 investigated using the powerful *Drosophila* genetic toolkit.
187
188 Control of Antp concentration by transcriptional auto-regulation
189 One mechanism by which genes control their expression level variability is
190 auto-regulation (Becskei and Serrano, 2000; Dublanche et al., 2006; Gronlund et al.,
191 2013; Nevozhay et al., 2009; Shimoga et al., 2013; Thattai and van Oudenaarden,
192 2001). To test whether Antp can regulate its own protein levels, we monitored the
193 concentration of endogenous Antp protein upon overexpression of *Antp* from a
194 transgene. To distinguish between overexpressed and endogenous protein, we used
195 synthetic Antp (SynthAntp) transgenes fused to eGFP (SynthAntp-eGFP). These
196 transgenes encode the Antp homeodomain, the conserved YPWM motif and the C
197 terminus (but lack the long and non-conserved N terminus of the protein, against which
198 widely used Antp antibodies have been raised) and they harbor Antp-specific homeotic
199 function (Papadopoulos et al., 2011). Clonal overexpression of *SynthAntp-eGFP* in the
200 wing disc notum (Fig. 2A-B' and controls in Supplemental Fig. S3D,D') repressed the
201 endogenous Antp protein, indicating that Antp is indeed able to regulate its own protein
202 levels.

203 Since Antp is a TF, we next asked whether the auto-repression indeed occurs
204 at the transcriptional level. The *Antp* locus is subject to complex transcriptional
205 regulation, involving a distal and a proximal promoter (P1 and P2 promoters,
206 respectively), spanning more than 100 kb of regulatory sequences. We established
207 that the P1 promoter (rather than the P2 promoter) is predominantly required to drive
208 expression of Antp in the wing disc notum (Supplemental Fig. S3A-C'), in line with
209 previous observations ((Engstrom et al., 1992; Jorgensen and Garber, 1987; Zink et
210 al., 1991) and Materials and Methods). Moreover, mitotic recombination experiments
211 in regions of the wing disc unique to P2 transcription have shown no function of the
212 P2 promoter transcripts in wing disc development (Abbott and Kaufman, 1986). Thus,
213 the P1 Antp reporter serves as a suitable reporter of the *Antp* locus transcriptional
214 activity in this context.

215 Clonal overexpression of SynthAntp-eGFP in the wing disc repressed the *Antp*
216 P1 transcriptional reporter (Fig. 2C,C' and controls in Supplemental Fig. S3E,E'). To
217 rule out putative dominant negative activity of the small SynthAntp-eGFP peptide, we
218 also performed these experiments with the full-length Antp protein (Supplemental Fig.
219 S3F,F'). We conclude that the Antp protein is able to repress its own transcription from
220 the P1 promoter, suggesting a possible mechanism of suppressing cell-to-cell
221 variability of *Antp* expression levels (Fig. 2D).

222 In the course of these experiments, we noticed that ectopic overexpression of
223 *SynthAntp-eGFP* or the full-length Antp protein from the *Distal-less* (*Dll*) (MD23)
224 enhancer resulted in activation of the *Antp* P1 reporter in distal compartments of the
225 wing disc, such as the wing pouch, where Antp is normally not detected (Fig. 2E-F'
226 and controls in Supplemental Fig. S3G-H'). This suggests that next to its auto-
227 repressing function, Antp is also capable of activating its own transcription (Fig. 2G).

228 To exclude that the auto-activation and repression of Antp are artifacts of
229 overexpression, we used FCS to measure the concentration of Antp triggered by
230 different Gal4-drivers (Supplemental Fig. S4A-E). We observed indistinguishable
231 DNA-binding behavior by FCS, not only across the whole concentration range
232 examined (Supplemental Fig. S4F), but also between endogenous and overexpressed
233 Antp (Supplemental Fig. S5A,B). Importantly, the auto-activating and auto-repressing
234 capacity of Antp was preserved even with the weak Gal4-driver *69B* (Supplemental
235 Fig. S4K,L) that triggered concentrations of Antp lower than its normal concentration
236 in the leg disc ($473\,nM$ versus $1110\,nM$), indicating that auto-activation and auto-
237 repression of Antp take place at endogenous protein concentrations.
238 We conclude that Antp is able to repress and activate its own transcription (Fig.
239 2D,G) and hypothesize that this auto-regulatory circuit sets the correct concentration
240 of Antp protein in imaginal discs.
241
242 <u>A temporal switch controls the transition of *Antp* from a state of auto-activation to a</u>
243 <u>state of auto-repression</u>
244 To further investigate the mechanism by which the Antp auto-regulatory circuit
245 sets the precise Antp expression levels, we next asked whether the seemingly
246 opposing auto-regulatory activities of Antp are separated in time during development.
247 To that end, we induced gain-of-function clones of full-length untagged *Antp* either at
248 26 h (first larval instar – henceforth referred to as “early” stage) or at 60 h (late second
249 larval instar – henceforth referred to as “late” stage) of development and analyzed the
250 clones in late third instar wing imaginal discs (Fig. 3). As a pre-requisite for this
251 analysis, we established that the Antp-eGFP homozygous viable MiMIC allele
252 recapitulates the endogenous Antp pattern in the embryo and all thoracic imaginal

253 discs and therefore can be used to monitor endogenous Antp protein (Supplemental
254 Fig. S6). Clonal induction of full-length untagged *Antp* in early development triggered
255 strong auto-activation of Antp-eGFP (Fig. 3A,B,B' and controls in Supplemental Fig.
256 S7A-C'). As before, we confirmed that early auto-activation of Antp is transcriptional
257 and similar for both full-length and SynthAntp proteins (Supplemental Fig. S7D-E' and
258 controls in F-G'). Early auto-activation was further supported by a loss-of-function
259 experiment, where *RNAi*-mediated early knockdown of Antp resulted in
260 downregulation of the Antp reporter (Fig. 3C,C' and controls in Supplemental Fig.
261 S7H,H'). The loss and gain-of-function analysis together suggest that during early disc
262 development Antp is required for sustaining its own expression.

263 In contrast, clonal induction during the late second instar stage (Fig. 3F)
264 repressed Antp-eGFP (Fig. 3G,G') and, reciprocally, the clonal knockdown by *RNAi*
265 triggered auto-activation of Antp transcription (Fig. 3H,H'). Hence, in contrast to early
266 development, Antp represses its own expression in third instar discs.

267 While the gain-of-function experiments show that Antp is sufficient to execute
268 auto-regulation, loss-of-function analysis indicates that it is also necessary for both
269 repression and activation at the transcriptional level.

270 Together, these results revealed the existence of a switch in Antp auto-
271 regulatory capacity on its own transcription during development. Starting from a
272 preferentially auto-activating state early in development (Fig. 3D), Antp changes to an
273 auto-inhibitory mode at later developmental stages (Fig. 3I).

274

275 <u>During development Antp switches from a low-concentration/high-variability to a high-</u>
276 <u>concentration/low-variability state</u>

277 If the *Antp* auto-repressive state limits the variability of Antp protein
278 concentration among neighboring cells late in development, we expected that the
279 variability would be higher during earlier stages, when auto-repression does not
280 operate. We, therefore, used FCS to characterize the endogenous expression levels
281 and cell-to-cell variability of Antp concentration in nuclei of second instar wing and leg
282 discs. We observed significantly lower average concentrations of Antp protein in
283 second versus third instar wing and leg discs and the inverse was true for
284 concentration variability (Fig. 3E and Supplemental Fig. S8A,A',C), indicating that the
285 developmental increase in concentration is accompanied by suppression of
286 concentration variability. In addition, FCS revealed a notable change in Antp
287 characteristic decay times (signifying molecular diffusion, limited by chromatin-
288 binding) at early versus late stages (Supplemental Fig. S8B). This behavior indicates
289 that endogenous Antp is initially moving fast in the nucleus, as it undergoes
290 considerably fewer interactions with chromatin compared to later stages where its
291 interactions with chromatin are more frequent and longer lasting.

292 Taken together, our FCS measurements show that *Antp* is expressed at
293 relatively low and highly variable levels in early developing discs, when genetic
294 evidence indicates auto-activation capacity on its own transcription. Later in
295 development, when Antp has reached a state of higher average concentrations, auto-
296 repression kicks in, resulting in considerably lower variability among neighboring cells.
297

298 <u>Dynamic control of Antp auto-regulation by different Antp isoforms</u>

299 The changing binding behavior of Antp on chromatin from second to third instar
300 discs and the developmental transition from an auto-activating to an auto-repressing
301 state suggested a causal relationship between the two phenomena. We, therefore,

302 sought to identify molecular mechanisms that could link the observed changes in Antp
303 chromatin-binding to Antp auto-activation and repression. It is well established that the
304 Antp mRNA contains an alternative splice site in exon 7 immediately upstream of the
305 homeobox-containing exon 8, and generates Antp isoforms differing in as little as 4
306 amino acids in the linker between the YPWM motif (a cofactor-interacting motif) and
307 the homeodomain (Fig. 4A) (Stroeher et al., 1988). Our previous observation that long
308 linker isoforms favor transcriptional activation of Antp target genes, whereas short
309 linker isoforms favor repression of Antp targets (Papadopoulos et al., 2011), prompted
310 us to examine whether the linker length is also responsible for differences in auto-
311 regulation.

312 Ectopic expression of SynthAntp-eGFP peptides featuring a long linker
313 displayed significantly weaker repression capacity on endogenous Antp, as compared
314 to their short linker counterparts (Fig. 4B,B',F,F' and quantified in D,H, see also
315 Materials and Methods). We confirmed that, also in this case, the repression was at
316 the transcriptional level (Supplemental Fig. S9I-J'). Inversely, long linker Antp isoforms
317 exhibited stronger activation of Antp reporter, as compared to short linker isoforms
318 (Fig. 4C,C',G,G' and quantified in D,H; see also Materials and Methods). We,
319 additionally, validated that short linker isoforms encoded by full-length or SynthAntp
320 cDNAs behaved as weaker auto-activating and stronger auto-repressing Antp species
321 in all our previous experiments using the endogenous Antp protein and the P1 reporter
322 (Supplemental Fig. S9A-H'). We conclude that, also in the case of Antp auto-
323 regulation, short linker isoforms function as more potent repressors, whereas long
324 linker ones operate as more potent activators.

325 Since the Antp P1 promoter undergoes a swich from preferential auto-activation
326 to auto-repression, and short and long linker Antp isoforms function as preferential

327 auto-repressors and auto-activators, respectively, it appeared possible that the switch
328 in Antp regulation is executed at the level of transcript variant abundance of these
329 isoforms. Therefore, we next quantified the relative abundance of long and short linker
330 transcript variants in the embryo, second and third instar discs (Fig. 4D,H). The data
331 showed that the abundance of the long linker variant decreased, whereas the
332 abundance of the short linker variant increased over time in development, in line with
333 previous observations (Stroeher et al., 1988). Thus, as hypothesized, this finding
334 suggested that relative transcript variant abundance may underlie the switch between
335 auto-activation and auto-repression (without excluding additional mechanisms, such
336 as changes in the chromatin modifications between early and later disc development,
337 or the participation of different cofactors).

338 Relative changes in Antp transcript variant abundance (Fig. 4D,H), differential
339 efficiency of their encoded isoforms to repress or activate the *Antp* gene (Fig. 4B-D,F-
340 H), the developmental switch of *Antp* from auto-activation to repression (Fig. 3) and
341 the different mobility of Antp between second and third instar imaginal discs (Fig. 3E)
342 all pointed towards the hypothesis that the two isoforms have different modes of
343 interaction with chromatin. To investigate this, we expressed the two isoforms from the
344 *69B* enhancer in third instar wing and antennal discs. This results in Antp
345 concentrations close to (if not below) endogenous levels (Supplemental Fig. S4A-J).
346 FCS measurements revealed that the short linker isoform displayed longer
347 characteristic decay times and a higher fraction of DNA-bound molecules, suggesting
348 stronger and more pronounced binding to chromatin than its long linker counterpart
349 (Fig. 4D,H and Supplemental Fig. S10A,B). With chromatin (and therefore Antp
350 binding sites configuration), as well as the presence of cofactor proteins, being
351 identical between the two instances (short and long linker isoforms examined in third

352 instar wing and antennal imaginal discs of the same age), we were able to directly
353 compare the apparent equilibrium dissociation constants for the two isoforms
354 (Supplement 3). We found that the affinity of binding to chromatin ($K_d{}^{-1}$) of the
355 repressing short linker isoform is at least 2.3 times higher compared to the activating
356 long linker isoform ($\frac{K_{d,Antp}^{long\ linker\ isof.}}{K_{d,Antp}^{short\ linker\ isof.}} > 2.3$) (Fig. 4D,H and Supplemental Fig. S10C-D').
357 Collectively, these experiments support the notion that differences in Antp regulation
358 during disc development can be largely attributed to differences in the affinity of the
359 investigated Antp isoforms.

360 Taken together, the switch of Antp from an auto-activating to an auto-repressing
361 state and the alteration of its DNA-binding behavior during disc development can be
362 largely explained by a temporal developmental regulation of the relative
363 concentrations of preferentially auto-activating and auto-repressing Antp protein
364 isoforms, which themselves display distinct properties in their modes of interaction
365 with chromatin (Fig. 4E,I).

366

367 Robustness of Antp auto-regulation

368 The mechanism of developmental Antp auto-regulation offered a possible
369 explanation for the observed increase in Antp concentration from second to third instar
370 discs, as well as the suppression of variability. What remained an open question is the
371 functional significance of suppression of Antp variability in development. In order to
372 test this in development, we require the means to manipulate variability, yet such
373 manipulation is currently hard to achieve at the endogenous locus. However, since
374 average concentration and variability are interdependent, we were able to use an
375 ectopic expression system to progressively dampen Antp variability by manipulating
376 its concentration. To this end, we expressed SynthAntp ectopically in the antennal

377 disc, devoid of endogenous Antp expression, and monitored the extent (strength) of
378 homeotic transformations induced by different Gal4 drivers corresponding to different
379 SynthAntp concentrations (as measured by FCS previously in Supplemental Fig. S4A-
380 D). In this case, expression of SynthAntp is controlled by the Gal4 driver,
381 independently of the Antp locus, therefore the phenotypic output does not depend on
382 Antp auto-regulation. We observed that partial transformations of antennae to tarsi
383 could be obtained with drivers expressing Antp at close to endogenous concentration
384 (*ptc*-Gal4, *Dll*-Gal4 (MD713) and *69B*-Gal4 drivers, Fig. 5B-D and Supplemental Fig.
385 S4B-D). This indicates that Antp is able to repress the antennal and launch the leg
386 developmental program in the antennal disc at endogenous concentrations, although
387 not in a robust manner across the tissue. As expected, the three weak transformation
388 phenotypes, elicited by *ptc*-, *Dll* (MD713)- and *69B*-Gal4 (Fig. 5B-D) were
389 accompanied by high variability of SynthAntp concentration in developing discs (Fig.
390 5E,F). In contrast, strong expression of SynthAntp from the *Dll*-Gal4 (MD23) enhancer
391 resulted in robust homeotic transformation to a complete tarsus (Fig. 5A) and was
392 accompanied by low cell to cell variability (Fig. 5F). This condition resembled most
393 closely the endogenous Antp variability in the leg disc ($CV^2 = 0.103$). Importantly,
394 endogenous Antp and Antp overexpressed by any of the Gal4 drivers showed
395 indistinguishable chromatin-binding behavior by FCS (Supplemental Fig. S4F and
396 Supplemental Fig. S5A,B).

397 These results suggest that robust Antp homeotic function can be achieved at
398 concentrations that are accompanied by low variability.

399 In order to further substantiate the qualitative model of Antp auto-regulation
400 suggested by our experimental findings and to examine its impact on protein
401 variability, we developed a simple mathematical model of stochastic *Antp* expression.

402 This model tests whether the identified interplay between positive and negative auto-
403 regulation of Antp through distinct isoforms is sufficient to explain the increase in
404 protein concentration and decrease in nucleus-to-nucleus variability from early to late
405 stages. The model consists of a dynamic promoter, which drives transcription of *Antp*
406 followed by a splicing step, leading to the expression of either the auto-repressing or
407 the auto-activating isoform of Antp. In line with our finding that the repressing isoform
408 has higher concentration at later stages, we assumed that splicing is more likely to
409 generate this isoform than the activating isoform. The initial imbalance of Antp towards
410 the activating isoform (Fig. 4D,H) is modeled through appropriate initial concentrations
411 of each isoform.

412 Since Antp copy numbers per nucleus are in the thousands at both early and
413 late stages, intrinsic noise of gene expression is likely to explain only a certain portion
414 of the overall variability in Antp concentrations (Elowitz et al., 2002; Taniguchi et al.,
415 2010). The remaining part (termed extrinsic variability) is due to cell-to-cell differences
416 in certain factors affecting gene expression such as the ribosomal or ATP abundances.
417 To check whether extrinsic variability significantly affects Antp expression, we
418 expressed nuclear mRFP1 constitutively, alongside with endogenous Antp and
419 measured the abundances of green-labeled Antp and mRFP1 (Supplemental Fig.
420 S11). Since extrinsic factors are expected to affect both genes in a similar way, one
421 should observe a correlation between the concentration of nuclear mRFP1 and Antp-
422 eGFP. Our data showed a statistically significant correlation between mRFP1 and
423 Antp (Supplemental Fig. S11C, $r = 0.524$ and $p = 9.77 \cdot 10^{-5}$). Correspondingly, we
424 accounted for extrinsic variability also in our model by allowing gene expression rates
425 to randomly vary between cells (Zechner et al., 2012).

426 The promoter itself is modeled as a Markov chain with three distinct
427 transcriptional states. In the absence of Antp, the promoter is inactive and transcription
428 cannot take place (state “U” in Fig. 5G). From there, the promoter can switch into a
429 highly expressing state “A” at a rate that is assumed to be proportional to the
430 concentration of the long-linker, auto-activating isoform (Antp-A, Fig. 5G). This
431 resembles the positive auto-regulatory function of Antp. Conversely, the promoter can
432 be repressed by recruitment of the short-linker, auto-repressing isoform,
433 corresponding to state “R” in the model (Antp-R, Fig. 5G). Since the auto-repressing
434 isoform of Antp can also activate the promoter, albeit significantly weaker than the
435 auto-activating isoform, and vice versa, we allow the promoter to switch between
436 states “A” and “R”.

437 While this promoter model resembles the dual-feedback structure of *Antp* locus
438 inferred from experiments, it is unclear whether the two isoforms compete for the same
439 binding sites on the P1 promoter or if auto-repression can take place regardless of
440 whether an activating isoform is already bound to the promoter. In the former case, an
441 increase in concentration of repressing Antp species enhances the probability to reach
442 state “R” only if the promoter is in state “U” (Fig. 5G). In the latter case, the rate of
443 switching between “A” and “R” also depends on the concentration of repressing
444 isoforms of Antp (Fig. 5G, compared to Supplemental Fig. S12A). We analyzed both
445 model variants by forward simulation and found that both of them can explain the
446 switch-like increase in average Antp concentration between early and late stages (Fig.
447 5J, compared to Supplemental Fig.S12D), as well as the relative fraction of repressing
448 and activating isoforms (Fig. 5I, compared to Supplemental Fig. S12C). However, only
449 the non-competitive binding model (Fig. 5G) can explain the substantial reduction of
450 total Antp variability between early and late stages (Fig. 5J), whereas in the

451 competitive model variability is not reduced (Supplemental Fig. S12D). Simulation
452 trajectories of individual nuclei indicated an initial increase and a subsequent
453 stabilization of concentration, whereas in the competitive model, or in the absence of
454 the negative feedback, this is not achieved (Fig. 5H, compared to Supplemental Fig.
455 S12B,F). Additionally, we established that the negative feedback is required for
456 suppression of variability (Supplemental Fig. S12E,H), since without this, no
457 suppression of variability is conferred (Supplemental Fig. S12H). Thus, the model
458 suggested that auto-repression is required and it is possible also if an activating
459 isoform of Antp is already bound to the P1 promoter. Correspondingly, we use the
460 non-competitive promoter model for further analyses.

461 To further validate this model, we analyzed how Antp variability scales with
462 average concentrations and compared it to our experimental measurements. To
463 generate different average concentrations, we varied the gene expression rates over
464 three orders of magnitude and calculated the corresponding variability. The model
465 predicted a decrease in variability as a function of total Antp concentration and an
466 increase in the Fano factor. These findings are in good agreement with the
467 experimental data (compare Fig. 5K to K' and L to L').

468 We next analyzed the model behavior under different genetic perturbations.
469 Increase of Antp concentration by overexpressing SynthAntp transgenes (bearing
470 either a long or a short linker isoform) from the Antp P1 promoter (Antp P1-Gal4>UAS-
471 SynthAntp-eGFP long or short linker) resulted in 100% embryonic lethality, rendering
472 the analysis of concentration and variability in imaginal discs impossible. This
473 indicated that indiscriminate increase of the dosage of either Antp variant from early
474 embryonic development onwards cannot be tolerated or buffered by the auto-
475 regulatory circuit.

476 However, overexpression from a *Dll* enhancer [*Dll*-Gal4 (MD23)] in the leg discs
477 or in the notum (*MS243*-Gal4), which overlaps with the endogenous Antp expression
478 pattern only during first instar disc development (Emerald and Cohen, 2004), resulted
479 in normal adult leg and notum structures. Flies overexpressing either the SynthAntp
480 auto-activating or the auto-repressing isoform in distal appendages (Fig. 6A,B) or the
481 notum (Supplemental Fig. S13A) displayed the wild type morphology, indicative of
482 normal Antp function, regardless of which isoform (activating or repressing) was
483 overexpressed. To understand this observation, we measured by FCS the
484 concentration and variability of the total Antp protein (endogenous Antp-eGFP and
485 overexpressed SynthAntp-eGFP) in proximal regions of the leg disc at second and
486 third instar stages (Fig. 6C,C'). We found that, while the concentration remained high
487 at early and later stages due to the overexpression, variability was reduced to
488 endogenous levels at late stages. Also, the reduction of Antp variability does not seem
489 to depend on its concentration alone, because for high concentrations at both early
490 and late stages, variability is high only in the early stage and reduced in the late stage.
491 Taken together, the phenotypic analysis and FCS measurements indicate that
492 Antp auto-regulation is able to reduce variability, even at high levels of expression of
493 either isoform, ensuring proper leg development.
494 The experimental data were corroborated by the model, which predicted that
495 more than three-fold overexpression of either auto-activating or auto-repressing Antp
496 isoforms will nevertheless equilibrate to normal expression levels at later stages (Fig.
497 6D,F,G,I). Specifically, we have measured by FCS roughly 15400 molecules in the
498 wild type leg disc, and the model is in good quantitative agreement with this
499 measurement upon overexpression of the activating or repressing isoform. In addition,
500 there is no negative effect on the noise suppressing property of the circuit (Fig. 6F,I).

501 Thus, both the model and experimental data indicate that transient high levels of either
502 isoform early during disc development can be tolerated and that the concentration and
503 cell-to-cell variability of the endogenous Antp protein is restored at later stages.

504 In contrast, overexpression of an exogenous repressor, such as Sex combs
505 reduced (Scr), which can repress Antp at the transcriptional level, but can neither
506 activate it nor activate its own transcription (Supplemental Fig. S13E-J'), resulted in
507 abnormal leg (Fig. 6J) and notum (Supplemental Fig. S13B) development. These flies
508 died as pharate adults with malformed legs that did not allow them to hatch from the
509 pupal case, in line with Antp being required for proper leg development in all ventral
510 thoracic discs (legs). FCS measurements in the corresponding proximal leg disc cell
511 nuclei of second and third instar leg discs overexpressing mCherry-SynthScr revealed
512 a pronounced reduction in Antp concentration and a remarkable increase in variability
513 (Fig. 6K). In line with these observations, the model predicted a similar block of
514 transcription and correspondingly severe effects on Antp dynamics (Fig. 6L-N). In both
515 the measurements and the model prediction, the high increase in variability was
516 triggered by the fact that a majority of the cells do not manage to switch into the highly-
517 expressing state since too few long-linker Antp molecules are present to establish the
518 positive auto-regulation. Since splicing favors the short-linker isoforms at later stages,
519 these cells never "recover" from Scr repression after restriction of the Antp
520 overexpression domain to proximal regions of the leg disc (Fig. 6L).

521 Taken together, the minimal model of Antp auto-regulatory genetic circuit is
522 able to explain the experimentally observed differences in Antp concentration and cell-
523 to-cell variability at early and late developmental stages.

524

525 **Discussion**

526 In this work, we have characterized the endogenous molecular numbers
527 (concentration) and cell-to-cell variability in concentration of 14 TFs in *Drosophila*
528 imaginal discs by FCS. We have identified Antp as a TF displaying low variability
529 among cells. We used genetics, FCS and mathematical modeling to quantitatively
530 characterize Antp behavior in live imaginal discs and identified a kinetic mechanism
531 responsible for the suppression of variability in the third instar discs compared to
532 earlier developmental stages. We found that *Antp* can auto-regulate its expression
533 levels during the course of development, starting from a preferentially auto-activating
534 state early in development and transitioning to a preferentially auto-repressing state
535 later. The early state is characterized by lower average Antp concentrations and high
536 variability, whereas the opposite is true for the later repressing state. Without excluding
537 other mechanisms, such as chromatin configuration, accessibility of Hox binding sites
538 to Antp, the differential abundance of cofactors among developmental stages, or
539 different modes of interactions with different Antp isoforms, we have shown that
540 differential expression of Antp isoforms is one contributing mechanism for the
541 observed regulatory switch. These isoforms have preferentially activating or
542 repressing activities on the Antp promoter, bind chromatin with different affinities and
543 are themselves expressed in different relative amounts during development. A loss-
544 of-function analysis of the isoforms *in vivo* will be required to provide a definitive
545 answer on the relative contribution of the Antp isoform-mediated auto-regulatory circuit
546 towards observed suppression of variability. CRISPR/Cas9-mediated genome
547 manipulation, in principle, allows the generation of Antp loci that express only one or
548 the other isoform. However, it is not clear whether these flies can reach the larval
549 developmental stages, given the Antp embryonic functions and, in fact, strong biases
550 towards only the activating or repressing isoform introduced by Antp-Gal4-mediated

551 expression of either Antp isoform resulted in embryonic lethality. In the absence of
552 such direct evidence, we turned to mathematical modelling and derived, based on our
553 experimental data, a simple kinetic model of *Antp* auto-regulation that confirmed the
554 plausibility of the proposed mechanism. In addition, the model generated predictions
555 that could be verified by introducing genetic perturbations.

556 Negative auto-regulation has been identified as a frequently deployed
557 mechanism for the reduction of noise (cell-to-cell variability) and the increase of
558 regulatory robustness in various systems (Becskei and Serrano, 2000; Dublanche et
559 al., 2006; Gronlund et al., 2013; Nevozhay et al., 2009; Shimoga et al., 2013; Thattai
560 and van Oudenaarden, 2001). Auto-repression has been described for the Hox gene
561 *Ultrabithorax* (*Ubx*) in haltere specification and as a mechanism of controlling Ubx
562 levels against genetic variation (Crickmore et al., 2009; Garaulet et al., 2008), as well
563 as in *Ubx* promoter regulation in Drosophila S2 cells (Krasnow et al., 1989). In contrast,
564 an auto-activating mechanism is responsible for the maintenance of *Deformed*
565 expression in the embryo (Kuziora and McGinnis, 1988). Moreover, global auto-
566 regulation of *Hox* gene complexes has been shown to be in effect also in mammalian
567 limb development (Sheth et al., 2014). These experiments point to evolutionarily
568 conserved mechanisms for establishing (auto-activation) or limiting (auto-repression)
569 Hox TF levels and variability in different developmental contexts.

570 Our data suggest that the developmental switch from auto-activation to auto-
571 repression is, at least in part, mediated by molecularly distinct Antp linker isoforms.
572 Differences in affinities of different Hox TF isoforms, based on their linker between the
573 YPWM motif and the homeodomain, have also been identified for the Hox TF Ubx.
574 Interestingly, its linker is also subject to alternative splicing at the RNA level (Reed et
575 al., 2010). In a similar way to Antp, the long linker Ubx isoform displays four to five fold

576 lower affinity of DNA binding, as compared to short linker isoforms, and the two
577 isoforms are not functionally interchangeable in *in vivo* assays. Finally, the Ubx linker
578 also affects the strength of its interaction with the Hox cofactor Extradenticle (Exd),
579 underscoring the functional importance of linker length in Hox TF function (Saadaoui
580 et al., 2011). Thus, protein isoform control might represent a common regulatory
581 mechanism of Hox-mediated transcriptional regulation.

582 Mathematical modeling predicts that the Antp auto-regulatory circuit is robust
583 with respect to initial conditions and extrinsic noise by being able to suppress cell-to-
584 cell concentration variability even at high concentrations of any of the two Antp
585 isoforms (auto-repressing or auto-activating). This "buffering" capacity on cell-to-cell
586 variability is reflected in the ability of flies to tolerate more than 3-fold overexpression
587 of Antp without dramatic changes in endogenous Antp levels or generation of
588 abnormal phenotypes. Therefore, two different isoforms produced from the same gene
589 with opposing roles in transcriptional regulation and different auto-regulatory binding
590 sites on the gene's promoter seem to suffice to create a robust gene expression circuit
591 that is able to "buffer" perturbations of the starting conditions.

592 So far, we have only been able to indiscriminately increase or decrease Antp
593 concentration at the tissue level and record the phenotypic outcome of these boundary
594 states. It will be interesting to test whether controlled perturbations of TF variability at
595 the tissue level that render TF concentration patterns less or more noisy among
596 neighboring cells, lead to abnormal phenotypes. The technology to selectively
597 manipulate expression variability of specific TF in a developing tissue is yet to be
598 established.

599

600 **Materials and Methods**

601

602 Fly stocks used

603 The Antp-eGFP MiMIC line has been a kind gift from Hugo J. Bellen
604 (Bloomington stock 59790). The *atonal* (VDRC ID 318959), *brinker* (VDRC ID
605 318246), *spalt major* (VDRC ID 318068), *yorkie* (VDRC ID 318237), *senseless* (VDRC
606 ID 318017) and *Sex combs reduced* (VDRC ID 318441) fosmid lines are available
607 from the Vienna Drosophila Resource Center (VDRC) and have been generated
608 recently in our laboratory (Sarov et al., 2016). The *fork head* (stock 43951), *grainy*
609 *head* (stock 42272), *Abdominal B* (stock 38625), *eyeless,* (stock 42271), *spineless*
610 (transcript variant A, stock 42289), and *grain* (stock 58483) tagged BACs were
611 generated by Rebecca Spokony and Kevin P. White and are available at the
612 Bloomington Stock Center. For the *scalloped* gene, a GFP-trap line was used
613 (Buszczak et al., 2007), a kind gift from Allan C. Spradling laboratory (line CA07575),
614 with which genome-wide chromatin immunoprecipitation experiments have been
615 performed (Slattery et al., 2013). For the *spineless* gene, Bloomington stock 42676,
616 which tags isoforms C and D of the Spineless protein has been also tried in
617 fluorescence imaging and FCS experiments, but did not yield detectable fluorescence
618 in the antennal disc, rendering it inappropriate to be used in our analysis. Therefore,
619 we resided to stock 42289, which tags the A isoform of the protein. For the *eyeless*
620 gene, the FlyFos015860(pRedFlp-Hgr)(ey13630::2XTY1-SGFP-V5-preTEV-BLRP-
621 3XFLAG)dFRT line (VDRC ID 318018) has been tried also in fluorescence imaging
622 and FCS experiments, but did not yield detectable fluorescence in the eye disc for it
623 to be used in our analysis. The *act5C*-FRT-yellow-FRT-Gal4 (Ay-Gal4) line used for
624 clonal overexpression or *RNAi* knockdown has been described (Ito et al., 1997). The
625 UAS-Antp lines (synthetic and full-length), as well as UAS-SynthScr constructs have

626 been previously described (Papadopoulos et al., 2011; Papadopoulos et al., 2010).
627 The *Dll*-Gal4 (MD23) line has been a kind gift of Ginés Morata (Calleja et al., 1996).
628 *69B*-Gal4 and *ptc*-Gal4 have been obtained from the Bloomington Stock Center. The
629 *Antp* P1-*lacZ* and P2-*lacZ* have been previously described (Engstrom et al., 1992; Zink
630 et al., 1991). The P1 reporter construct spans the region between 9.4 kb upstream of
631 the P1 promoter transcription initiation site and 7.8 kb downstream into the first intron,
632 including the first exon sequences and thus comprising 17.2 kb of Antp regulatory
633 sequences (pAPT 1.8). The line used has been an insertion of the pAPT 1.8 vector
634 bearing the P1 promoter regulatory sequences upstream of an *actin-lacZ* cytoplasmic
635 reporter and has been inserted in cytogenetic location 99F on the right chromosomal
636 arm of chromosome 3. The *Antp-RNAi* line has been from VDRC, line KK101774.
637 UAS-eGFP stock was a kind gift of Konrad Basler. We are indebted to Sebastian Dunst
638 for generating the *ubi*-FRT-mCherry(stop)-FRT-Gal4(VK37)/CyO line, which drives
639 clonal overexpression upon flippase excision, while simultaneously marking cells by
640 the loss of mCherry. For red-color labeling of clones the *act5C*-FRT-CD2-FRT-Gal4,
641 UAS-mRFP1(NLS)/TM3 stock 30558 from the Bloomington Stock Center has been
642 used. For marking the ectopic expression domain of untagged Antp proteins the UAS-
643 mRFP1(NLS)/TM3 stock 31417 from the Bloomington Stock Center has been used.
644 The *MS243*-Gal4; UAS-GFP/CyO line was a kind gift from the laboratory of Ernesto
645 Sánchez-Herrero.
646
647 <u>Fly genotypes corresponding to fluorescence images</u>
648 Supplemental Fig. S1A: FlyFos018487(pRedFlp-Hgr)(ato37785::2XTY1-SGFP-V5-
649 preTEV-BLRP-3XFLAG)dFRT

650 Supplemental Fig. S1B: FlyFos024884(pRedFlp-Hgr)(brk25146::2XTY1-SGFP-V5-
651 preTEV-BLRP-3XFLAG)dFRT
652 Supplemental Fig. S1C: FlyFos030836(pRedFlp-Hgr)(salm30926::2XTY1-SGFP-V5-
653 preTEV-BLRP-3XFLAG)dFRT
654 Supplemental Fig. S1: FlyFos029681(pRedFlp-Hgr)(yki19975::2XTY1-SGFP-V5-
655 preTEV-BLRP-3XFLAG)dFRT
656 Supplemental Fig. S1E: w^{1118}; PBac(fkh-GFP.FPTB)VK00037/SM5
657 Supplemental Fig. S1F: *sd*-eGFP (FlyTrap, homozygous)
658 Supplemental Fig. S1G: w^{1118}; PBac(grh-GFP.FPTB)VK00033
659 Supplemental Fig. S1H: FlyFos018974(pRedFlp-Hgr)(Scr19370::2XTY1-SGFP-V5-
660 preTEV-BLRP-3XFLAG)dFRT
661 Supplemental Fig. S1I: FlyFos015942(pRedFlp-Hgr)(sens31022::2XTY1-SGFP-V5-
662 preTEV-BLRP-3XFLAG)dFRT
663 Supplemental Fig. S1J,K: Antp-eGFP (MiMIC) homozygous (line MI02272, converted
664 to an artificial exon)
665 Supplemental Fig. S1L: w^{1118}; PBac(Abd-B-EGFP.S)VK00037/SM5
666 Supplemental Fig. S1M: w^{1118}; PBac(ey-GFP.FPTB)VK00033
667 Supplemental Fig. S1N: w^{1118}; PBac(ss-GFP.A.FPTB)VK00037
668 Supplemental Fig. S1O,P: w^{1118}; PBac(grn-GFP.FPTB)VK00037
669 Fig. 2B,B': *hs*-flp/+; *act5C*-FRT-yellow-FRT-Gal4/+; UAS-SynthAntp long linker-
670 eGFP/+
671 Fig. 2C,C': *hs*-flp/+; *act5C*-FRT-yellow-FRT-Gal4, UAS-eGFP/+; UAS-Antp long linker
672 (full-length, untagged)/+
673 Fig. 2F,F': *Dll*-Gal4 (MD23)/+; UAS-SynthAntp-eGFP/*Antp* P1-*lacZ*
674 Supplemental Fig. S3A,A': *Antp* P1-*lacZ*/TM3

675 Supplemental Fig. S3B,B': *Antp* P2-*lacZ*/CyO

676 Supplemental Fig. S3C,C': wild type

677 Supplemental Fig. S3D,D': *hs*-flp; *act5C*-FRT-yellow-FRT-Gal4, UAS-eGFP

678 Supplemental Fig. S3E,E': *hs*-flp/+; *act5C*-FRT-yellow-FRT-Gal4, UAS-eGFP/+; *Antp*
679 P1-*lacZ*/+

680 Supplemental Fig. S3F,F': *hs*-flp/+; *act5C*-FRT-yellow-FRT-Gal4, UAS-eGFP/+; UAS-
681 Antp long linker (full-length, untagged)/*Antp* P1-*lacZ*

682 Supplemental Fig. S3G,G': *Dll*-Gal4 (MD23)/+; UAS-Antp long linker (full-length,
683 untagged), UAS-mRFP1(NLS)/ *Antp* P1-*lacZ*

684 Supplemental Fig. S3H,H': *Dll*-Gal4 (MD23)/+; UAS-mRFP1(NLS)/ *Antp* P1-*lacZ*

685 Supplemental Fig. S4A: *Dll*-Gal4 (MD23)/+; UAS-SynthAntp long linker-eGFP/+

686 Supplemental Fig. S4B: *ptc*-Gal4/+; UAS-SynthAntp long linker-eGFP/+

687 Supplemental Fig. S4C: *Dll*-Gal4 (MD713)/+; UAS-SynthAntp long linker-eGFP/+

688 Supplemental Fig. S4D,G,H,K: *69B*-Gal4/UAS-SynthAntp long linker-eGFP

689 Supplemental Fig. S4I,J,L: *69B*-Gal4/UAS- eGFP

690 Fig. 3B,B',G,G': *hs*-flp/+; *ubi*-FRT-mChery-FRT-Gal4/+; Antp-eGFP (MiMIC)/UAS-
691 Antp long linker (full-length, untagged)

692 Fig. 3C,C': *hs*-flp/+; UAS-Antp^{RNAi}/+; *Antp* P1-*lacZ*/*act5C*-FRT-CD2-FRT-Gal4, UAS-
693 mRFP1(NLS)

694 Fig. 3H,H': *hs*-flp/+; UAS-Antp^{RNAi}/*act5C*-FRT-yellow-FRT-Gal4, UAS-eGFP; *Antp* P1-
695 *lacZ*/+

696 Supplemental Fig. S6B: *Antp* P1-*lacZ*/TM6B

697 Supplemental Fig. S7A,A': *hs*-flp/+; *ubi*-FRT-mChery-FRT-Gal4/+; Antp-eGFP
698 (MiMIC)/UAS-Antp long linker (full-length, untagged)

699 Supplemental Fig. S7B-C': *hs*-flp/+; *ubi*-FRT-mChery-FRT-Gal4/+; Antp-eGFP
700 (MiMIC)/+
701 Supplemental Fig. S7D,D': *hs*-flp/+; *act5C*-FRT-yellow-FRT-Gal4, UAS-eGFP/+; *Antp*
702 P1-*lacZ*/UAS-Antp long linker (full-length, untagged)
703 Supplemental Fig. SE,E': *hs*-flp/+; *act5C*-FRT-yellow-FRT-Gal4/+; UAS-SynthAntp
704 long linker-eGFP/+
705 Supplemental Fig. S7F,F': *hs*-flp/+; *act5C*-FRT-yellow-FRT-Gal4, UAS-eGFP/+
706 Supplemental Fig. S7G,G': *hs*-flp/+; *act5C*-FRT-yellow-FRT-Gal4, UAS-eGFP/+; *Antp*
707 P1-*lacZ*/+
708 Supplemental Fig. S7H,H': *hs*-flp/+; UAS-Antp^{RNAi}/+; Antp-eGFP (MiMIC)/*act5C*-FRT-
709 CD2-FRT-Gal4, UAS-mRFP1(NLS)
710 Fig. 4B,B': *ptc*-Gal4/+; UAS-SynthAntp long linker-eGFP/+
711 Fig. 4C,C': *Dll*-Gal4 (MD23)/+; UAS-SynthAntp long linker-eGFP/*Antp* P1-*lacZ*
712 Fig. 4F,F': *ptc*-Gal4/+; UAS-SynthAntp long linker-eGFP/+
713 Fig. 4G,G': *Dll*-Gal4 (MD23)/+; UAS-SynthAntp short linker-eGFP/*Antp* P1-*lacZ*
714 Supplemental Fig. S9A,A': *hs*-flp/+; *act5C*-FRT-yellow-FRT-Gal4/+; UAS-SynthAntp
715 short linker-eGFP/+
716 Supplemental Fig. S9B,B',G,G': *hs*-flp/+; *act5C*-FRT-yellow-FRT-Gal4/+; UAS-
717 SynthAntp short linker-eGFP/*Antp* P1-*lacZ*
718 Supplemental Fig. S9C,C',H,H': *hs*-flp/+; *act5C*-FRT-yellow-FRT-Gal4/+; UAS-Antp
719 short linker (full-length, untagged)/*Antp* P1-*lacZ*
720 Supplemental Fig. S9D,D': *hs*-flp/+; *Dll*-Gal4 (MD23)/+; UAS-Antp short linker (full-
721 length, untagged), UAS-mRFP1(NLS)/*Antp* P1-*lacZ*
722 Supplemental Fig. S9E-F': *hs*-flp/+; *ubi*-FRT-mChery-FRT-Gal4/+; Antp-eGFP
723 (MiMIC)/UAS-Antp short linker (full-length, untagged)

724 Supplemental Fig. S9I,I': *ptc*-Gal4/+; UAS-SynthAntp long linker-eGFP/*Antp* P1-*lacZ*

725 Supplemental Fig. S9J,J': *ptc*-Gal4/+; UAS-SynthAntp short linker-eGFP/*Antp* P1-*lacZ*

726 Fig. 5A: *Dll*-Gal4 (MD23)/+; UAS-SynthAntp long linker-eGFP/+

727 Fig. 5B: *ptc*-Gal4/+; UAS-SynthAntp long linker-eGFP/+

728 Fig. 5C: *Dll*-Gal4 (MD713)/+; UAS-SynthAntp long linker-eGFP/+

729 Fig. 5D: *69B*-Gal4/UAS-SynthAntp long linker-eGFP

730 Supplemental Fig. S11A-B': *ubi*-mRFP1(NLS)/+ or y; Antp-eGFP (MiMIC)/+

731 Supplemental Fig. S12B,C: *Dll*-Gal4 (MD23)/+; UAS-mCitrine-SynthScr/+

732 Fig. 6A,B: *Dll*-Gal4 (MD23)/+; UAS-SynthAntp long linker-eGFP/+ or *Dll*-Gal4

733 (MD23)/+; UAS-SynthAntp short linker-eGFP/+

734 Fig. 6J: *Dll*-Gal4 (MD23)/+; UAS-mCitrine-SynthScr/+

735 Supplemental Fig. S13A,D,D': *MS243*-Gal4/+; UAS-SynthAntp long linker-eGFP/*Dr* or

736 *MS243*-Gal4/+; UAS-SynthAntp short linker-eGFP/*Dr*

737 Supplemental Fig. S13B,F,F': *MS243*-Gal4/+; UAS-mCitrine-SynthScr/+

738 Supplemental Fig. S13C,I,I': *Dll*-Gal4 (MD23)/+; UAS-mCitrine-SynthScr/+

739 Supplemental Fig. S13E,E': *ptc*-Gal4/+; UAS-SynthAntp long linker-eGFP/+

740 Supplemental Fig. S13F,F': *MS243*-Gal4/+; UAS- mCitrine-SynthScr/+

741 Supplemental Fig. S13G,G': *ptc*-Gal4/+; UAS- mCitrine-SynthScr/*Antp* P1-*lacZ*

742 Supplemental Fig. S13H,H': *Dll*-Gal4 (MD23)/+; UAS-mCitrine-SynthScr/*Antp* P1-*lacZ*

743 Supplemental Fig. S13J,J': *MS243*-Gal4/+; UAS-eGFP/+

744

745 <u>Preparation of second and third instar imaginal discs for FCS measurements</u>

746 For FCS measurements, imaginal discs (eye-antennal, wing, leg, humeral and

747 genital) and salivary glands were dissected from third instar wandering larvae, or wing

748 and leg discs from second instar larvae, in Grace's insect tissue culture medium

749 (ThermoFisher Scientific, 11595030) and transferred to 8-well chambered coverglass
750 (Nunc® Lab-Tek™, 155411) containing PBS just prior to imaging or FCS
751 measurements. Floating imaginal discs or salivary glands were sunk to the bottom of
752 the well using forceps.
753
754 Immunostainings in larval imaginal discs
755 Larval imaginal discs were stained according to (Papadopoulos et al., 2010).
756 Stainings for the endogenous Antp protein have been performed using a mouse anti-
757 Antp antibody (Developmental Studies Hybridoma Bank, University of Iowa, anti-Antp
758 4C3) in a dilution of 1:250 for embryos and 1:500 for imaginal discs. eGFP, or eGFP-
759 tagged proteins have been stained using mouse or rabbit anti-GFP antibodies from
760 ThermoFisher Scientific in a dilution of 1:500 in imaginal discs and 1:250 in embryos.
761 mRFP1 was stained using a Chromotek rat anti-RFP antibody. For *Antp* P1 promoter
762 stainings in imaginal discs we used the mouse anti-β-galactosidase 40-1a antibody
763 from Developmental Studies Hybridoma Bank, University of Iowa in a dilution of 1:50.
764 The rabbit anti-Scr antibody was used in a dilution of 1:300 (LeMotte et al., 1989).
765 Confocal images of antibody stainings represent predominatly Z-projections and Zeiss
766 LSM510, Zeiss LSM700 or Zeiss LSM880 Airyscan confocal laser scanning
767 microscopy systems with an inverted stand Axio Observer microscope were used for
768 imaging. Image processing and quantifications have been performed in Fiji (Schindelin
769 et al., 2012). For optimal spectral separation, secondary antibodies coupled to
770 Alexa405, Alexa488, Alexa594 and Cy5 (ThermoFischer Scientific) were used.
771
772 Colocalization of wild type and eGFP-tagged MiMIC Antp alleles in imaginal discs

773 To examine whether the pattern of the MiMIC Antp-eGFP fusion protein
774 recapitulates the Antp wild type expression pattern in both embryo and larval imaginal
775 discs, we performed immunostainings of heterozygous Antp-eGFP and wild type flies
776 to visualize the embryonic (stage 13) and larval expression of *Antp* and eGFP. In this
777 experiment, we 1) visualized the overlap between eGFP and *Antp* (the eGFP pattern
778 reflects the protein encoded by the MiMIC allele, whereas the *Antp* pattern reflects the
779 sum of protein produced by the MiMIC allele and the allele of the balancer
780 chromosome) and 2) compared the eGFP expression pattern to the Antp expression
781 pattern in wild type discs and embryos.
782
783 Induction of early and late overexpression and *RNAi*-knockdown clones in imaginal
784 discs
785 Genetic crosses with approximately 100 virgin female and 100 male flies were
786 set up in bottles and the flies were allowed to mate for 2 days. Then, they were
787 transferred to new bottles and embryos were collected for 6 hours at 25°C. Flies were
788 then transferred to fresh bottles and kept until the next collection at 18°C. To asses
789 Antp auto-activation, the collected eggs were allowed to grow at 25°C for 26 h from
790 the midpoint of collection, when they were subjected to heat-shock by submersion to
791 a water-bath of 38°C for 30 min and then placed back at 25°C until they reached the
792 stage of third instar wandering larvae, when they were collected for dissection, fixation
793 and staining with antibodies. To assess Antp auto-repression, the same procedure
794 was followed, except that the heat-shock was performed at 60 h of development after
795 the midpoint of embryo collection. Whenever necessary, larval genotypes were
796 selected under a dissection stereomicroscope with green and red fluorescence filters

797 on the basis of *deformed* (*dfd*)-YFP bearing balancer chromosomes (Le et al., 2006)
798 and visual inspection of fluorescence in imaginal discs.
799
800 Measurement of Antp transcript variant abundance
801 The linker between the Antp YPWM motif and the homeodomain contains the
802 sequence RSQFGKCQE. Short linker isoforms encode the sequence RSQFE,
803 whereas long linker isoforms are generated by alternative splicing of a 12 base pair
804 sequence encoding the four amino acid sequence GKCQ into the mRNA. We initially
805 designed primer pairs for RT-qPCR experiments to distinguish between the short and
806 long linker mRNA variants. For the short linker variant, we used nucleotide sequences
807 corresponding to RSQFERKR (with RKR being the first 3 amino acids of the
808 homeodomain). For detection of the long linker variant we designed primers either
809 corresponding to the RSQFGKCQ sequence, or GKCQERKR. We observed in control
810 PCRs (using plasmid DNA harboring either a long or a short linker cDNA) that primers
811 designed for the short linker variant still amplified the long linker one. Moreover, with
812 linker sequences differing in only four amino acids, encoded by 12 base pars, primer
813 pairs flanking the linker could also not be used, since, due to very similar sizes, both
814 variants would be amplified in RT-qPCR experiments with almost equal efficiencies.
815 Therefore, we used primer pairs flanking the linker region to indiscriminately amplify
816 short and long linker variants, using non-saturating PCR (18 cycles) on total cDNA
817 generated from total RNA. We then resolved and assessed the relative amounts of
818 long and short linker amplicons in a second step using Fragment Analyzer (Advanced
819 Analytical). RNA was extracted from stage 13 embryos, second instar larvae at 60 h
820 of development, and leg or wing discs from third instar wandering larvae using the
821 Trizol® reagent (ThermoFischer Scientific), following the manufacturer's instructions.

822 Total RNA amounts were measured by NanoDrop and equal amounts were used to
823 synthesize cDNA using High-Capacity RNA-to-cDNA™ Kit (ThermoFischer Scientific),
824 following the manufacturer's instructions. Total cDNA yields were measured by
825 NanoDrop and equal amounts were used in PCR, using in-house produced Taq
826 polymerase. 10 ng of plasmid DNA, bearing either a long or a short transcript cDNA
827 were used as a control. PCR product abundance was analyzed both by agarose gel
828 electrophoresis and using Fragment Analyzer (Advanced Analytical).

829 The quantification of the transcript variant concentration (Fig. 4 D and H) has
830 been made considering 100% (value equal to 1 on the y axis) as the sum of long and
831 short isoforms at each developmental stage, whereas the quantification of the relative
832 activation and repression efficiency has been performed considering the short linker
833 variant as having 100% repression and the long linker variant as having 100%
834 activation (values equal to 1 on the y-axis) efficiency.

835

836 Quantification of the relative repressing and activating efficiencies of different Antp
837 isoforms

838 Quantification of the relative efficiency of Antp activating and repressing
839 isoforms (Fig. 4D,H) were performed in Fiji (Schindelin et al., 2012) by outlining the
840 total region of repression or activation of Antp protein or P1 reporter staining and
841 quantification of the relative fluorescence intensity of the selected regions. From the
842 calculated values, we have subtracted the values obtaining by outlining and calculating
843 Antp protein or reporter beta-galactosidase staining background in the region of
844 expression of an eGFP transgene alone (negative control). 5-7 imaginal disc images
845 per investigated genotype were used for analysis. For the repression assay the
846 obtained values have been normalized over the intensity of Antp protein calculated in

847 the region of overlap between an eGFP expressing transgene and Antp (negative
848 control). In both cases (repression and activation), the highest efficiency per transcript
849 variant (for repression, the short linker isoform; for activation the long linker isoform)
850 have been set to 100%.
851
852 Fluorescence Microscopy Imaging of live imaginal discs and FCS
853 Fluorescence imaging and FCS measurements were performed on two
854 uniquely modified confocal laser scanning microscopy systems, both comprised of the
855 ConfoCor3 system (Carl Zeiss, Jena, Germany) and consisting of either an inverted
856 microscope for transmitted light and epifluorescence (Axiovert 200 M); a VIS-laser
857 module comprising the Ar/ArKr (458, 477, 488 and 514 nm), HeNe 543 nm and HeNe
858 633 nm lasers and the scanning module LSM510 META; or a Zeiss LSM780 inverted
859 setup, comprising Diode 405 nm, Ar multiline 458, 488 and 514 nm, DPSS 561 nm
860 and HeNe 633 nm lasers. Both instruments were modified to enable detection using
861 silicon Avalanche Photo Detectors (SPCM-AQR-1X; PerkinElmer, USA) for imaging
862 and FCS. Images were recorded at a 512X512 pixel resolution. C-Apochromat 40x/1.2
863 W UV-VIS-IR objectives were used throughout. Fluorescence intensity fluctuations
864 were recorded in arrays of 10 consecutive measurements, each measurement lasting
865 10 s. Averaged curves were analyzed using the software for online data analysis or
866 exported and fitted offline using the OriginPro 8 data analysis software (OriginLab
867 Corporation, Northampton, MA). In either case, the nonlinear least square fitting of the
868 autocorrelation curve was performed using the Levenberg–Marquardt algorithm.
869 Quality of the fitting was evaluated by visual inspection and by residuals analysis.
870 Control FCS measurements to asses the detection volume were routinely performed
871 prior to data acquisition, using dilute solutions of known concentration of Rhodamine

872 6G and Alexa488 dyes. The variability between independent measurements reflects
873 variabilitys between cells, rather than imprecision of FCS measurements. For more
874 details on Fluorescence Microscopy Imaging and FCS, refer to Supplement 1.

875 In Figure 1A-H the workflow of FCS measurements is schematically
876 represented. Live imaging of imaginal discs, expressing endogenously-tagged TFs,
877 visualized by fluorescence microscopy and neighboring cells, expressing TFs at
878 different levels, selected for FCS measurements (Fig. 1A-B). FCS measurements are
879 performed by placing the focal point of the laser light into the nucleus (Fig 1C-D) and
880 recording fluorescence intensity fluctuations (Fig. 1E), generated by the increase or
881 decrease of the fluorescence intensity, caused by the arrival or departure of fast- and
882 slowly-diffusing TF molecules into or out of the confocal detection volume (Fig. 1D).
883 The recorded fluctuations are subjected to temporal autocorrelation analysis, which
884 generates temporal autocorrelation curves (henceforth referred to as FCS curves),
885 which by fitting with an appropriate model (Supplement 1), yield information about the
886 absolute concentration of fluorescent molecules (F) and, after normalization to the
887 same amplitude, their corresponding diffusion times, as well as the fraction of fast-
888 and slowly-diffusing TF molecules (Fig. 1G). The concentration of molecules is
889 inversely proportional to the y-axis amplitude at the origin of the FCS curve (Fig. 1F).
890 Processes that slow down the diffusion of TF molecules, such as binding to very large
891 molecules (e.g. chromosomal DNA), are visible by a shift of the FCS curves to longer
892 characteristic times (Fig. 1G). Measurements in a collection of neighboring cell nuclei
893 also allow the calculation of protein concentration variability at the live tissue level (Fig.
894 1H).

895

896 <u>Sample size, biological and technical replicates</u>

897 For the measurement of TF molecular numbers and variability (Fig. 1 and
898 Supplemental Fig. S1), 7-10 larvae of each fly strain were dissected, yielding at least
899 15 imaginal discs, which were used in FCS analysis. For the Fkh TF, 7 pairs of salivary
900 glands were analyzed and for AbdB, 12 genital discs were dissected from 12 larvae.
901 More than 50 FCS measurements were performed in patches of neighboring cells of
902 these dissected discs, in the regions of expression indicated in Supplemental Fig. S1
903 by arrows. Imaginal discs from the same fly strain (expressing a given endogenously-
904 tagged TF) were analyzed on at least 3 independent instances (FCS sessions), taking
905 place on different days (biological replicates) and for Antp, which was further analyzed
906 in this study, more than 20 independent FCS sessions were used. As routinely done
907 with FCS measurements in live cells, these measurements were evaluated during
908 acquisition and subsequent analysis and, based on their quality (high counts per
909 molecule and second, low photobleaching), were included in the calculation of
910 concentration and variability. In Supplemental Fig. S1Q, *n* denotes the number of FCS
911 measurements included in the calculations.

912 For experiments involving immunostainings in imaginal discs to investigate the
913 auto-regulatory behavior of Antp (Figs. 2-5 and supplements thereof, except for the
914 temporally-resolved auto-activating and repressing study of Antp in Fig. 3, as
915 discussed above), 14-20 male and female flies were mated in bottles and 10 larvae
916 were selected by means of fluorescent balancers and processed downstream. Up to
917 20 imaginal discs were visualized by fluorescence microscopy and high resolution Z-
918 stacks were acquired for 3-5 representative discs or disc regions of interest per
919 experiment. All experiments were performed in triplicate, except for the temporal
920 analysis of Antp auto-regulatory behavior in Fig. 3 (and Supplemental Figs. thereof),
921 which was performed 6 times and the quantification of repression efficiency of short

922 and long linker Antp isoforms in Fig. 4 (and Supplemental Figs. thereof), which was
923 performed 5 times.
924 For the quantification of transcript variant abundance in Fig. 4D,H, RNA and
925 thus cDNA was prepared from each stage 3 independent times (biological replicates)
926 and the transcript abundance per RNA/cDNA sample was also analyzed 3 times.
927 For the experiments involving perturbations in Antp expression whereby the proper
928 development of the leg and the notum have been assessed in Fig. 5, more than 100
929 adult flies have been analyzed and this experiment has been performed more than 10
930 times independently.
931
932 Statistical significance
933 Fig. 3E: Statistical significance was determined using a two-tailed Student's T-test (***,
934 $p < 0.001$ and *, $p < 0.05$, namely $p_{concentration}^{2nd\ vs\ 3rd\ instar} = 2.04 \cdot 10^{-20}$, $p_{\tau D2}^{2nd\ vs\ 3rd\ instar} =$
935 $7.2 \cdot 10^{-4}$ and $p_{variation}^{2nd\ vs\ 3rd\ instar} = 3.4 \cdot 10^{-2}$).
936 Fig. 4D, H: Statistical significance was determined using a two-tailed Student's T-test
937 between measurements performed with the long linker (auto-activating) isoform (Fig.
938 4D) and the short linker (auto-repressing) isoform (Fig. 4H) (***, $p < 0.001$ and *, $p <$
939 0.05, namely $p_{concentration}^{embryo\ long\ vs\ short} = 3.16 \cdot 10^{-5}$, $p_{concentration}^{2nd\ instar\ long\ vs\ short} = 1.16 \cdot 10^{-4}$,
940 $p_{concentration}^{3rd\ instar\ long\ vs\ short} = 2.85 \cdot 10^{-6}$, $p_{relative\ activation}^{long\ vs\ short} = 4.1 \cdot 10^{-3}$, $p_{relative\ repression}^{long\ vs\ short} =$
941 $2.4 \cdot 10^{-4}$ and $p_{DNA-bound\ fraction\ (FCS)}^{long\ vs\ short} = 5.6 \cdot 10^{-10}$).
942 Fig. 6C-C': Statistical significance was determined using a two-tailed Student's T-test
943 ($p_{leg\ disc,\ o/e\ activator}^{early\ vs\ late\ conc.} = 0.679$ and $p_{leg\ disc,\ o/e\ repressor}^{early\ vs\ late\ conc.} = 0.454$).
944 Fig. 6K: Statistical significance was determined using a two-tailed Student's T-test
945 ($p_{leg\ disc,\ o/e\ exog.\ repr.}^{early\ vs\ late\ conc.} = 0.892$).

946

947 **Acknowledgements**

948 We are deeply saddened by the unexpected passing of Prof. Walter J. Gehring,
949 at the very inception of this work, when the project was still in the planning and
950 preliminary data gathering stage. Prof. Gehring was an extraordinary human being
951 and a scientific giant, whose work will continue to educate and inspire generations to
952 come. DKP has been supported by a long-term fellowship from the Swiss National
953 Science Foundation (PBBSP-138700) and a long-term fellowship from the Federation
954 of European Biochemical Societies (FEBS). VV has been supported by the Knut and
955 Alice Wallenberg foundation and Karolinska Institute Research Funds. DKP would like
956 to express his gratitude to PT for outstanding scientific, and uninterrupted financial,
957 support. DKP would like to acknowledge Markus Burkhardt, Sylke Winkler, Aliona
958 Bogdanova and the Light Microscopy facility of MPI-CBG. DKP is also grateful to
959 Konstantinos Papadopoulos for advice on the mathematical analysis. The authors
960 thank Wendy Bickmore, Jan Brugues and Thomas M. Schultheiss for critical
961 comments on the manuscript.

962

963 **References**

964 Abbott, M.K., and Kaufman, T.C. (1986). The relationship between the functional
965 complexity and the molecular organization of the Antennapedia locus of Drosophila
966 melanogaster. Genetics *114*, 919-942.

967 Baumgartner, S., Littleton, J.T., Broadie, K., Bhat, M.A., Harbecke, R., Lengyel, J.A.,
968 Chiquet-Ehrismann, R., Prokop, A., and Bellen, H.J. (1996). A Drosophila neurexin is
969 required for septate junction and blood-nerve barrier formation and function. Cell *87*,
970 1059-1068.

971 Becskei, A., and Serrano, L. (2000). Engineering stability in gene networks by
972 autoregulation. Nature *405*, 590-593.
973 Blake, W.J., M, K.A., Cantor, C.R., and Collins, J.J. (2003). Noise in eukaryotic gene
974 expression. Nature *422*, 633-637.
975 Boettiger, A.N., and Levine, M. (2013). Rapid transcription fosters coordinate snail
976 expression in the Drosophila embryo. Cell reports *3*, 8-15.
977 Buszczak, M., Paterno, S., Lighthouse, D., Bachman, J., Planck, J., Owen, S., Skora,
978 A.D., Nystul, T.G., Ohlstein, B., Allen, A.*, et al.* (2007). The carnegie protein trap
979 library: a versatile tool for Drosophila developmental studies. Genetics *175*, 1505-
980 1531.
981 Calleja, M., Moreno, E., Pelaz, S., and Morata, G. (1996). Visualization of gene
982 expression in living adult Drosophila. Science *274*, 252-255.
983 Clark, N.M., Hinde, E., Winter, C.M., Fisher, A.P., Crosti, G., Blilou, I., Gratton, E.,
984 Benfey, P.N., and Sozzani, R. (2016). Tracking transcription factor mobility and
985 interaction in Arabidopsis roots with fluorescence correlation spectroscopy. eLife *5*.
986 Crickmore, M.A., Ranade, V., and Mann, R.S. (2009). Regulation of Ubx expression
987 by epigenetic enhancer silencing in response to Ubx levels and genetic variation.
988 PLoS genetics *5*, e1000633.
989 Dublanche, Y., Michalodimitrakis, K., Kummerer, N., Foglierini, M., and Serrano, L.
990 (2006). Noise in transcription negative feedback loops: simulation and experimental
991 analysis. Mol Syst Biol *2*, 41.
992 Dworkin, I., Lee, W., McCloskey, F., and Larsen, E. (2007). Complex genetic
993 interactions govern the temporal effects of Antennapedia on antenna-to-leg
994 transformations in Drosophila melanogaster. J Genet *86*, 111-123.

995 Elowitz, M.B., Levine, A.J., Siggia, E.D., and Swain, P.S. (2002). Stochastic gene
996 expression in a single cell. Science *297*, 1183-1186.
997 Emerald, B.S., and Cohen, S.M. (2004). Spatial and temporal regulation of the
998 homeotic selector gene Antennapedia is required for the establishment of leg identity
999 in Drosophila. Dev Biol *267*, 462-472.
1000 Engstrom, Y., Schneuwly, S., and Gehring, W.J. (1992). Spatial and Temporal
1001 Expression of an Antennapedia Lac Z Gene Construct Integrated into the Endogenous
1002 Antennapedia Gene of Drosophila-Melanogaster. Dev Genes Evol *201*, 65-80.
1003 Franz, K., Singh, A., and Weinberger, L.S. (2011). Lentiviral vectors to study stochastic
1004 noise in gene expression. Methods in enzymology *497*, 603-622.
1005 Garaulet, D.L., Foronda, D., Calleja, M., and Sanchez-Herrero, E. (2008). Polycomb-
1006 dependent Ultrabithorax Hox gene silencing induced by high Ultrabithorax levels in
1007 Drosophila. Development *135*, 3219-3228.
1008 Gillespie, D.T. (2007). Stochastic simulation of chemical kinetics. Annu Rev Phys
1009 Chem *58*, 35-55.
1010 Gregor, T., Tank, D.W., Wieschaus, E.F., and Bialek, W. (2007a). Probing the limits
1011 to positional information. Cell *130*, 153-164.
1012 Gregor, T., Wieschaus, E.F., McGregor, A.P., Bialek, W., and Tank, D.W. (2007b).
1013 Stability and nuclear dynamics of the bicoid morphogen gradient. Cell *130*, 141-152.
1014 Gronlund, A., Lotstedt, P., and Elf, J. (2013). Transcription factor binding kinetics
1015 constrain noise suppression via negative feedback. Nat Commun *4*, 1864.
1016 Halford, S.E., and Marko, J.F. (2004). How do site-specific DNA-binding proteins find
1017 their targets? Nucleic Acids Res *32*, 3040-3052.
1018 Holloway, D.M., Lopes, F.J., da Fontoura Costa, L., Travencolo, B.A., Golyandina, N.,
1019 Usevich, K., and Spirov, A.V. (2011). Gene expression noise in spatial patterning:

1020 hunchback promoter structure affects noise amplitude and distribution in Drosophila
1021 segmentation. PLoS computational biology *7*, e1001069.
1022 Holloway, D.M., and Spirov, A.V. (2015). Mid-embryo patterning and precision in
1023 Drosophila segmentation: Kruppel dual regulation of hunchback. PLoS One *10*,
1024 e0118450.
1025 Ito, K., Awano, W., Suzuki, K., Hiromi, Y., and Yamamoto, D. (1997). The Drosophila
1026 mushroom body is a quadruple structure of clonal units each of which contains a
1027 virtually identical set of neurones and glial cells. Development *124*, 761-771.
1028 Jorgensen, E.M., and Garber, R.L. (1987). Function and misfunction of the two
1029 promoters of the Drosophila Antennapedia gene. Genes Dev *1*, 544-555.
1030 Kang, M., Piliszek, A., Artus, J., and Hadjantonakis, A.K. (2013). FGF4 is required for
1031 lineage restriction and salt-and-pepper distribution of primitive endoderm factors but
1032 not their initial expression in the mouse. Development *140*, 267-279.
1033 Kaur, G., Costa, M.W., Nefzger, C.M., Silva, J., Fierro-Gonzalez, J.C., Polo, J.M., Bell,
1034 T.D., and Plachta, N. (2013). Probing transcription factor diffusion dynamics in the
1035 living mammalian embryo with photoactivatable fluorescence correlation
1036 spectroscopy. Nat Commun *4*, 1637.
1037 Kelso, R.J., Buszczak, M., Quinones, A.T., Castiblanco, C., Mazzalupo, S., and
1038 Cooley, L. (2004). Flytrap, a database documenting a GFP protein-trap insertion
1039 screen in Drosophila melanogaster. Nucleic Acids Res *32*, D418-420.
1040 Krasnow, M.A., Saffman, E.E., Kornfeld, K., and Hogness, D.S. (1989). Transcriptional
1041 activation and repression by Ultrabithorax proteins in cultured Drosophila cells. Cell
1042 *57*, 1031-1043.
1043 Kuziora, M.A., and McGinnis, W. (1988). Autoregulation of a Drosophila homeotic
1044 selector gene. Cell *55*, 477-485.

1045 Lam, C.S., Mistri, T.K., Foo, Y.H., Sudhaharan, T., Gan, H.T., Rodda, D., Lim, L.H.,
1046 Chou, C., Robson, P., Wohland, T.*, et al.* (2012). DNA-dependent Oct4-Sox2
1047 interaction and diffusion properties characteristic of the pluripotent cell state revealed
1048 by fluorescence spectroscopy. The Biochemical journal *448*, 21-33.
1049 Le, T., Liang, Z., Patel, H., Yu, M.H., Sivasubramaniam, G., Slovitt, M., Tanentzapf,
1050 G., Mohanty, N., Paul, S.M., Wu, V.M.*, et al.* (2006). A new family of Drosophila
1051 balancer chromosomes with a w- dfd-GMR yellow fluorescent protein marker.
1052 Genetics *174*, 2255-2257.
1053 LeMotte, P.K., Kuroiwa, A., Fessler, L.I., and Gehring, W.J. (1989). The homeotic gene
1054 Sex Combs Reduced of Drosophila: gene structure and embryonic expression. EMBO
1055 J *8*, 219-227.
1056 Li, Y., Wang, F., Lee, J.A., and Gao, F.B. (2006). MicroRNA-9a ensures the precise
1057 specification of sensory organ precursors in Drosophila. Genes Dev *20*, 2793-2805.
1058 Little, S.C., Tikhonov, M., and Gregor, T. (2013). Precise developmental gene
1059 expression arises from globally stochastic transcriptional activity. Cell *154*, 789-800.
1060 Lo, C.A., Kays, I., Emran, F., Lin, T.J., Cvetkovska, V., and Chen, B.E. (2015).
1061 Quantification of Protein Levels in Single Living Cells. Cell reports *13*, 2634-2644.
1062 Lucas, T., Ferraro, T., Roelens, B., De Las Heras Chanes, J., Walczak, A.M., Coppey,
1063 M., and Dostatni, N. (2013). Live imaging of bicoid-dependent transcription in
1064 Drosophila embryos. Current biology : CB *23*, 2135-2139.
1065 Mistri, T.K., Devasia, A.G., Chu, L.T., Ng, W.P., Halbritter, F., Colby, D., Martynoga,
1066 B., Tomlinson, S.R., Chambers, I., Robson, P.*, et al.* (2015). Selective influence of
1067 Sox2 on POU transcription factor binding in embryonic and neural stem cells. EMBO
1068 reports *16*, 1177-1191.

1069 Morin, X., Daneman, R., Zavortink, M., and Chia, W. (2001). A protein trap strategy to
1070 detect GFP-tagged proteins expressed from their endogenous loci in Drosophila. Proc
1071 Natl Acad Sci U S A *98*, 15050-15055.
1072 Muller, C.B., Loman, A., Pacheco, V., Koberling, F., Willbold, D., Richtering, W., and
1073 Enderlein, J. (2008). Precise measurement of diffusion by multi-color dual-focus
1074 fluorescence correlation spectroscopy. Epl-Europhys Lett *83*.
1075 Nagarkar-Jaiswal, S., Lee, P.T., Campbell, M.E., Chen, K., Anguiano-Zarate, S.,
1076 Gutierrez, M.C., Busby, T., Lin, W.W., He, Y., Schulze, K.L.*, et al.* (2015). A library of
1077 MiMICs allows tagging of genes and reversible, spatial and temporal knockdown of
1078 proteins in Drosophila. eLife *4*.
1079 Nevozhay, D., Adams, R.M., Murphy, K.F., Josic, K., and Balazsi, G. (2009). Negative
1080 autoregulation linearizes the dose-response and suppresses the heterogeneity of
1081 gene expression. Proc Natl Acad Sci U S A *106*, 5123-5128.
1082 Newman, J.R., Ghaemmaghami, S., Ihmels, J., Breslow, D.K., Noble, M., DeRisi, J.L.,
1083 and Weissman, J.S. (2006). Single-cell proteomic analysis of S. cerevisiae reveals the
1084 architecture of biological noise. Nature *441*, 840-846.
1085 Papadopoulos, D.K., Krmpot, A.J., Nikolic, S.N., Krautz, R., Terenius, L., Tomancak,
1086 P., Rigler, R., Gehring, W.J., and Vukojevic, V. (2015). Probing the kinetic landscape
1087 of Hox transcription factor-DNA binding in live cells by massively parallel Fluorescence
1088 Correlation Spectroscopy. Mechanisms of development *138 Pt 2*, 218-225.
1089 Papadopoulos, D.K., Resendez-Perez, D., Cardenas-Chavez, D.L., Villanueva-
1090 Segura, K., Canales-del-Castillo, R., Felix, D.A., Funfschilling, R., and Gehring, W.J.
1091 (2011). Functional synthetic Antennapedia genes and the dual roles of YPWM motif
1092 and linker size in transcriptional activation and repression. Proc Natl Acad Sci U S A
1093 *108*, 11959-11964.

1094 Papadopoulos, D.K., Vukojevic, V., Adachi, Y., Terenius, L., Rigler, R., and Gehring,
1095 W.J. (2010). Function and specificity of synthetic Hox transcription factors in vivo. Proc
1096 Natl Acad Sci U S A *107*, 4087-4092.
1097 Pare, A., Lemons, D., Kosman, D., Beaver, W., Freund, Y., and McGinnis, W. (2009).
1098 Visualization of individual Scr mRNAs during Drosophila embryogenesis yields
1099 evidence for transcriptional bursting. Current biology : CB *19*, 2037-2042.
1100 Pelaez, N., Gavalda-Miralles, A., Wang, B., Navarro, H.T., Gudjonson, H., Rebay, I.,
1101 Dinner, A.R., Katsaggelos, A.K., Amaral, L.A., and Carthew, R.W. (2015). Dynamics
1102 and heterogeneity of a fate determinant during transition towards cell differentiation.
1103 eLife *4*.
1104 Perez-Camps, M., Tian, J., Chng, S.C., Sem, K.P., Sudhaharan, T., Teh, C.,
1105 Wachsmuth, M., Korzh, V., Ahmed, S., and Reversade, B. (2016). Quantitative
1106 imaging reveals real-time Pou5f3-Nanog complexes driving dorsoventral
1107 mesendoderm patterning in zebrafish. eLife *5*.
1108 Plachta, N., Bollenbach, T., Pease, S., Fraser, S.E., and Pantazis, P. (2011). Oct4
1109 kinetics predict cell lineage patterning in the early mammalian embryo. Nat Cell Biol
1110 *13*, 117-123.
1111 Quinones-Coello, A.T., Petrella, L.N., Ayers, K., Melillo, A., Mazzalupo, S., Hudson,
1112 A.M., Wang, S., Castiblanco, C., Buszczak, M., Hoskins, R.A.*, et al.* (2007). Exploring
1113 strategies for protein trapping in Drosophila. Genetics *175*, 1089-1104.
1114 Rao, C.V., and Arkin, A.P. (2003). Stochastic chemical kinetics and the quasi-steady-
1115 state assumption: Application to the Gillespie algorithm. J Chem Phys *118*, 4999-5010.
1116 Reed, H.C., Hoare, T., Thomsen, S., Weaver, T.A., White, R.A., Akam, M., and
1117 Alonso, C.R. (2010). Alternative splicing modulates Ubx protein function in Drosophila
1118 melanogaster. Genetics *184*, 745-758.

1119 Saadaoui, M., Merabet, S., Litim-Mecheri, I., Arbeille, E., Sambrani, N., Damen, W.,
1120 Brena, C., Pradel, J., and Graba, Y. (2011). Selection of distinct Hox-Extradenticle
1121 interaction modes fine-tunes Hox protein activity. Proc Natl Acad Sci U S A *108*, 2276-
1122 2281.
1123 Sanchez, A., Garcia, H.G., Jones, D., Phillips, R., and Kondev, J. (2011). Effect of
1124 promoter architecture on the cell-to-cell variability in gene expression. PLoS
1125 computational biology *7*, e1001100.
1126 Sarov, M., Barz, C., Jambor, H., Hein, M.Y., Schmied, C., Suchold, D., Stender, B.,
1127 Janosch, S., K, J.V., Krishnan, R.T.*, et al.* (2016). A genome-wide resource for the
1128 analysis of protein localisation in Drosophila. eLife *5*, e12068.
1129 Schindelin, J., Arganda-Carreras, I., Frise, E., Kaynig, V., Longair, M., Pietzsch, T.,
1130 Preibisch, S., Rueden, C., Saalfeld, S., Schmid, B.*, et al.* (2012). Fiji: an open-source
1131 platform for biological-image analysis. Nat Methods *9*, 676-682.
1132 Schwanhausser, B., Busse, D., Li, N., Dittmar, G., Schuchhardt, J., Wolf, J., Chen, W.,
1133 and Selbach, M. (2011). Global quantification of mammalian gene expression control.
1134 Nature *473*, 337-342.
1135 Sela, I., and Lukatsky, D.B. (2011). DNA sequence correlations shape nonspecific
1136 transcription factor-DNA binding affinity. Biophys J *101*, 160-166.
1137 Sheth, R., Bastida, M.F., Kmita, M., and Ros, M. (2014). "Self-Regulation," A New
1138 Facet of Hox Genes' Function. Dev Dynam *243*, 182-191.
1139 Shimoga, V., White, J.T., Li, Y., Sontag, E., and Bleris, L. (2013). Synthetic
1140 mammalian transgene negative autoregulation. Mol Syst Biol *9*, 670.
1141 Slattery, M., Voutev, R., Ma, L., Negre, N., White, K.P., and Mann, R.S. (2013).
1142 Divergent transcriptional regulatory logic at the intersection of tissue growth and
1143 developmental patterning. PLoS genetics *9*, e1003753.

1144 Smolander, O.P., Kandhavelu, M., Mannerstrom, H., Lihavainen, E., Kalaichelvan, S.,
1145 Healy, S., Yli-Harja, O., Karp, M., and Ribeiro, A.S. (2011). Cell-to-cell diversity in
1146 protein levels of a gene driven by a tetracycline inducible promoter. BMC molecular
1147 biology *12*, 21.
1148 Soltani, M., Bokes, P., Fox, Z., and Singh, A. (2015). Nonspecific transcription factor
1149 binding can reduce noise in the expression of downstream proteins. Phys Biol *12*,
1150 055002.
1151 Stroeher, V.L., Gaiser, J.C., and Garber, R.L. (1988). Alternative RNA splicing that is
1152 spatially regulated: generation of transcripts from the Antennapedia gene of
1153 Drosophila melanogaster with different protein-coding regions. Molecular and cellular
1154 biology *8*, 4143-4154.
1155 Swain, P.S., Elowitz, M.B., and Siggia, E.D. (2002). Intrinsic and extrinsic contributions
1156 to stochasticity in gene expression. Proc Natl Acad Sci U S A *99*, 12795-12800.
1157 Szaloki, N., Krieger, J.W., Komaromi, I., Toth, K., and Vamosi, G. (2015). Evidence
1158 for Homodimerization of the c-Fos Transcription Factor in Live Cells Revealed by
1159 Fluorescence Microscopy and Computer Modeling. Molecular and cellular biology *35*,
1160 3785-3798.
1161 Taniguchi, Y., Choi, P.J., Li, G.W., Chen, H., Babu, M., Hearn, J., Emili, A., and Xie,
1162 X.S. (2010). Quantifying E. coli proteome and transcriptome with single-molecule
1163 sensitivity in single cells. Science *329*, 533-538.
1164 Thattai, M., and van Oudenaarden, A. (2001). Intrinsic noise in gene regulatory
1165 networks. Proc Natl Acad Sci U S A *98*, 8614-8619.
1166 Tiwari, M., Mikuni, S., Muto, H., and Kinjo, M. (2013). Determination of dissociation
1167 constant of the NFkappaB p50/p65 heterodimer using fluorescence cross-correlation

1168 spectroscopy in the living cell. Biochemical and biophysical research communications
1169 *436*, 430-435.
1170 Tsutsumi, M., Muto, H., Myoba, S., Kimoto, M., Kitamura, A., Kamiya, M., Kikukawa,
1171 T., Takiya, S., Demura, M., Kawano, K.*, et al.* (2016). In vivo fluorescence correlation
1172 spectroscopy analyses of FMBP-1, a silkworm transcription factor. FEBS open bio *6*,
1173 106-125.
1174 Venken, K.J., Schulze, K.L., Haelterman, N.A., Pan, H., He, Y., Evans-Holm, M.,
1175 Carlson, J.W., Levis, R.W., Spradling, A.C., Hoskins, R.A.*, et al.* (2011). MiMIC: a
1176 highly versatile transposon insertion resource for engineering Drosophila
1177 melanogaster genes. Nat Methods *8*, 737-743.
1178 Vukojevic, V., Heidkamp, M., Ming, Y., Johansson, B., Terenius, L., and Rigler, R.
1179 (2008). Quantitative single-molecule imaging by confocal laser scanning microscopy.
1180 Proc Natl Acad Sci U S A *105*, 18176-18181.
1181 Vukojevic, V., Papadopoulos, D.K., Terenius, L., Gehring, W.J., and Rigler, R. (2010).
1182 Quantitative study of synthetic Hox transcription factor-DNA interactions in live cells.
1183 Proc Natl Acad Sci U S A *107*, 4093-4098.
1184 Zechner, C., Ruess, J., Krenn, P., Pelet, S., Peter, M., Lygeros, J., and Koeppl, H.
1185 (2012). Moment-based inference predicts bimodality in transient gene expression.
1186 Proc Natl Acad Sci U S A *109*, 8340-8345.
1187 Zink, B., Engstrom, Y., Gehring, W.J., and Paro, R. (1991). Direct interaction of the
1188 Polycomb protein with Antennapedia regulatory sequences in polytene chromosomes
1189 of Drosophila melanogaster. EMBO J *10*, 153-162.

1190

1191 **Figure Legends**

1192 Figure 1: **Concentration, DNA-binding dynamics and cell-to-cell protein**
1193 **concentration variability of 14 Drosophila TFs.** (A-H) Workflow of the study of TFs
1194 by FCS (see Materials and Methods and Supplement 1). (I) Representative average
1195 FCS measurements of eight TFs. (J) FCS curves shown in (I), normalized to the same
1196 amplitude, $G_n(\tau) = 1$ at $\tau = 10\ \mu s$. (K) Variability of the 14 TFs as a function of
1197 concentration. (L) Variability in concentration of endogenous Antp in the wing disc. (M)
1198 Variability of Antp concentration in clusters of neighboring cell nuclei as a function of
1199 concentrations. Error bars in (K) and (N) represent 1 standard deviation.
1200
1201 Figure 2: **Antp activates and represses its own transcription.** (A) Schematic of the
1202 wing disc used for analysis. (B-B') Clonal overexpression of a *SynthAntp-eGFP*
1203 construct. Dashed line in (B) shows a clone in the Antp expression domain. (C-C')
1204 Transcriptional auto-repression of Antp using the *Antp* P1-*lacZ*. (D) Schematic of Antp
1205 transcriptional auto-repression. (E) Schematic of the wing disc used for analysis. (F-
1206 F') Ectopic induction of *Antp* P1-*lacZ* by expression of *SynthAntp-eGFP* using *Dll*-Gal4
1207 (MD23). (G) Schematic of Antp auto-activation. Scale bars denote $100\ \mu m$.
1208
1209 Figure 3: **Antp switches from transcriptional auto-activation to auto-repression.**
1210 (A and F) Schematic representations of the experimental setup (see Materials and
1211 Methods). Black rectangles enclose the regions of clonal analysis used. (B-B')
1212 Endogenous Antp in early-induced clones, marked by the absence of mCherry
1213 (dashed lines in (B)). (C-C') *Antp* P1 transcription in early *Antp RNAi* knockdown
1214 clones (dashed line in (C), marked by nuclear mRFP1. (D) Updated Antp auto-
1215 activation model. (E) Concentration, DNA-binding and variability studied by FCS at
1216 second instar leg and wing discs (FCS analysis in Supplemental Fig. S8). (G-G')

1217 Endogenous Antp in late-induced clones, marked by the absence of mCherry (dashed
1218 lines in (G)). (H-H') *Antp* P1 transcription in early *Antp RNAi* knockdown clones
1219 (dashed line in (H)), marked by nuclear mRFP1. (I) Updated Antp auto-repression
1220 model. Cyan lines in (B, G, H) outlines the region of highest endogenous Antp
1221 expression.
1222
1223 Figure 4: **Antp auto-activation and auto-repression relies on Antp isoforms with**
1224 **different binding affinities to chromatin.** (A) Schematic of the Antp mRNA,
1225 generated from the P1 promoter. Exons are represented by grey boxes. (B-B') *Antp*
1226 auto-repression at the proximal wing disc (white dashed line). (C-C') *Antp* auto-
1227 activation at the proximal wing disc (yellow dashed line). (D) Abundance of long linker
1228 isoform (Materials and Methods); auto-activation and auto-repression efficiencies
1229 (Materials and Methods); DNA-bound fractions, measured by FCS (Supplemental
1230 Figure S10); and relative affinity of binding to chromatin, measured by FCS
1231 (Supplemental Figure S10) for comparison with (H). (E) Updated model of *Antp* auto-
1232 regulation. (F-G') Similar to (B-C') for the short linker isoform. (H) Similar to (D) for
1233 comparison. (I) Updated qualitative model representation of Antp repression as in (E).
1234
1235 Figure 5: **Concentrations resulting in low variability are required for Antp**
1236 **homeotic function.** (A-D) Transformations of the distal antenna into a tarsus in adult
1237 flies, caused by *SynthAntp-eGFP* overexpression in antennal discs (Supplemental
1238 Figure S4A-D). Black arrows point to weaker transformations (ectopic leg bristles). (E-
1239 F) Measurements of SynthAntp concentration and cell-to-cell variability of antennal
1240 discs (Supplemental Figure S4A-D) in the corresponding antennal discs (A-D). (G)
1241 Dynamic Antp promoter (see text for details). (H) Trajectories of individual simulations.

1242 (I) Distribution of Antp isoforms, predicted by the model. (J) Concentration and
1243 variability predicted by the model. (K-L') Model predictions (K and L) and experimental
1244 data validation (K' and L') of variability (K) and protein Fano factor (L) as a function of
1245 Antp concentration.
1246
1247 Figure 6: **Response of *Antp* to genetic perturbations.** (A-B) Overexpression of
1248 SynthAntp-eGFP long or short linker isoform result in tarsal transformations of the
1249 antenna (A), but normal leg development (B). (C-C') Antp concentration and variability,
1250 measured by FCS, in leg discs of second and third instar larvae upon SynthAntp-eGFP
1251 long or short linker isoform expression. (D-I) Model response upon overexpression of
1252 Antp activating or repressing isoforms (similar to Fig. 5H-J). (J) Overexpression of an
1253 exogenous repressor (Scr) results in abnormal leg development Scr. (K-N) Similar to
1254 (C-I) (see also Supplemental Figure S13E-I'). (K) Antp concentration and variability,
1255 measured by FCS in the proximal leg disc of second (early) and third (late) instar
1256 larvae upon overexpression of mCherry-SynthScr.
1257
1258 Supplemental Figure S1: **Measurement of average concentrations and nucleus-**
1259 **to-nucleus variability of 14 endogenously-tagged TFs in Drosophila imaginal**
1260 **discs by FCS.** (A-P) Fluorescence imaging of TFs, showing their expression pattern
1261 in imaginal discs and the salivary gland. White arrows indicate regions where FCS
1262 measurements of endogenous intra-nuclear concentration were performed and the
1263 average concentrations are given for each TF. Images have been contrasted for
1264 visualization purposes. For the Antp and Grn TFs, both leg and wing imaginal discs
1265 have been used for measurements. Average concentrations of TFs measured in
1266 different cells span a range of two orders of magnitude, from few tens to a thousand

1267 nanomolar. Scale bars denote $100\,\mu m$, unless otherwise indicated. (Q)
1268 Characterization of nucleus-to-nucleus variability among neighboring cells within the
1269 same expression domain in imaginal discs of the 14 TF studied by FCS. Black bars
1270 show concentration averages (with error bars representing 1 standard deviation),
1271 whereas grey bars show the variability, i.e. the squared coefficient of variability
1272 (expressed as the variance over the squared mean, $CV^2 = \frac{s^2}{m^2}$). TFs have been sorted
1273 according to increasing variability. (P) Characterization of variability as a function of
1274 concentration, using the Fano factor value (expressed as variance over the mean,
1275 $CV^2 = \frac{s^2}{m}$). The red squares point to the Fano factor values of Antp in the wing and leg
1276 disc.
1277
1278 Supplemental Figure S2: **Characteristic decay times of Antp-eGFP do not change**
1279 **as a function of total concentration.** (A-B) Characteristic decay times τ_{D_1} (A) and
1280 τ_{D_2} (B) do not vary with the concentration of Antp-eGFP TF molecules, as evident
1281 from $\tau_{D_1} = f\,(N_1)$ and $\tau_{D_2} = f\,(N_2)$, where N_1 is the number of freely diffusing, N_2 the
1282 number of bound Antp-eGFP TF molecules and τ_{D_1}, τ_{D_2} their respective diffusion
1283 times.
1284
1285 Supplemental Figure S3: **Antp is able to repress and activate itself at the**
1286 **transcriptional level – controls.** (A-C') Normal expression patterns of the Antp P1
1287 (A-A') and P2 (B-B') transcriptional reporters and Antp protein immunohistochemistry
1288 (C-C'). Boxed areas in (A), (B) and (C) are magnified in (A'), (B') and (C'). The Antp
1289 P1 reporter is highly expressed in the prescutum region of the notum (A') and the
1290 peripodial cells at the base of the wing blade (giving rise to the mesopleura and

1291 pteropleura of the thorax, white arrows in (A)), which overlaps with the Antp protein
1292 pattern ((C') and arrows in (C)). The Antp P2 promoter reporter construct exhibits very
1293 weak, if any, expression at these two domains (B-B'). (D-E') Negative controls of Antp
1294 protein (D-D') and P1 reporter transcription (E-E') upon overexpression of eGFP.
1295 Dashed lines outline the regions of clonal induction in (D) and (E), where neither the
1296 Antp protein (D) nor the Antp P1 reporter (E) are repressed. (F-F') Repression of Antp
1297 P1 reporter transcription upon clonal overexpression of the full-length untagged Antp
1298 protein (Antp-FL). The ectopic expression domain is outlined by white dashed lines in
1299 (F) and marked by the expression of eGFP (F'). (G-G') Activation of Antp P1 reporter
1300 transcription upon ectopic expression of untagged Antp full-length (Antp-FL) with *Dll*
1301 (MD23) driver in the distal region of wing pouch. The ectopic expression domain is
1302 outlined by a yellow dashed line in (G) and is marked by the expression of nuclear
1303 mRFP1. (H-H') Negative control of ectopic activation of Antp P1 transcription upon
1304 overexpression of nuclear mRFP1 alone by *Dll* (MD23)-Gal4. Scale bars denote
1305 $100\ \mu m$.
1306
1307 Supplemental Figure S4: **Direct correlation between Antp concentration and**
1308 **homeotic function – Antp auto-repression and activation occurs at endogenous**
1309 **concentrations.** (A-D) Live imaging (one optical section) of SynthAntp-eGFP
1310 expressed in the distal antennal portion of the eye-antennal disc by different Gal4
1311 drivers. The concentration was measured using FCS and average concentrations are
1312 indicated. An eightfold difference was observed between the strong *Dll*-Gal4 driver
1313 (MD23) (A) and weak *69B*-Gal4 driver (D). (E) Average FCS measurements performed
1314 in nuclei overexpressing *SynthAntp-eGFP*, using different Gal4 drivers. Note that the
1315 y-axis amplitudes at the origin of the FCS curves are inversely proportional to the

1316 concentration. (F) FCS curves of measurements in (E) normalized to the same
1317 amplitude, $G_n(\tau) = 1$ at $\tau = 10\ \mu s$, show major overlap, indicating indistinguishable
1318 behavior of Antp binding to chromatin across the concentration range examined ($0.5 -$
1319 $3.8\ nM$). (G-L) Antp auto-regulation occurs at endogenous concentrations. (G-H)
1320 Repression of endogenous Antp protein upon induction of *SynthAntp-eGFP* in the
1321 proximal regions of the wing disc by *69B*-Gal4, which results in Antp expression very
1322 similar to endogenous levels. (I-J) No repression is observed upon overexpression of
1323 *eGFP* (negative control), as indicated by white arrows in (I). White arrows in (G) and
1324 (I) point to the equivalent area in the wing disc, where Antp repression is observed.
1325 (K) X-gal stainings of the *Antp* P1 reporter show weak but detectable ectopic β-
1326 galactosidase activity in the antennal disc (black arrows). (L) Negative control
1327 stainings of eGFP induced by the *69B* enhancer show complete absence of ectopic
1328 reporter transcription. Scale bars denote $100\ \mu m$, unless otherwise indicated.
1329
1330 Supplemental Figure S5: **Comparison of endogenous and overexpressed Antp by**
1331 **FCS.** (A) FCS curves of Antp-eGFP in wing disc nuclei. Concentration differences of
1332 fluorescent Antp protein are obvious among cells expressing one or two copies of
1333 Antp-eGFP (homozygous and heterozygous larvae) or overexpressing SynthAntp-
1334 eGFP from the *Dll* MD23)-Gal4 driver. (B) FCS curves shown in (A) normalized to the
1335 same amplitude, $G_n(\tau) = 1$ at $\tau = 10\ \mu s$, show pronounced overlap between
1336 homozygous and heterozygous *Antp-eGFP*-expressing cells, as well as between
1337 endogenously expressed *Antp* and overexpressed *SynthAntp-eGFP*, indicating similar
1338 diffusion times and modes of interaction with chromatin. FCS curves are color-coded
1339 as outlined in panel (B).
1340

1341 Supplemental Figure S6: **Antp expression patterns are not altered by the MiMIC**
1342 **MI02272 insertion.** (A) Schematic representation of the Antp-eGFP fusion protein
1343 produced by the conversion of the MiMIC MI02272 construct to an artificial exon. The
1344 eGFP-encoding artificial exon is situated in intron 6 of the mRNA and is spliced in
1345 between exons 6 and 7 that correspond to the long and non-conserved N-terminal
1346 coding sequence of the protein, which has little (if any) function *in vivo* (Papadopoulos
1347 et al., 2011), and does not disrupt the homeodomain or YPWM motif. All features have
1348 been drawn to scale. (B) Heterozygous flies (embryos and third instar larvae),
1349 examined for their Antp-eGFP pattern (detected by an antibody to GFP, green), as
1350 compared to the total amount of Antp (expressed by the sum of the MiMIC *Antp-eGFP*
1351 and the wild type *Antp* loci), detected by an Antp antibody (magenta). Comparisons of
1352 the Antp pattern in wild type embryos and all thoracic imaginal discs are provided
1353 case-wise in the right panel. In discs, dashed lines approximately separate the anterior
1354 (indicated by "A") from the posterior (indicated by "P") domain of the disc. Note the
1355 high expression of Antp in the humeral disc. In the leg discs, Antp is expressed most
1356 strongly in the posterior compartment of the prothoracic leg disc, the anterior
1357 compartment of the mesothoracic leg disc and in an abundant pattern in the
1358 metathoracic leg disc. Cyan arrows point to Antp positive cells in the second and third
1359 leg discs that are centrally located, as previously shown (Engstrom et al., 1992). All
1360 images represent Z-projections. Scale bars denote $100\ \mu m$.
1361
1362 Supplemental Figure S7: **Antp is sufficient and required to trigger a**
1363 **developmental switch from transcriptional auto-activation to auto-repression –**
1364 **controls.** (A-C') Negative controls of Antp clonal auto-activation and repression using
1365 early and late clone induction regimes. (A-A') Without induction of clones expressing

1366 full-length untagged Antp, no repression or activation of endogenous Antp protein is
1367 observed. (B-C') Upon induction of non-overexpressing clones (clones expressing
1368 only Gal4, without a UAS transgene), no activation or repression of Antp protein is
1369 observed at early or late induction time points. White dashed lines in (B) and (C) outline
1370 the induced clones, marked by the absence of mCherry. (D-E') Early ectopic induction
1371 of either Antp full-length untagged protein (D-D') or SynthAntp (E-E') result in
1372 upregulation of the Antp P1 reporter. Yellow dashed lines in (D) and arrows in (E) point
1373 to the induced clones and cyan continuous lines show the regions of high endogenous
1374 expression of the reporter. Clones have been marked by cytoplasmic eGFP. (F-G')
1375 Negative controls of early clonal induction of eGFP alone (without concurrent induction
1376 of Antp) show no repression of the Antp protein (F-F') or the P1 reporter (G-G').
1377 Dashed lines in (G) mark the clones of eGFP induction. (H-H') Positive control of clonal
1378 knockdown of the Antp *RNAi* line used in Fig. 3. Clonal knockdown by *RNAi* (indicated
1379 by the dashed line in (H) and marked by nuclear mRFP1 in (H')) resulted in efficient
1380 downregulation of the endogenous Antp protein. Scale bars denote $100\ \mu m$, unless
1381 otherwise indicated.
1382
1383 Supplemental Figure S8: **Antp concentration and cell-to-cell variability in second**
1384 **and third instar wing and leg imaginal discs** (A-A'') Representative FCS curves
1385 recorded in second and third instar wing and leg imaginal discs, expressing *Antp-*
1386 *eGFP*. Note the low concentration in second instar leg and wing discs, reflected by the
1387 relatively high amplitude of the FCS curves (inversely proportional to concentration) in
1388 (A), as compared to the high concentration in third instar discs in (A'). (B) FCS curves
1389 shown in (A) and (A'), normalized to the same amplitude, $G_n(\tau) = 1$ at $\tau = 10\ \mu s$, show
1390 a shift towards longer decay times in the third instar leg and wing discs, indicative of

1391 pronounced interactions of Antp with chromatin. FCS curves are color-coded as
1392 outlined in panel (A). (C) Quantification of average concentrations and cell-to-cell
1393 variability in protein concentration among neighboring nuclei in wing and leg, second
1394 and third instar, discs. Black bars denote the average concentration and grey bars
1395 denote the variability, expressed as the variance over the squared mean. Note the
1396 increase in average concentration from second to third instar (eleven-fold increase in
1397 the leg disc) and the concurrent drop in variability to almost half of its value. Statistical
1398 significance was determined using Student's two-tailed T-test (***, p<0.001, namely
1399 $p_{3rd-2nd\ instar\ leg} = 4.4 \cdot 10^{-18}$ and $p_{3rd-2nd\ instar\ wing} = 3.2 \cdot 10^{-8}$).
1400
1401 Supplemental Figure S9: **Developmental control of Antp auto-activation and**
1402 **repression relies on the relative concentrations of preferentially auto-activating**
1403 **and auto-repressing Antp isoforms, which display different binding affinities to**
1404 **chromatin – short linker isoform controls.** (A-H') Experiments of Figs. 2-4,
1405 performed with short linker (preferentially auto-repressing) full-length and SynthAntp
1406 isoforms on their capacity to repress and activate Antp P1 reporter transcription and
1407 Antp protein. Dashed lines in all panels outline the clones induced or the region of
1408 ectopic expression using *Dll* (MD23)-Gal4, whereas closed continuous cyan lines
1409 outline the regions of endogenous Antp P1 reporter expression in (G) and (H). (A-A')
1410 Repression of Antp protein by late clonal induction of SynthAntp in the wing notum.
1411 (B-B') Equivalent assay as in (A-A'), but monitoring auto-repression of the Antp P1
1412 promoter transcription. (C-C') Similar assay to (B-B'), using the full-length Antp protein,
1413 induced at the later time point. (D-D') Ectopic induction of full-length, short linker,
1414 untagged Antp cDNA with concurrent labeling of the expression domain by nuclear
1415 mRFP1 results in weak ectopic auto-activation of the Antp P1 reporter. (E-F') Early

1416 and late clonal induction of full-length, short linker, untagged Antp results in auto-
1417 repression (E-E'), or induction (F-F'), of the endogenous Antp protein, respectively.
1418 (G-H') Early clonal induction of SynthAntp (G-G') or the full-length cDNA (H-H'), both
1419 featuring a short linker, triggers ectopic activation of P1 promoter transcription. (I-J')
1420 Antp long (I-I') and short (J-J') linker isoforms repress Antp at the transcriptional level
1421 (monitored by Antp P1 reporter expression) when induced by *ptc*-Gal4 in the wing disc.
1422 Arrows point to the regions of auto-repressed Antp promoter. Scale bars denote
1423 $100\ \mu m$, unless otherwise indicated.
1424
1425 Supplemental Figure S10: **Comparative binding study of Antp short and long**
1426 **linker isoforms by FCS.** (A-B) FCS analysis performed on third instar wing and
1427 antennal imaginal discs, expressing short or long linker Antp isoforms (tagged to
1428 eGFP) close to endogenous concentrations, from the *69B*-enhancer. Cell nuclei of
1429 similar concentrations in the two datasets have been selected for analysis (A).
1430 Average FCS measurements on the short linker Antp isoform display a consistent shift
1431 towards longer decay times, as compared to its long linker counterpart (B), indicating
1432 higher degree of chromatin binding. (C-D') Binding study of short and long linker Antp
1433 isoforms in third instar wing and antennal discs, expressed by *69B*-Gal4. The
1434 concentration of the Antp short and long linker isoform DNA-bound complexes
1435 (derived by fitting the FCS curves in (A)) is plotted as a function of the total
1436 concentration of Antp-eGFP molecules. From the linear regression equations, $y =$
1437 $0.34x - 5.31$ (D') and $y = 0.24x - 3.28$ (E'), the ratio of apparent dissociation
1438 constants for the long and short linker isoforms was calculated to be $\frac{K_{d,Antp}^{long\ linker\ isof.}}{K_{d,Antp}^{short\ linker\ isof.}} >$
1439 2.3 (for the calculation refer to Supplement 3). The two dissociation constants differ at

1440 least 2.3 times, indicating stronger binding of the short linker isoform to the DNA, as
1441 compared to the long linker one.
1442
1443 Supplemental Figure S11: **Investigation of extrinsic variability in the endogenous**
1444 **Antp-eGFP expression domain.** (A-B') Live imaging of a wing disc notum, where
1445 nuclear mRFP1 protein is highly expressed from a constitute enhancer (*ubi-*
1446 mRFP1(NLS)), alongside with endogenous Antp-eGFP. FCS measurements were
1447 performed in the region of high co-expression of Antp and mRFP1. (B-B') Higher
1448 magnification of cells as in (A-A'). Note the uneven distribution of Antp in the nuclei
1449 and the formation of sites of accumulation in (B). (C) Plot of the concentration of Antp-
1450 eGFP (expressed as number of fluorescent molecules in the Observation Volume
1451 Element (OVE)). The correlation coefficient r was calculated to be $r = 0.523$ and the
1452 p-value to be $p_{correlation} = 9.77 \cdot 10^{-5}$. Scale bars denote $100\ \mu m$, unless otherwise
1453 indicated.
1454
1455 Supplemental Figure S12: (A-D) Competition of Antp binding, whereby state "A" can
1456 be reached only through the unbound state "U" in (A), results in increase in Antp
1457 protein numbers (D) without decrease in variability (grey bars in (D)). Trajectories of
1458 individual simulations are presented in (B) and the distribution of the Antp isoforms,
1459 predicted by the model, in (C). (E-H) Requirement of the negative feedback for
1460 suppression of variability. In the absence of the state "R" (E), concentration increases
1461 (H), but variability also increases rather than being suppressed (grey bars in (H)).
1462 Trajectories of individual simulations are presented in (F) and the distribution of the
1463 Antp isoforms, predicted by the model, in (G).
1464

1465 Supplemental Figure S13: **Controls of Antp model predictions and Scr-mediated**
1466 **perturbations.** (A-C) Perturbations of the model system in (Fig. 5A) by
1467 overexpression of Antp long or short linker isoforms or an exogenous Antp repressor
1468 (Scr). Overexpression of activating or repressing SynthAntp-eGFP isoforms by
1469 *MS243*-Gal4 results in normal development of the fly notum (A), whereas induction of
1470 an exogenous repressor (mCitrine-SynthScr) results in severe malformations,
1471 indicated by developmental defects of the adult cuticle (B). Flies of both genotypes in
1472 (A) and (B) die as pharate adults. (C) Induction of mCitrine-SynthScr in the antennal
1473 disc results in complete transformations of antenna to tarsus as the induction of
1474 SynthAntp-eGFP (Fig. 6A). (D-D') *MS243*-Gal4-mediated expression of repressing or
1475 activating SynthAntp isoforms results in repression of the Antp endogenous protein in
1476 the notum region of the wing disc. (E-E') Ectopic expression of SynthScr in the wing
1477 disc using *ptc*-Gal4 results in drastic reduction of endogenous Antp protein levels. (F-
1478 F') Ectopic expression of SynthScr by *MS243*-Gal4 in the notum results in repression
1479 of the Antp protein. (G-G') SynthScr represses Antp at the transcriptional level, as
1480 indicated by the absence of transcription of the Antp P1 reporter (white arrows in (G)).
1481 (H-H') Unlike SynthAntp, SynthScr is not able to activate the Antp P1 promoter reporter
1482 transcription (H), when induced by *Dll* (MD23)-Gal4. (I-I') SynthScr is not able to
1483 downregulate its own endogenous protein levels upon overexpression by *Dll* (MD23)-
1484 Gal4. Dashed line in (I') outlines the region of high overlap between the overexpressed
1485 SynthScr and endogenous Scr stainings. (J-J') Negative control staining for the
1486 induction of eGFP in the wing disc notum by *MS243*-Gal4, which fails to repress
1487 endogenous Antp protein. Dashed lines in (D), (E) and (F) outline the regions of
1488 ectopic overexpression of SynthAntp or SynthScr, where endogenous Antp is
1489 repressed, whereas the dashed line in (I') outlines the region of overlap between

1490 SynthScr overexpression and endogenous expression of the Scr protein, where no
1491 repression is observed. Scale bars denote $100\ \mu m$, unless otherwise indicated.
1492

1493 **Supplemental information**

1494 Supplement 1: Background on Fluorescence Microscopy Imaging and FCS

1495 Two individually modified instruments (Zeiss, LSM 510 and 780, ConfoCor 3)
1496 with fully integrated FCS/CLSM optical pathways were used for imaging. The detection
1497 efficiency of CLSM imaging was significantly improved by the introduction of APD
1498 detectors. As compared to PMTs, which are normally used as detectors in
1499 conventional CLSM, the APDs are characterized by higher quantum yield and
1500 collection efficiency – about 70 % in APDs as compared to 15 – 25 % in PMTs, higher
1501 gain, negligible dark current and better efficiency in the red part of the spectrum.
1502 Enhanced fluorescence detection efficiency enabled image collection using fast
1503 scanning ($1 - 5\ \mu s/pixel$). This enhances further the signal-to-noise-ratio by avoiding
1504 fluorescence loss due to triplet state formation, enabling fluorescence imaging with
1505 single-molecule sensitivity. In addition, low laser intensities ($150 - 750\ \mu W$) could be
1506 applied for imaging, significantly reducing the photo-toxicity (Vukojevic et al., 2008).

1507 FCS measurements are performed by recording fluorescence intensity
1508 fluctuations in a very small, approximately ellipsoidal observation volume element
1509 (OVE) (about $0.2\mu m$ wide and $1\mu m$ long) that is generated in imaginal disc cells by
1510 focusing the laser light through the microscope objective and by collecting the
1511 fluorescence light through the same objective using a pinhole in front of the detector
1512 to block out-of-focus light. The fluorescence intensity fluctuations, caused by
1513 fluorescently labeled molecules passing through the OVE are analyzed using temporal
1514 autocorrelation analysis.

In temporal autocorrelation analysis we first derive the autocorrelation function $G(\tau)$:

$$G(\tau) = 1 + \frac{\langle \delta I(t) \cdot \delta I(t+\tau) \rangle}{\langle I(t) \rangle^2} \quad \text{(S1)},$$

where $\delta I(t) = I(t) - \langle I(t) \rangle$ is the deviation from the mean intensity at time t and $\delta I(t+\tau) = I(t+\tau) - \langle I(t) \rangle$ is the deviation from the mean intensity at time $t + \tau$. For further analysis, an autocorrelation curve is derived by plotting $G(\tau)$ as a function of the lag time, i.e. the autocorrelation time τ.

To derive information about molecular numbers and their corresponding diffusion time, the experimentally obtained autocorrelation curves are compared to autocorrelation functions derived for different model systems, and the model describing free three dimensional (3D) diffusion of two components and triplet formation was identified as the simplest and best suited for fitting the experimentally derived autocorrelation curves, and was used throughout:

$$G(\tau) = 1 + \frac{1}{N}\left(\frac{1-y}{\left(1+\frac{\tau}{\tau_{D_1}}\right) \cdot \sqrt{1+\frac{w_{xy}^2 \tau}{w_z^2 \tau_{D_1}}}} + \frac{y}{\left(1+\frac{\tau}{\tau_{D_2}}\right) \cdot \sqrt{1+\frac{w_{xy}^2 \tau}{w_z^2 \tau_{D_2}}}} \right) \cdot \left(1 + \frac{T}{1-T} \cdot e^{-\frac{\tau}{\tau_T}} \right)$$

(S2)

In the above equation, *N* is the average number of molecules in the OVE; *y* is the fraction of the slowly moving Antp-eGFP molecules; τ_{D_1} is the diffusion time of the free Antp-eGFP molecules; τ_{D_2} is the diffusion time of Antp-eGFP molecules undergoing nonspecific interactions with the DNA; w_{xy} and w_z are radial and axial parameters, respectively, related to spatial properties of the OVE; T is the average equilibrium fraction of molecules in the triplet state; and τ_T the triplet correlation time related to rate constants for intersystem crossing and the triplet decay. Spatial

1537 properties of the detection volume, represented by the square of the ratio of the axial
1538 and radial parameters ($\left(\frac{w_z}{w_{xy}}\right)^2$), are determined in calibration measurements
1539 performed using a solution of Rhodamine 6G for which the diffusion coefficient (D) is
1540 known to be $D_{Rh6G} = 4.1 \cdot 10^{-10}\, m^2 s^{-1}$ (Muller et al., 2008). The diffusion time, τ_D,
1541 measured by FCS, is related to the translation diffusion coefficient *D* by:

1542 $$\tau_D = \frac{w_{xy}^2}{4D} \text{ (S3).}$$

1543 To establish that Antp molecules diffusing through the OVE are the underlying
1544 cause of the recorded fluorescence intensity fluctuations, we plotted the characteristic
1545 decay times τ_{D1} and τ_{D2}, obtained by FCS, as a function of the total concentration of
1546 Antp molecules (Supplemental Fig. S2). We observed that both characteristic decay
1547 times remain stable for increasing total concentration of Antp molecules, signifying that
1548 the underlying process triggering the fluorescence intensity fluctuations is diffusion of
1549 fluorescent Antp molecules through the OVE (which is independent of the total
1550 concentration of Antp molecules).

1551 In order to ascertain that the interpretation and fitting of FCS curves is correct,
1552 we have: (1) tested several laser intensities in our FCS measurements and have
1553 utilized the highest laser intensity, for which the highest counts per second and
1554 molecule (CPSM) were obtained, while photobleaching was not observed; (2) we have
1555 established that CPSM do not change among FCS measurements performed in cells
1556 expressing Antp endogenously, or overexpressed with different Gal4 drivers.
1557 Moreover, we have previously shown that both characteristic decay times increase
1558 when the size of the OVE is increased (Fig. 4 in (Vukojevic et al., 2010)). Together,
1559 these lines of evidence indicate that both short and long characteristic decay times are
1560 generated by molecular diffusion rather than by photophysical and/or chemical

1561 processes such as eGFP protonation/deprotonation; (3) we have ascertained that the
1562 long characteristic decay time of our FCS measurements is not the result of
1563 photobleaching and that differences in the relative amplitudes of the fast and slow
1564 diffusing components reflect differences in their concentrations among cells.

1565 While we have taken all possible precautions to ascertain that the correct model
1566 for FCS data fitting is applied, some inevitable limitations still remain. For example,
1567 FCS cannot account for Antp molecules with irreversibly photobleached fluorophores
1568 or with fluorophores residing for various reasons in dark states. In addition, FCS
1569 cannot account for Antp molecules associated with large immobile structures, such as
1570 specifically bound Antp molecules. These molecules contribute to the overall
1571 background signal, but they do not give rise to fluorescence intensity fluctuations. As
1572 a consequence, transcription factor concentration can be somewhat underestimated
1573 by FCS. In contrast, the number of transcription factor molecules may also be
1574 overestimated by FCS, when high background signal as compared to fluorescence
1575 intensity may lead to an artificially low amplitude of FCS curves, and, hence,
1576 overestimation of molecular numbers. To avoid artifacts due to photobleaching, the
1577 incident laser intensity was kept as low as possible but sufficiently high to allow high
1578 signal-to-noise ratio. This is because photobleaching of fluorophores may induce
1579 errors in the measurements of molecular numbers and lateral diffusion, yielding both
1580 smaller number of molecules and shorter values of τ_D, and hence apparently larger
1581 diffusion coefficients. Finally, contribution of brightness, *i.e.* brightness squared, to the
1582 correlation function was not analyzed, which may in turn affect quantification of Antp
1583 numbers.

1584

1585 Supplement 2: Calculation of the concentration of endogenous TFs and average
1586 number of molecules in imaginal disc cell nuclei from FCS measurements (exemplified
1587 for Antp)

1588 Experimentally derived FCS curves were analyzed by fitting, using the model
1589 function for free three-dimensional diffusion of two components with triplet formation,
1590 equation (S2), to derive the average number of molecules in the OVE (N); the diffusion
1591 time of the free Antp-eGFP molecules (τ_{D_1}); the diffusion time of Antp-eGFP molecules
1592 undergoing interactions with the DNA (τ_{D_2}); and the relative fraction of Antp-eGFP
1593 molecules that are engaged in interactions with chromatin and therefore move slowly
1594 (y).

1595 In order to translate the average number of molecules in the OVE (N) into molar
1596 concentration, the size of the OVE, *i.e.* the axial and radial parameters (w_z and w_{xy},
1597 respectively) were determined in calibration experiments with Alexa488 or Rhodamine
1598 6G dyes, using equation (S3). The volume of the OVE, approximated by a prolate
1599 ellipsoid, was determined as follows:

1600 $$V_{OVE} = \pi^{\frac{3}{2}} \cdot w_{xy}^2 \cdot z_0 = 5.57 \cdot 0.1847^{\mathbf{2}} \cdot 1 = 0.223 \cdot 10^{-18}\, m^3 = 0.22 \cdot 10^{-15} L \text{ (S4).}$$

1601

1602 Thereafter, the average number of molecules in the OVE (N) was converted
1603 into molar concentration (C) using the relationship:

1604 $$C = \frac{N}{N_A \cdot V_{OVE}} \text{ (S5),}$$

1605 where N_A is the Avogadro number ($6.022 \cdot 10^{23} mol^{-1}$), which indicated that one
1606 molecule in the OVE corresponds on the average to $8.74\, nM$ concentration of
1607 fluorescent molecules in the nucleus.

Finally, the concentration of non-specifically bound TF molecules ($[DNA - Antp - eGFP]_{ns}$) was calculated by multiplying the relative amplitude of the second component (y), determined by fitting the experimental autocorrelation curves with the model function (S2), with the total concentration of Antp-eGFP, $C = [Antp - eGFP]_0$, which was determined from the amplitude of the autocorrelation curve at zero lag time:

$$[DNA - Antp - eGFP]_{ns} = y \cdot [DNA - Antp - eGFP]_0 \text{ (S6).}$$

The concentration of non-specifically bound TF molecules ($[DNA - Antp - eGFP]_{ns}$) was then plotted as a function of the total concentration of Antp-eGFP ($[Antp - eGFP]_0$) to yield the graphs shown in Supplemental Fig. S10C,D.

In order to estimate the total number of molecules in the wing disc imaginal cell nuclei, we applied the following calculation. The wing disc nuclei within the Antp expression domain (prescutum precursors) are not spherical, but rather ellipsoidal. Their axes were determined by fluorescence imaging to be $1.4\,\mu m$ in the transverse dimension and $2.8\,\mu m$ in the longitudinal. The volume of the nucleus was approximated by the volume of a prolate ellipsoid:

$$V_{nucleus} = \frac{4}{3}\pi a^2 b = \frac{4}{3} \cdot 3.14 \cdot (1.4 \cdot 10^{-6})^2 \cdot 2.8 \cdot 10^{-\mathbf{6}}\, m^3 = 22.99 \cdot 10^{-18}\, m^3 = 22.99 \cdot 10^{-15}\, L \text{ (S7).}$$

Therefore, the OVE represents roughly $1/121$ of the nuclear volume:

$$\frac{V_{nucleus}}{V_{OVE}} = 121 \text{ (S8)}$$

and the number of molecules in Antp-eGFP nuclei is on the average $57.37 \cdot 121 \approx 6942$ molecules in third instar wing and $127 \cdot 121 \approx 15367$ in third instar leg discs.

Generalizing, with known axial and radial parameters of the OVE and calculation of the transverse and longitudinal dimensions of the nucleus, the total number of molecules of transcription factor in the nucleus can be estimated:

$$N_{TF\ molecules}^{total} = \frac{V_{nucleus}}{V_{OVE}} \cdot N_{TF\ molecules}^{OVE} = \frac{\frac{4}{3}\pi a^2 b N_{TF\ molecules}^{OVE}}{\pi^{\frac{3}{2}} \cdot w_{xy}^2 \cdot z_0} = \frac{4a^2 b N_{TF\ molecules}^{OVE}}{3\sqrt{\pi} \cdot w_{xy}^2 \cdot z_0} \quad \text{(S9)}$$

<u>Supplement 3: Calculation of the ratio of apparent Antp dissociation constant for short and long linker Antp isoforms from FCS measurements on ectopically expressed Antp</u>

Antp undergoes both specific and non-specific interactions with DNA, with non-specific interactions preceding the specific ones and effectively assisting the binding to a specific target site by facilitated diffusion (Halford and Marko, 2004). The searching for specific binding sites can be described as a two-step process of consecutive reactions (Vukojevic et al., 2010):

$$\begin{aligned} DNA_{ns} + Antp - eGFP &\underset{k_{-ns}}{\overset{k_{ns}}{\Longleftrightarrow}} (DNA - Antp - eGFP)_{ns} \\ (DNA - Antp - eGFP)_{ns} + DNA_s &\underset{k_{-s}}{\overset{k_s}{\Longleftrightarrow}} (DNA - Antp - eGFP)_s \end{aligned} \quad \text{(S10).}$$

The turnover rate for the non-specific complex is:

$$\frac{d[(DNA-Antp-eGFP)_{ns}]}{dt} = k_{ns} \cdot [DNA_{ns}] \cdot [Antp - eGFP] - (k_{-ns} + k_s \cdot [DNA_s]) \cdot [(DNA - Antp - eGFP)_{ns}] + k_{-s} \cdot [(DNA - Antp - eGFP)_s] \quad \text{(S11).}$$

Assuming a quasi-steady state approximation:

$$\frac{d[(DNA-Antp-eGFP)_{ns}]}{dt} = 0 \quad \text{(S12),}$$

$$(k_{-ns} + k_s \cdot [DNA_s]) \cdot [(DNA - Antp - eGFP)_{ns}] = k_{ns} \cdot [DNA_{ns}] \cdot [Antp - eGFP] + k_{-s} \cdot [(DNA - Antp - eGFP)_s] \quad \text{(S13).}$$

Using the mass balance equation to express the concentration of the free TF:

$$[Antp - eGFP] = [Antp - eGFP]_0 - [(DNA - Antp - eGFP)_{ns}] - [(DNA - Antp - eGFP)_s] \quad \text{(S14)}$$

and assuming that:

$$[DNA]_{ns} \approx [DNA]_0 \text{ (S15)},$$

equation (S13) becomes:

$$(k_{-ns} + k_s \cdot [DNA_s]) \cdot [(DNA - Antp - eGFP)_{ns}] = k_{ns} \cdot [DNA]_0 \cdot ([Antp - eGFP]_0 - [(DNA - Antp - eGFP)_{ns} - [(DNA - Antp - eGFP)_s]) + k_{-s} \cdot [(DNA - Antp - eGFP)_s] \text{ (S16)},$$

$$(k_{-ns} + k_s \cdot [DNA_s] + k_{ns} \cdot [DNA]_0) \cdot [(DNA - Antp - eGFP)_{ns}] = k_{ns} \cdot [DNA]_0 \cdot ([Antp - eGFP]_0 - [(DNA - Antp - eGFP)_s]) + k_{-s} \cdot [(DNA - Antp - eGFP)_s] \text{ (S17)},$$

$$(k_{-ns} + k_s \cdot [DNA_s] + k_{ns} \cdot [DNA]_0) \cdot [(DNA - Antp - eGFP)_{ns}] = k_{ns} \cdot [DNA]_0 \cdot [Antp - eGFP]_0 - (k_{ns} \cdot [DNA]_0 - k_{-s}) \cdot [(DNA - Antp - eGFP)_s] \text{ (S18)},$$

$$[(DNA - Antp - eGFP)_{ns}] = \frac{k_{ns} \cdot [DNA]_0}{k_{-ns} + k_s \cdot [DNA_s] + k_{ns} \cdot [DNA]_0} \cdot [Antp - eGFP]_0 - \frac{k_{ns} \cdot [DNA]_0 - k_{-s}}{k_{-ns} + k_s \cdot [DNA_s] + k_{ns} \cdot [DNA]_0} \cdot [(DNA - Antp - eGFP)_s] \text{ (S19)}.$$

According to equation (S19) and the FCS data presented in Supplemental Fig. S10, the slope of the linear dependence for:

a) the short linker Antp isoform gives:

$$\frac{k_{ns}^{short\ linker} \cdot [DNA]_0}{k_{-ns}^{short\ linker} + k_s^{short\ linker} \cdot [DNA_s] + k_{ns}^{short\ linker} \cdot [DNA]_0} = 0.34 \text{ (S20)}$$

and the intercept:

$$\frac{k_{ns}^{short\ linker} \cdot [DNA]_0 - k_{-s}^{short\ linker}}{k_{-ns}^{short\ linker} + k_s^{short\ linker} \cdot [DNA_s] + k_{ns}^{short\ linker} \cdot [DNA]_0} \cdot [(DNA - Antp - eGFP)_s] = 5.31\ nM \text{ (S21)}.$$

If $k_{-s}^{short\ linker}$ is small compared to $k_{ns}^{short\ linker} \cdot [DNA]_0$ and can therefore be neglected, then:

$$0.34 \cdot [(DNA - Antp - eGFP)_s] = 5.31\ nM \text{ (S22)}.$$

Thus, the concentration of specific complex between Antp-eGFP and DNA in the wing disc cell nuclei can be estimated to be:

$$[(DNA - Antp - eGFP)_s] = 15.62\ nM \text{ (S23).}$$

The average concentration of free-diffusing Antp-eGFP molecules is determined as follows:

$$[Antp - eGFP]_{free} = [Antp - eGFP]_0 - [(DNA - Antp - eGFP)_{ns}] - [(DNA - Antp - eGFP)_s] = [Antp - eGFP]_0 - (0.34 \cdot [Antp - eGFP]_0 - 5.31) - [(DNA - Antp - eGFP)_s] = 785.28 - 0.34 \cdot 785.28 + 5.31 - 15.62 = 507.97nM \text{ (S24).}$$

Using the experimentally determined concentration of specific DNA–Antp-eGFP complexes (equation (S23)), we could estimate the dissociation constant for the specific DNA–Antp-eGFP, as a function of the total concentration of specific Antp binding sites, to be:

$$K_{d,Antp}^{short\ linker} = \frac{[DNA_s]_{free} \cdot [Antp-eGFP]_{free}}{[(DNA-Antp-eGFP)_s]} = \frac{[DNA_s]_{free} \cdot 507.97}{15.62} \approx ([DNA_s]_{free} \cdot 32.52)\ nM \text{ (S25).}$$

b) The long linker Antp isoform gives:

$$\frac{k_{ns}^{long\ linker} \cdot [DNA]_0}{k_{-ns}^{long\ linker} + k_s^{long\ linker} \cdot [DNA_s] + k_{ns}^{long\ linker} \cdot [DNA]_0} = 0.24 \text{ (S26).}$$

and the intercept:

$$\frac{k_{ns}^{long\ linker} \cdot [DNA]_0 - k_{-s}^{long\ linker}}{k_{-ns}^{long\ linker} + k_s^{long\ linker} \cdot [DNA_s] + k_{ns}^{long\ linker} \cdot [DNA]_0} \cdot [(DNA - Antp - eGFP)_s] = 3.28\ nM \text{ (S27).}$$

If $k_{-s}^{long\ linker}$ is small compared to $k_{ns}^{long\ linker} \cdot [DNA]_0$ and can therefore be neglected, then:

$$0.24 \cdot [(DNA - Antp - eGFP)_s] = 3.28\ nM \text{ (S28).}$$

Thus, the concentration of specific complex between Antp-eGFP and DNA in the wing disc cell nuclei can be estimated to be:

$$[(DNA - Antp - eGFP)_s] = 13.67\ nM \text{ (S29).}$$

The average concentration of free-diffusing Antp-eGFP molecules is determined as follows:

$$[Antp-eGFP]_{free} = [Antp-eGFP]_0 - [(DNA-Antp-eGFP)_{ns}] - [(DNA-Antp-eGFP)_s] = [Antp-eGFP]_0 - (0.24 \cdot [Antp-eGFP]_0 - 3.28) - [(DNA-Antp-eGFP)_s] = 1382.95 - 0.24 \cdot 785.28 + 3.28 - 13.67 = 1040.65nM \text{ (S30).}$$

Using the experimentally determined concentration of specific DNA–Antp-eGFP complexes (equation (S29)), we could estimate the dissociation constant for the specific DNA–Antp-eGFP, as a function of the total concentration of specific Antp binding sites, to be:

$$K_{d,Antp}^{long\ linker} = \frac{[DNA_s]_{free} \cdot [Antp-eGFP]_{free}}{[(DNA-Antp-eGFP)_s]} = \frac{[DNA_s]_{free} \cdot 1040.65}{13.67} \approx ([DNA_s]_{free} \cdot 76.13)\ nM \text{ (S31).}$$

From equations (S25) and (S31), we could calculate the ratio of the apparent equilibrium dissociation constants for specific interactions to be:

$$\frac{K_{d,Antp}^{long\ linker}}{K_{d,Antp}^{short\ linker}} = \frac{[DNA_s]_{free}^{long\ linker} \cdot 76.13}{[DNA_s]_{free}^{short\ linker} \cdot 32.52} = 2.34 \cdot \frac{([DNA]_0 - [(DNA-Antp-eGFP)_s]_{long\ linker})}{([DNA]_0 - [(DNA-Antp-eGFP)_s]_{short\ linker})} = 2.34 \frac{[DNA]_0 - 13.67}{[DNA]_0 - 15.62} \text{ (S32).}$$

Therefore:

$$K_{d,Antp}^{s,long\ linker} > 2.34 \cdot K_{d,Antp}^{s,short\ linker} \text{ (S33),}$$

independently of the total concentration of Antp binding sites in the nucleus. Although the affinities of the ratio of the equilibrium dissociation constants does not depend on the total concentration of binding sites for Antp ($[DNA]_0$), its value is required for the calculation. For values close to $15.62\ nM$ ($[DNA]_0 \to 15.62\ nM$) with $[DNA]_0 > 15.62\ nM$, the ratio of the apparent equilibrium dissociation constants will be high:

$$\lim_{[DNA]_0 \to 15.62} \left(2.34 \frac{[DNA]_0 - 13.67}{[DNA]_0 - 15.62}\right) = +\infty \text{ (S34),}$$

indicating that, in this case, the short linker isoform will bind the Antp binding sites with much higher affinity than the long linker isoform.

In contrast, for considerably higher values of $[DNA]_0$ than $15.62\ nM$ ($[DNA]_0 \rightarrow +\infty$), the ratio of apparent equilibrium dissociation constants will be:

$$\lim_{[DNA]_0 \rightarrow +\infty} \left(2.34 \frac{[DNA]_0 - 13.67}{[DNA]_0 - 15.62}\right) = \lim_{[DNA]_0 \rightarrow +\infty} \left(2.34 \frac{[DNA]_0 \left(1 - \frac{13.67}{[DNA]_0}\right)}{[DNA]_0 \left(1 - \frac{15.62}{[DNA]_0}\right)}\right) =$$

$$\lim_{[DNA]_0 \rightarrow +\infty} \left(2.34 \frac{1 - \frac{13.67}{[DNA]_0}}{1 - \frac{15.62}{[DNA]_0}}\right) = 2.34 \text{ (S35)},$$

indicating a roughly 2.5fold higher affinity of the short linker repressive isoform.

In addition, equations (S20) and (S26) contain information about the ratio of the apparent equilibrium dissociation constants for nonspecific interactions [(Vukojevic et al., 2010), Fig. 5, solid red line *versus* dashed red line]. Thus, the slopes of the linear regression lines (Supplemental Fig. S10C-D'), give:

$$\frac{k_{ns}^{short\ linker} \cdot [DNA]_0}{k_{-ns}^{short\ linker} + k_{ns}^{short\ linker} \cdot [DNA]_0} = 0.34 \text{ (S36)}$$

$$\frac{k_{ns}^{long\ linker} \cdot [DNA]_0}{k_{-ns}^{long\ linker} + k_{ns}^{long\ linker} \cdot [DNA]_0} = 0.24 \text{ (S37)}$$

From these relationships, the ratio of the apparent equilibrium dissociation constants for nonspecific interactions can be estimated to be:

$$K_{d,Antp}^{ns,long\ linker} > 1.63 \cdot K_{d,Antp}^{ns,short\ linker} \text{ (S38)}.$$

Thus, our analysis shows that the short linker, which is the preferentially repressing isoform, binds with higher affinity (lower K_d) to both specific and nonspecific binding sites on the DNA [(S33) and (S38), respectively]. This, in turn, implies that the short linker is also more efficient in searching for specific TF binding sites, as evident from the lower dissociation constant for nonspecific DNA interactions of the short linker isoform (Sela and Lukatsky, 2011; Soltani et al., 2015), and that it binds with lower apparent dissociation constant to specific binding sites on the DNA.

1746

1747 Supplement 4: Stochastic modeling of Antennapedia expression

1748 In the following, we develop a simple mathematical model that is able to explain
1749 the behavior of Antennapedia (Antp) expression at early and late developmental
1750 stages. The Antp promoter is modeled as a continuous-time Markov chain with three
1751 distinct transcriptional states. In the absence of Antp, the promoter is in an unbound
1752 state ("U"), in which transcription is inactive. From this state, the promoter can switch
1753 to a transcriptionally active state "A" at a rate, assumed to be proportional to the
1754 concentration of the long-linker, activating isoform of Antp. Analogously, repression of
1755 the promoter by the short-linker isoform of Antp is modeled by an additional
1756 transcriptionally inactive state "R", which can be reached from state "U" at a rate
1757 proportional to the concentration of that isoform. The corresponding reverse transitions
1758 from states "R" and "A" back into state "U" are assumed to happen at a constant rate
1759 k. Since the activating isoform can potentially also repress the promoter, we assume
1760 that state "R" can be reached also from the active state "A". Similarly, we model a
1761 potential link also in the reverse direction from state "A" to "R". Depending on the model
1762 variant, we assume this transition happens either at a constant rate k (competitive
1763 promoter model) or at a rate proportional to the concentration of the repressing isoform
1764 of Antp (non-competitive promoter model). In the latter case, repression through short-
1765 linker isoforms can take place even if a long-linker isoform is already bound to the
1766 promoter. As we have demonstrated in Fig. 5A,B, the two model variants yield
1767 qualitative differences in Antp expression. For the sake of illustration, the following
1768 description focuses on the non-competitive model variant but we remark that the
1769 competitive model can be derived analogously.

At a particular time point t, the transcription rate of Antp is determined by the current state of the promoter, i.e., $\lambda(t)\epsilon\{0, \lambda_A, 0\}$, with λ_A as the transcription rate associated with state "A". In line with our experimental findings, we assume that transcripts are spliced into the activating and repressing isoforms at different rates ρ_A and ρ_R, respectively. This allows us to capture the imbalance between the two isoforms that was revealed by our FCS data. The overall expression rates for the two isoforms of Antp are then given by $h_A(t) = \lambda(t)Z\rho_A$ and $h_R(t) = \lambda(t)Z\rho_R$, whereas Z is a random variable that accounts for extrinsic variability in gene expression rates (Zechner et al., 2012). In all of our analyses, we model Z as a Gamma random variable, i.e., $Z \sim \Gamma(\alpha, \beta)$ with α and β as shape and inverse scale parameters of that distribution. In summary, we describe the auto-regulatory circuit of Antp expression by a Markovian reaction network of the form:

$$U \underset{k}{\overset{\gamma_A X_A(t)^n}{\rightleftharpoons}} A$$

$$U \underset{k}{\overset{\gamma_R X_R(t)^n}{\rightleftharpoons}} R$$

$$A \underset{k}{\overset{\gamma_R X_R(t)^n}{\rightleftharpoons}} R$$

$$\emptyset \xrightarrow{h_A(t)} X_A \xrightarrow{1/\tau} \emptyset$$

$$\emptyset \xrightarrow{h_R(t)} X_R \xrightarrow{1/\tau} \emptyset$$

(S39),

with $X_A(t)$and $X_R(t)$ as the concentration of the activating and repressing isoforms of Antp, τ as the protein half-live and n as a coefficient accounting for cooperativity in the binding of Antp to the promoter. The initial conditions $X_A(0)$ and $X_R(0)$ were drawn randomly in accordance with our concentration measurements at early stages. In particular, we assume that the total amount of Antp X_{tot} in each cell is drawn from a

negative binomial distribution such that $X_{tot} \sim \mathcal{NB}(r,p)$, with $\mu_X = r(1-p)/p$ and $\eta_x^2 = 1/r(1-p)$ as the mean and squared coefficient of variation of this distribution. The total number of Antp molecules was then randomly partitioned into fractions of repressing and activating isoforms according to a Beta distribution. More specifically, we set $X_A(0) = WX_{tot}$ and $X_R(0) = (1-W)X_{tot}$ with $W \sim Beta(a,b)$. The parameters r, p, a and b were chosen based on our experimental data (see Table 1).

Due to the fact that Antp expression takes place at the timescale of several hours to days, we can further simplify our model from (S39). In particular, we can make use of a quasi-steady state assumption (Rao and Arkin, 2003), by assuming that promoter switching due to binding and unbinding of the different Antp isoforms occurs at a much faster timescale than production and degradation of Antp. As a consequence, we can replace the stochastic gene expression rates of the two isoforms by their expected value, whereas the expectation is taken with respect to the quasi-stationary distribution of the three-state promoter model. More precisely, we have:

$$h_A\,(t) \approx \mathbb{E}[\lambda(t)]Z\rho_A$$

$$h_R\,(t) \approx \mathbb{E}[\lambda(t)]Z\rho_R$$

(S40),

with $\mathbb{E}[\lambda(t)] = P_U 0 + P_A\lambda_A + P_R 0 = P_A\lambda_A$ as the quasi-stationary probabilities of finding the promoter in state “U”, “A” and “R”, respectively. These probabilities can be derived from the generator matrix of the three-state promoter model, which reads:

$$Q = \begin{pmatrix} -\gamma_A X_A(t)^n - \gamma_R X_R(t)^n & k & k \\ \gamma_A X_A(t)^n & -k - \gamma_R X_R(t)^n & k \\ \gamma_R X_R(t)^n & \gamma_R X_R(t)^n & -2k \end{pmatrix} \text{(S41).}$$

Assuming that $X_A(t)$ and $X_R(t)$ remain roughly constant on the timescale of the promoter, the quasi-stationary distribution can be determined by the null-space of Q, which is given by:

$$P_{QSS} = \begin{pmatrix} P_U \\ P_A \\ P_R \end{pmatrix} = \begin{pmatrix} \frac{k}{(k+\gamma_A X_A(t)^n+\gamma_R X_R(t)^n)} \\ \frac{k(2\gamma_A X_A(t)^n+\gamma_R X_R(t)^n)}{(2k+\gamma_R X_R(t)^n)(k+\gamma_A X_A(t)^n+\gamma_R X_R(t)^n)} \\ \frac{\gamma_R X_R(t)^n}{2k+\gamma_R X_R(t)^n} \end{pmatrix} \text{(S42)}.$$

Correspondingly, the expectation of $\lambda(t)$ becomes:

$$\mathbb{E}[\lambda(t)] = (0 \quad \lambda_A \quad 0)\begin{pmatrix} P_U \\ P_A \\ P_R \end{pmatrix} = \frac{k(2\gamma_A X_A(t)^n + \gamma_R X_R(t)^n)}{(2k + \gamma_R X_R(t)^n)(k + \gamma_A X_A(t)^n + \gamma_R X_R(t)^n)}$$

$$:= \bar{\lambda}(X_A(t), X_R(t)) \text{ (S43)}.$$

The simplified model of Antp expression can then be compactly written as two coupled birth-and-death processes:

$$\emptyset \xrightarrow{\bar{h}_A(X_A(t),X_R(t))} X_A \xrightarrow{1/\tau} \emptyset$$

$$\emptyset \xrightarrow{\bar{h}_R(X_A(t),X_R(t))} X_R \xrightarrow{1/\tau} \emptyset$$

(S44),

with $\bar{h}_A(X_A(t), X_R(t)) = \bar{\lambda}(X_A(t), X_R(t))Z\rho_A$ and $\bar{h}_R(X_A(t), X_R(t)) = \bar{\lambda}(X_A(t), X_R(t))Z\rho_R$.

In all our simulation studies, the circuit from (S44) was simulated using the τ-leaping algorithm (Gillespie, 2007). In case of the perturbation experiments, small modifications to the model were made. Overexpression of either of the two isoforms was reflected by changing the initial conditions of Antp. In particular, we added to the overexpressed isoform a random number of molecules drawn from a negative binomial distribution with mean μ_O and squared coefficient of variation η_O^2 (see Table 1). To account for overexpression of an external repressor S, we introduced a fourth state in the promoter model, from which no expression can take place. This state is assumed to be reachable from any of the other three states at a rate $\gamma_S S(t)^{n_S}$ with $S(t)$ as the concentration of the external repressor at time t and n_S as a coefficient accounting for cooperativity in the binding of the repressor to the promoter. For simplicity, we

assumed $n_S = n$ in our case studies. To account for cell-to-cell variability in the repressor concentration, the latter was initialized randomly according to a Poisson distribution, i.e., $S(t_0) \sim Pois(Z\mu_S)$ with μ_S as the average repressor abundance and Z as the Gamma-distributed random variable defined above. Furthermore, repressor molecules were assumed to have an average lifetime of τ_S, i.e., $S \xrightarrow{\tau_S^{-1}} \emptyset$.

The corresponding reaction rates of Antp expression were determined analogously to equations (S41-S43). Table 1 summarizes the parameters used for each of the simulation studies.

Table 1: Parameters used for simulating the stochastic model of Antp expression

Parameter	μ_X	η_x^2	μ_O	η_O^2	a	b	τ	k	γ_A	γ_R	λ_A	ρ_A	ρ_R	α	β	γ_S	μ_S	τ_S
Unit	–	–	–	–	–	–	h	min^{-1}	min^{-1}	min^{-1}	min^{-1}	–	–	–	–	–	–	h
Fig. 5 H, I, J	$1.5e3$	0.3	–	–	18	12	12[a]	1	$1.0e-8$	$1.6e-7$	150	0.8	1.5	2	2	–	–	–
Fig. 5 K, L	$1.5e3$	0.3	–	–	18	12	12	1	0.25	1	150	0.8	1.5	2	$1-1000$	–	–	–
Fig. 6 D, E[b]	$1.5e3$	0.3	$6e4$	0.3	18	12	12	1	0.25	0	150	0.8	1.5	2	2	–	–	–
Fig. 6 G, H[c]	$1.5e3$	0.3	$4e4$	0.3	18	12	12	1	0.25	0	150	0.8	1.5	2	2	–	–	–
Fig. 6 L, M[d]	$6e2$	0.35	–	–	18	12	12	1	0.25	1	150	0.8	1.5	2	2	$1e-4$	$6e4$	2

[a]Experimentally determined value from (Dworkin et al., 2007)

[b]Overexpression of X_R

[c]Overexpression of X_A

[d]Overexpression of external repressor

Figure 1

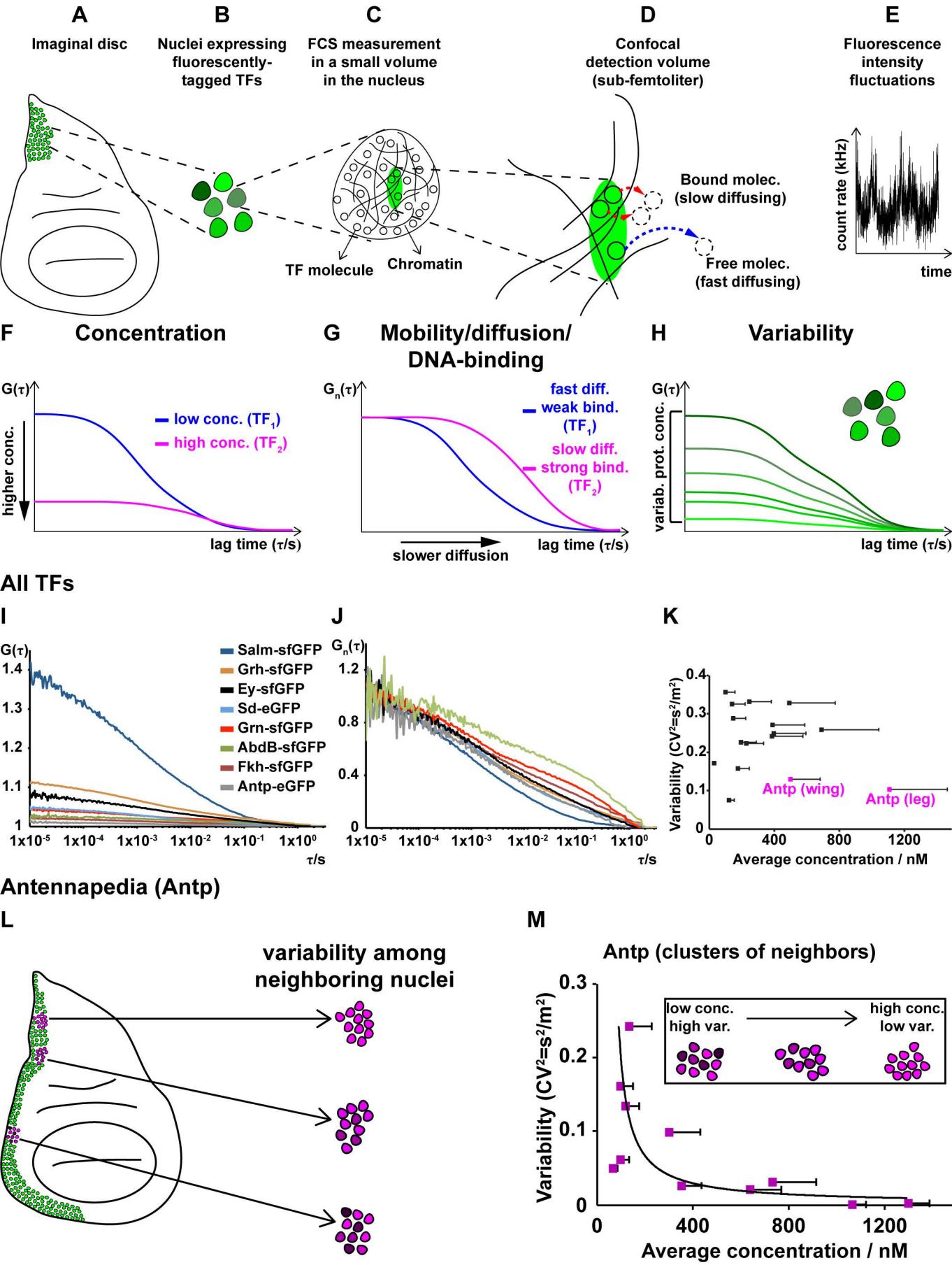
A
Imaginal disc
B
Nuclei expressing fluorescently-tagged TFs
C
FCS measurement in a small volume in the nucleus
D
Confocal detection volume (sub-femtoliter)
E
Fluorescence intensity fluctuations
TF molecule
Chromatin
Bound molec. (slow diffusing)
Free molec. (fast diffusing)
count rate (kHz)
time
F Concentration
G Mobility/diffusion/ DNA-binding
H Variability
G(τ)
higher conc.
low conc. (TF1)
high conc. (TF2)
lag time (τ/s)
Gn(τ)
fast diff.
weak bind. (TF1)
slow diff.
strong bind. (TF2)
slower diffusion
variab. prot. conc.
All TFs
I
J
K
Salm-sfGFP
Grh-sfGFP
Ey-sfGFP
Sd-eGFP
Grn-sfGFP
AbdB-sfGFP
Fkh-sfGFP
Antp-eGFP
τ/s
Variability (CV²=s²/m²)
Antp (wing)
Antp (leg)
Average concentration / nM
Antennapedia (Antp)
L
variability among neighboring nuclei
M
Antp (clusters of neighbors)
low conc. high var.
high conc. low var.

Figure 2

Auto-repression: protein level

Ay>SynthAntp-eGFP

A

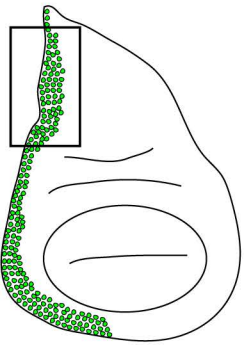

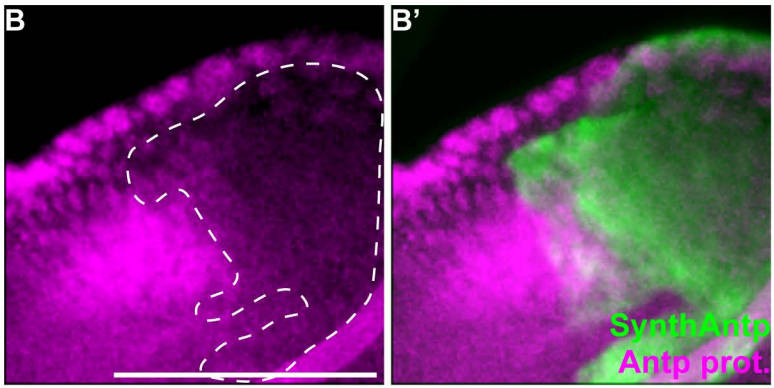

D

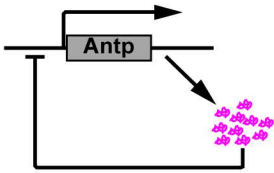

Auto-repression: transcripts level

Antp (P1)-lacZ, Ay>SynthAntp-eGFP

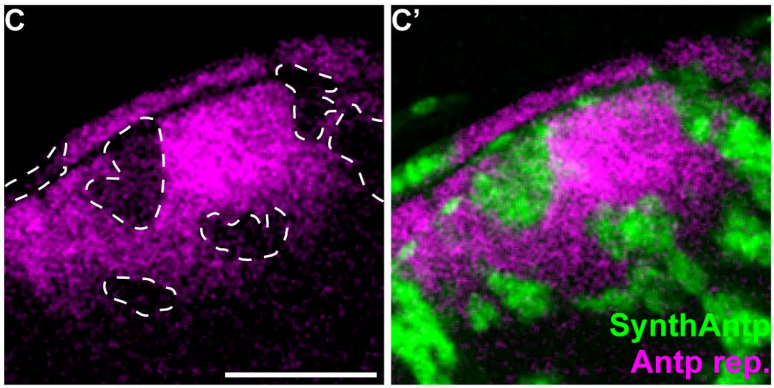

Auto-activation: transcripts level

Antp (P1)-lacZ, *Dll* (MD23)>SynthAntp-eGFP

E

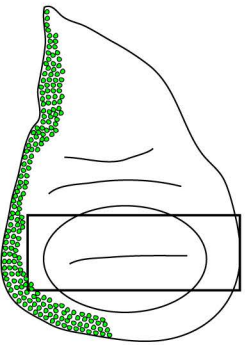

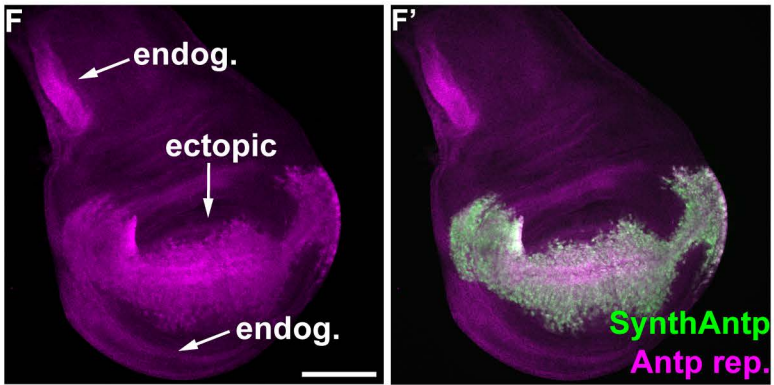

G

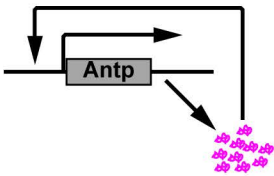

Figure 3

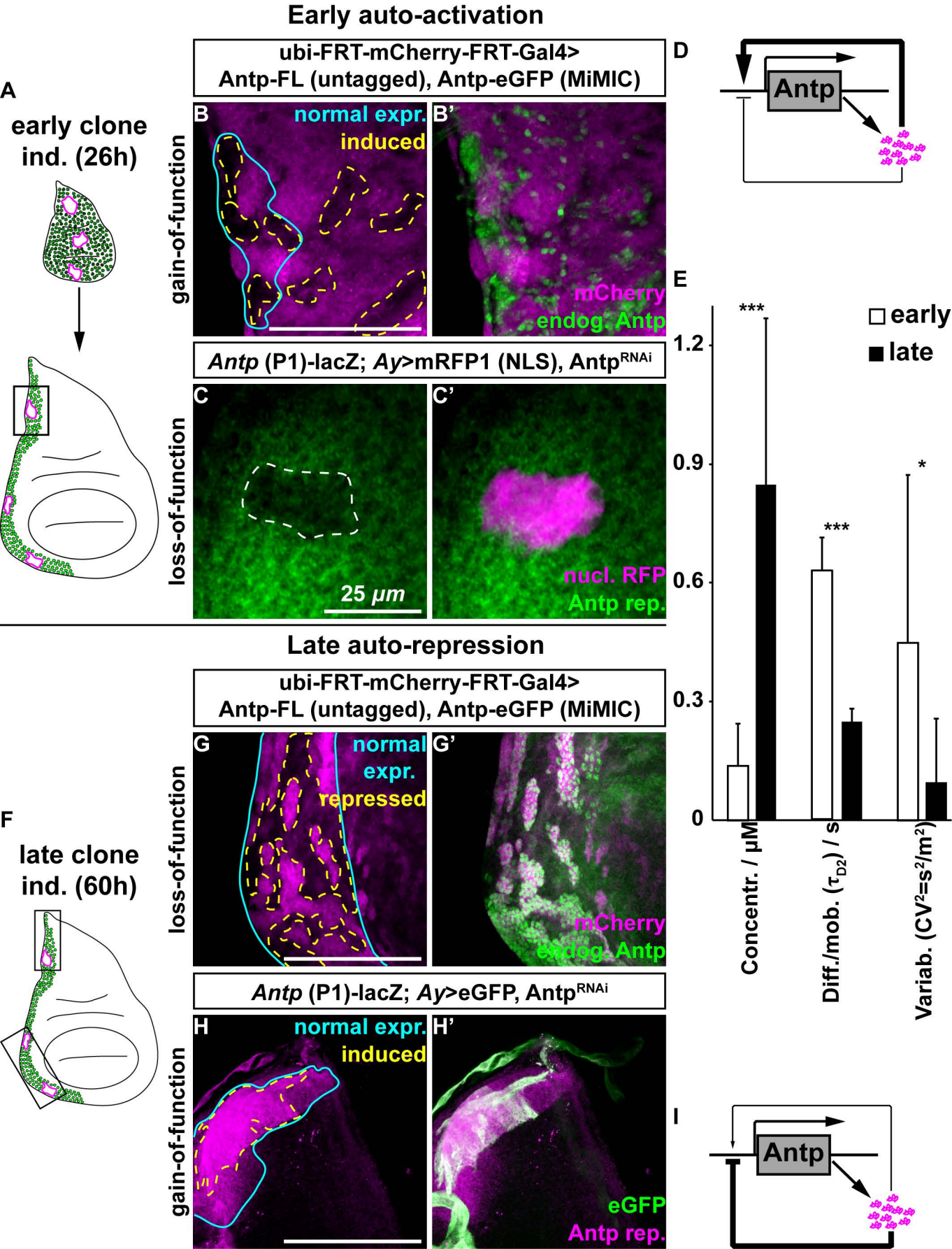
Early auto-activation
ubi-FRT-mCherry-FRT-Gal4>
Antp-FL (untagged), Antp-eGFP (MiMIC)
A
early clone
ind. (26h)
B
normal expr.
induced
B'
mCherry
endog. Antp
gain-of-function
Antp (P1)-lacZ; Ay>mRFP1 (NLS), Antp^RNAi
C
C'
25 μm
nucl. RFP
Antp rep.
loss-of-function
D
Antp
E
early
late
***
*
***
1.2
0.9
0.6
0.3
0
Concentr. / μM
Diff./mob. (τD2) / s
Variab. (CV²=s²/m²)
Late auto-repression
ubi-FRT-mCherry-FRT-Gal4>
Antp-FL (untagged), Antp-eGFP (MiMIC)
F
late clone
ind. (60h)
G
normal
expr.
repressed
G'
mCherry
endog. Antp
loss-of-function
Antp (P1)-lacZ; Ay>eGFP, Antp^RNAi
H
normal expr.
induced
H'
eGFP
Antp rep.
gain-of-function
I
Antp

Figure 4

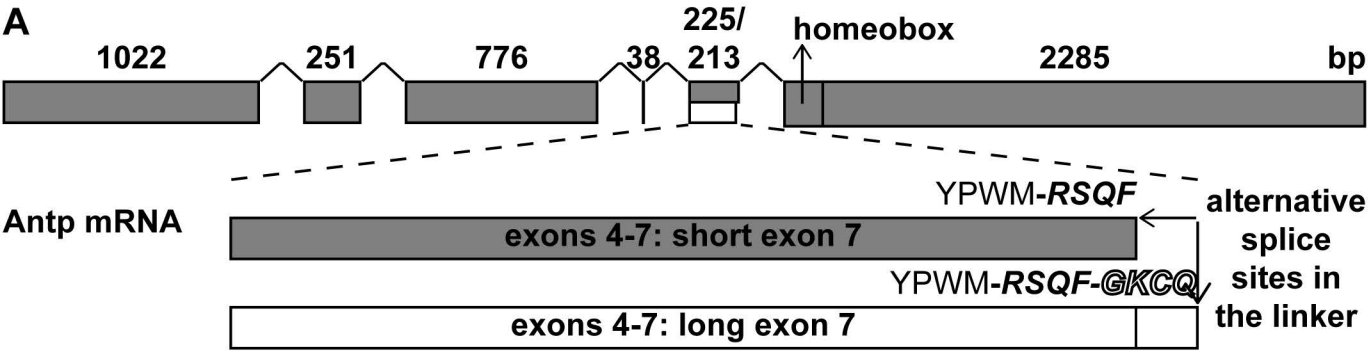

Long linker isoform (preferential activator)

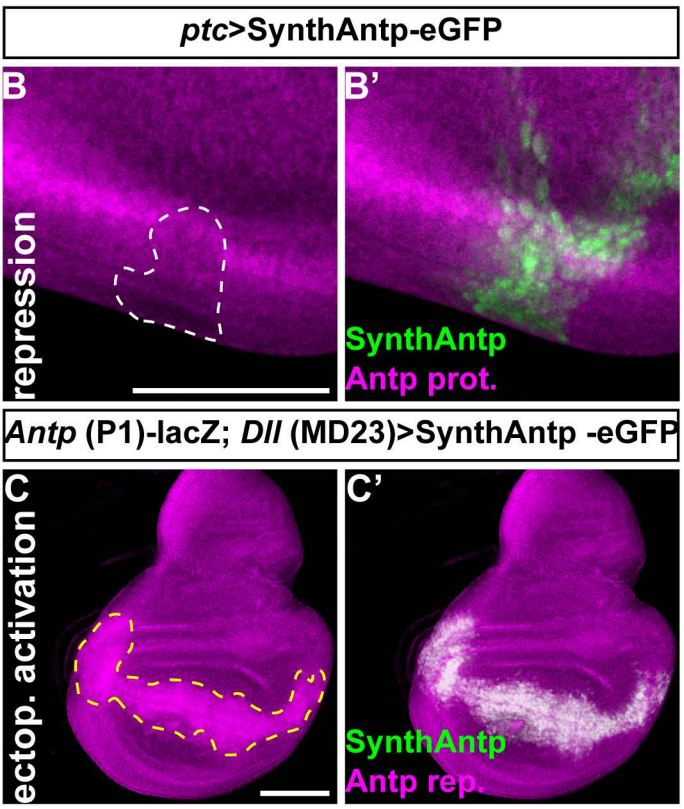

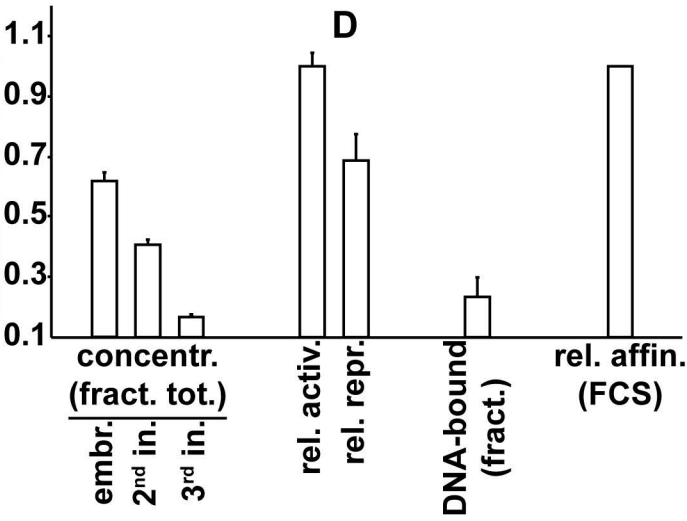

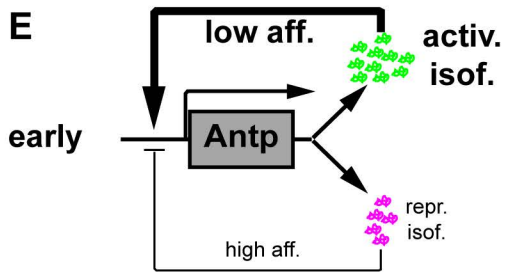

Short linker isoform (preferential repressor)

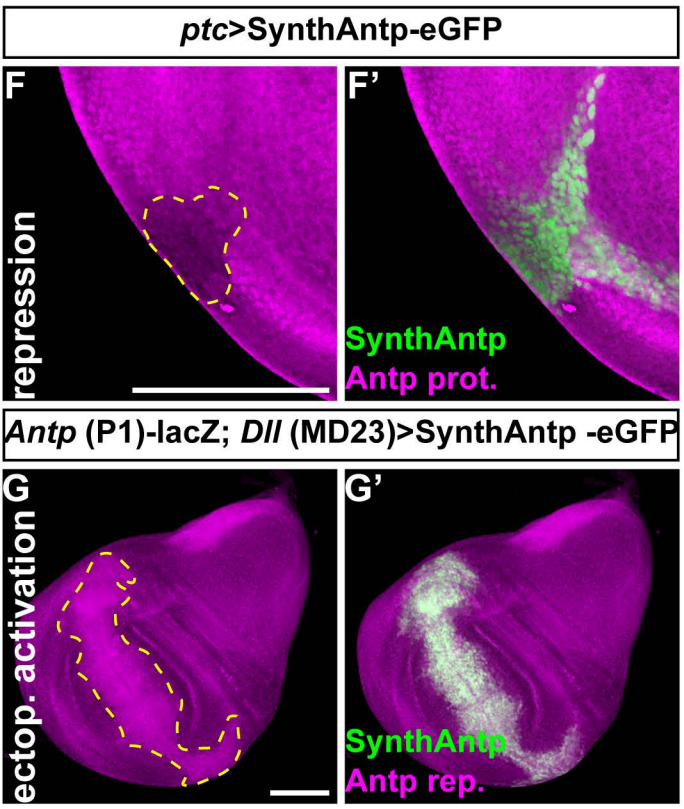

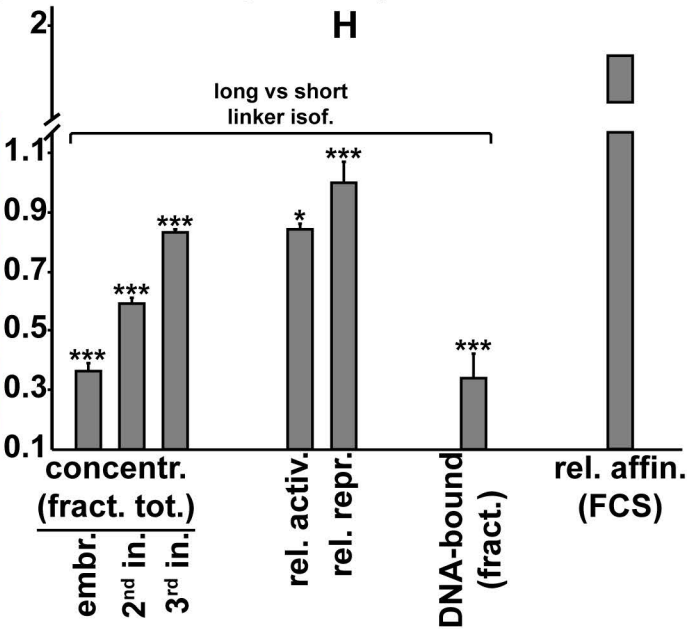

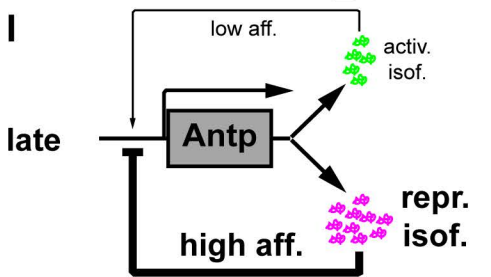

Figure 5

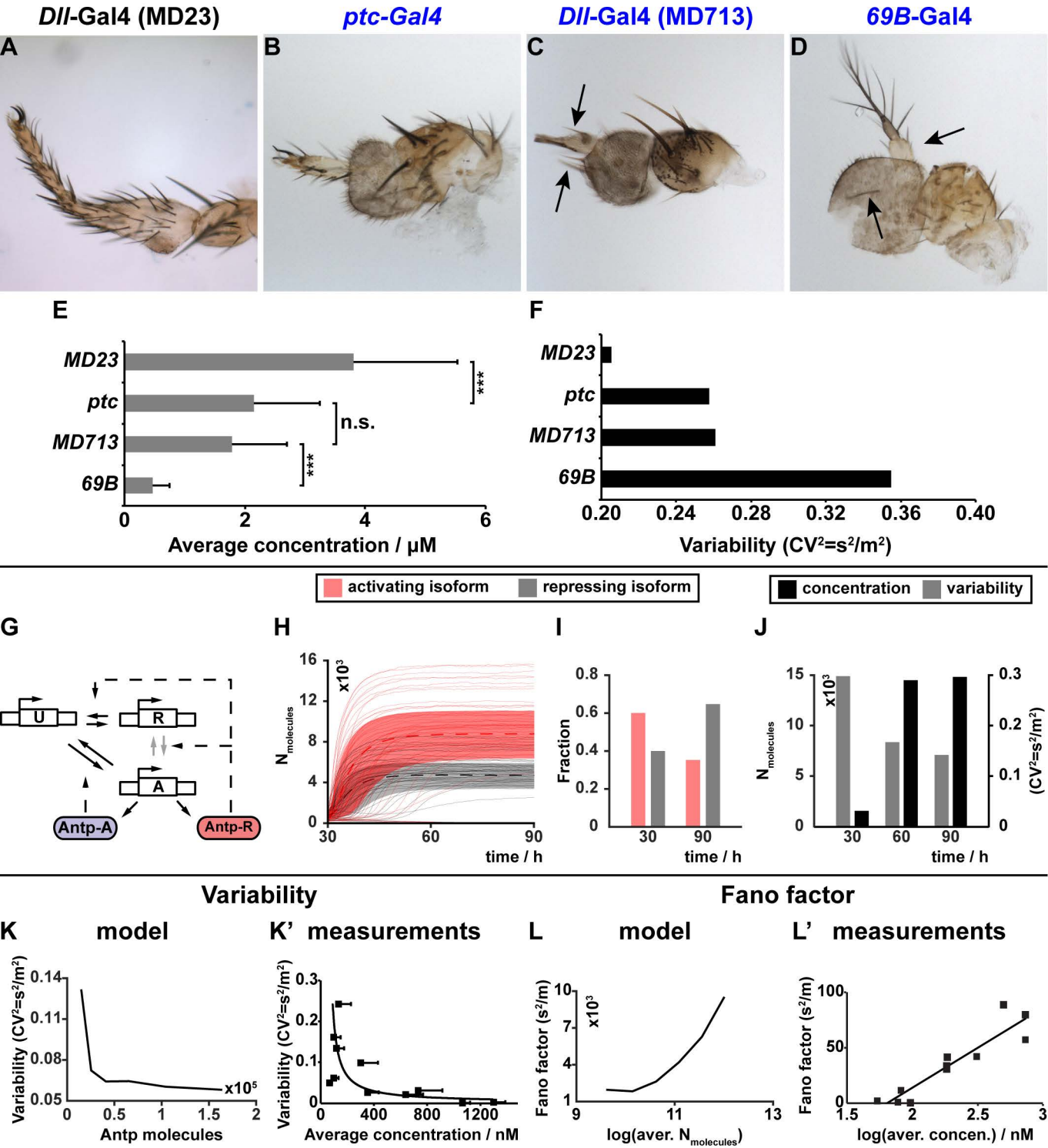
Dll-Gal4 (MD23)
ptc-Gal4
Dll-Gal4 (MD713)
69B-Gal4
A
B
C
D
E
MD23
ptc
MD713
69B
***
n.s.
***
0
2
4
6
Average concentration / µM
F
MD23
ptc
MD713
69B
0.20
0.24
0.28
0.32
0.36
0.40
Variability (CV²=s²/m²)
activating isoform
repressing isoform
concentration
variability
G
U
R
A
Antp-A
Antp-R
H
x10³
N molecules
16
12
8
4
0
30
60
90
time / h
I
Fraction
0.8
0.6
0.4
0.2
0
30
90
time / h
J
x10³
N molecules
15
10
5
0
0.3
0.2
0.1
0
(CV²=s²/m²)
30
60
90
time / h
Variability
Fano factor
K
model
Variability (CV²=s²/m²)
0.14
0.11
0.08
0.05
x10⁵
0
0.5
1
1.5
2
Antp molecules
K'
measurements
Variability (CV²=s²/m²)
0.3
0.2
0.1
0
0
400
800
1200
Average concentration / nM
L
model
Fano factor (s²/m)
10
7
4
1
x10³
9
11
13
log(aver. N molecules)
L'
measurements
Fano factor (s²/m)
100
50
0
1.5
2
2.5
3
log(aver. concen.) / nM

Figure 6

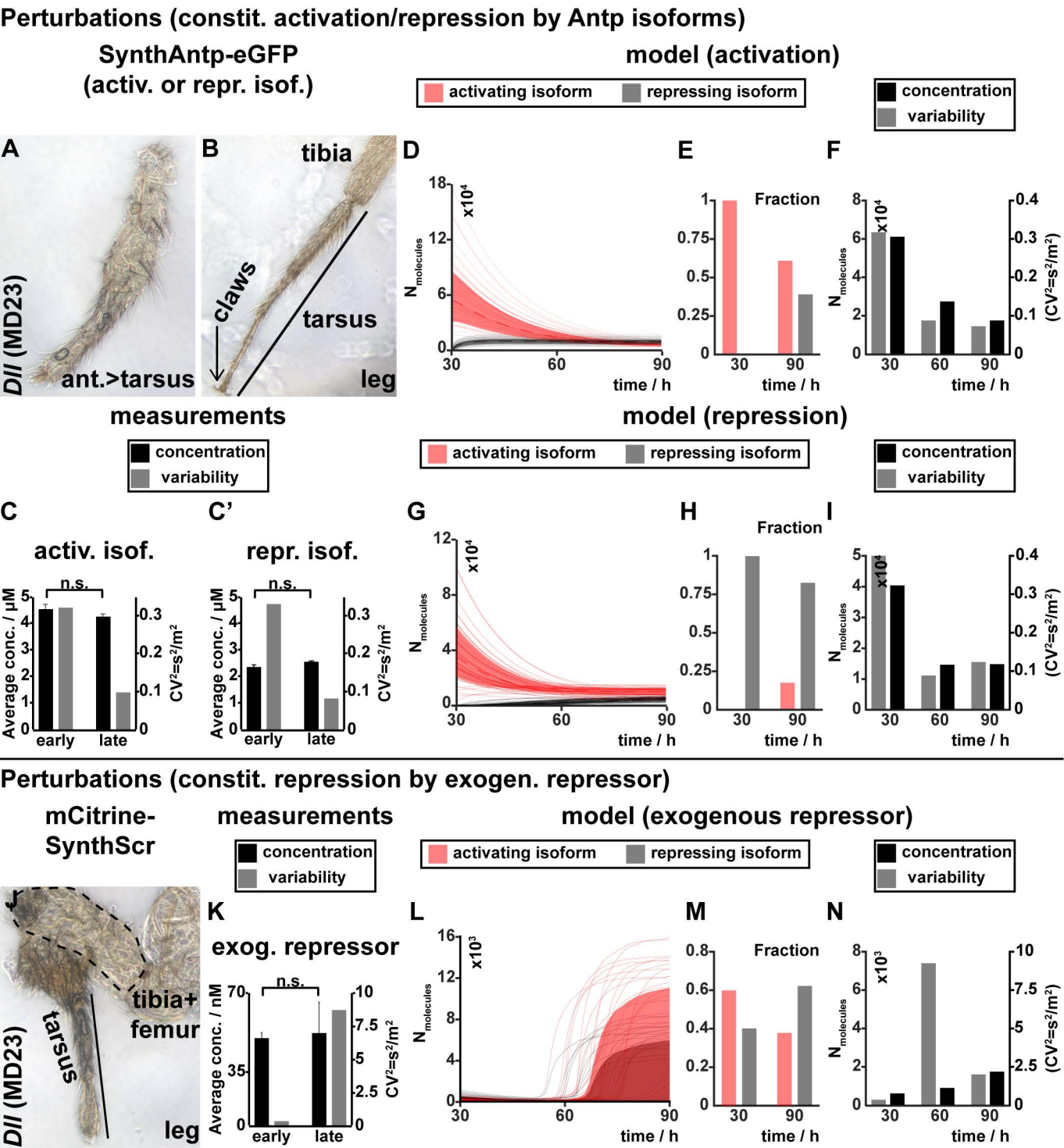
Perturbations (constit. activation/repression by Antp isoforms)
SynthAntp-eGFP
(activ. or repr. isof.)
model (activation)
activating isoform
repressing isoform
concentration
variability
A
B
tibia
claws
tarsus
Dll (MD23)
ant.>tarsus
leg
D
E
F
Fraction
time / h
measurements
model (repression)
C
C'
activ. isof.
repr. isof.
n.s.
Average conc. / µM
early
late
G
H
I
Perturbations (constit. repression by exogen. repressor)
mCitrine-
SynthScr
measurements
model (exogenous repressor)
J
tibia+
femur
tarsus
Dll (MD23)
leg
K
exog. repressor
Average conc. / nM
L
M
N

Supplemental Figure S1

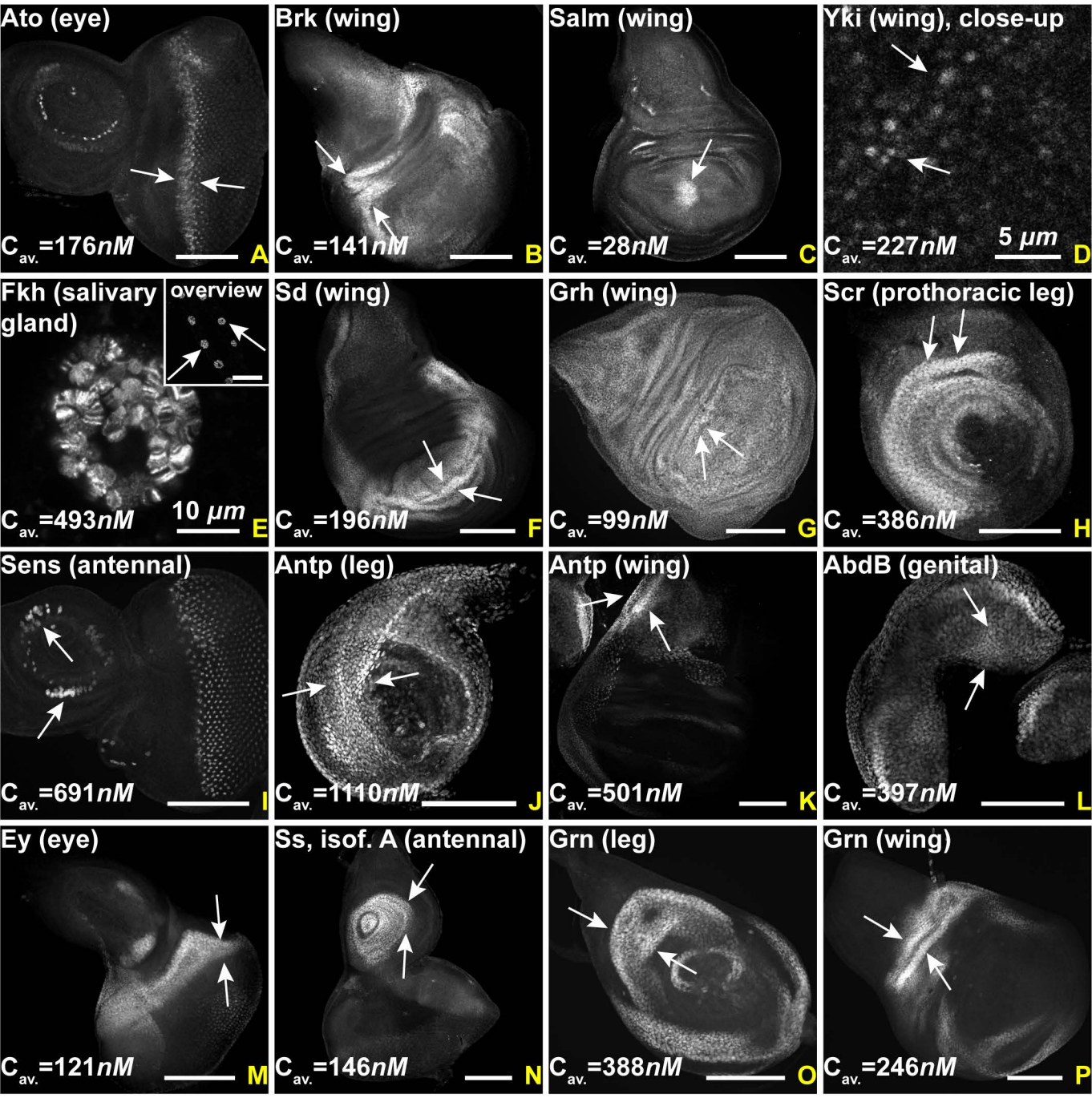

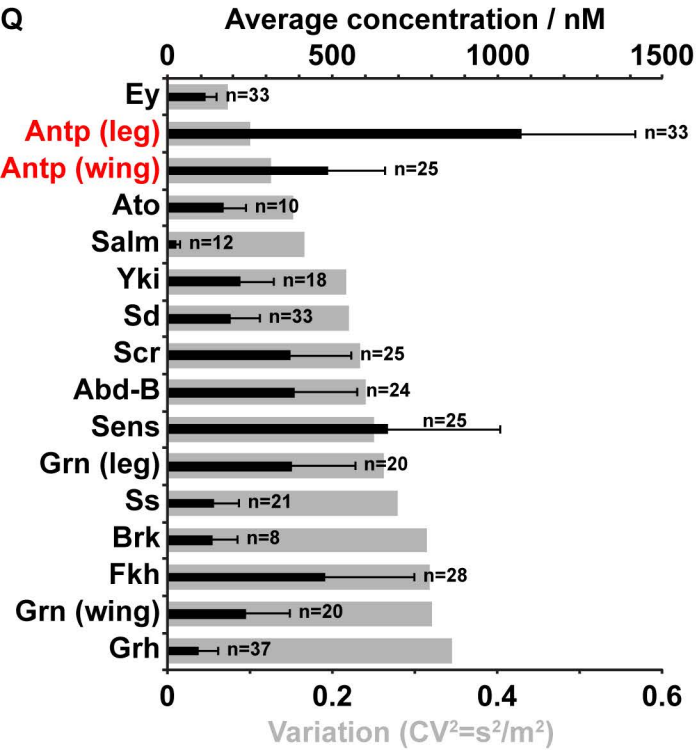

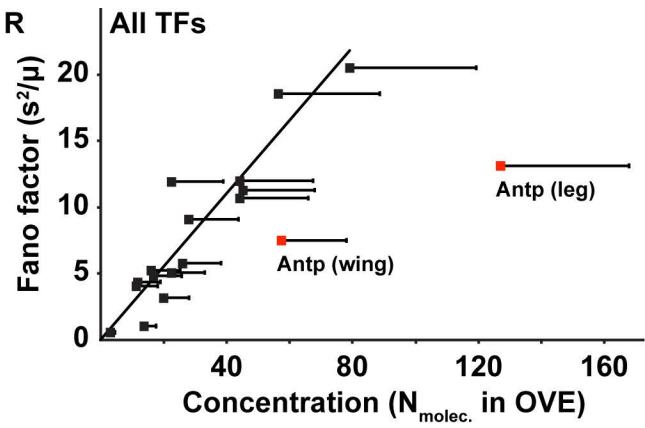

Supplemental Figure S2

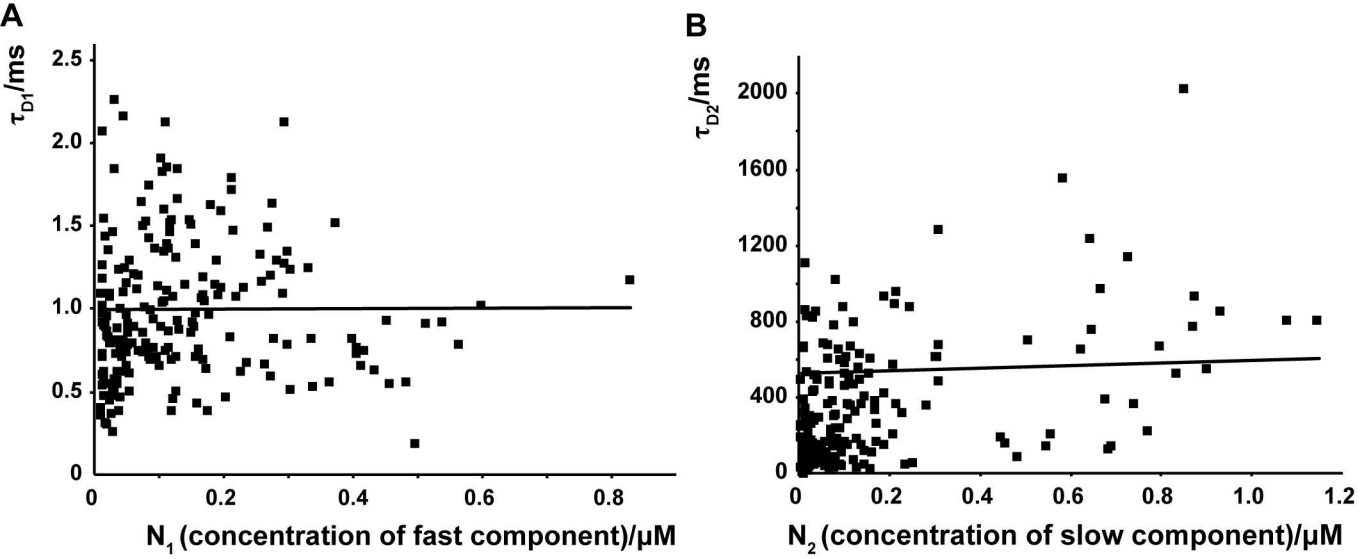

Supplemental Figure S3

Normal expression patterns (P1, P2 reporters and protein)

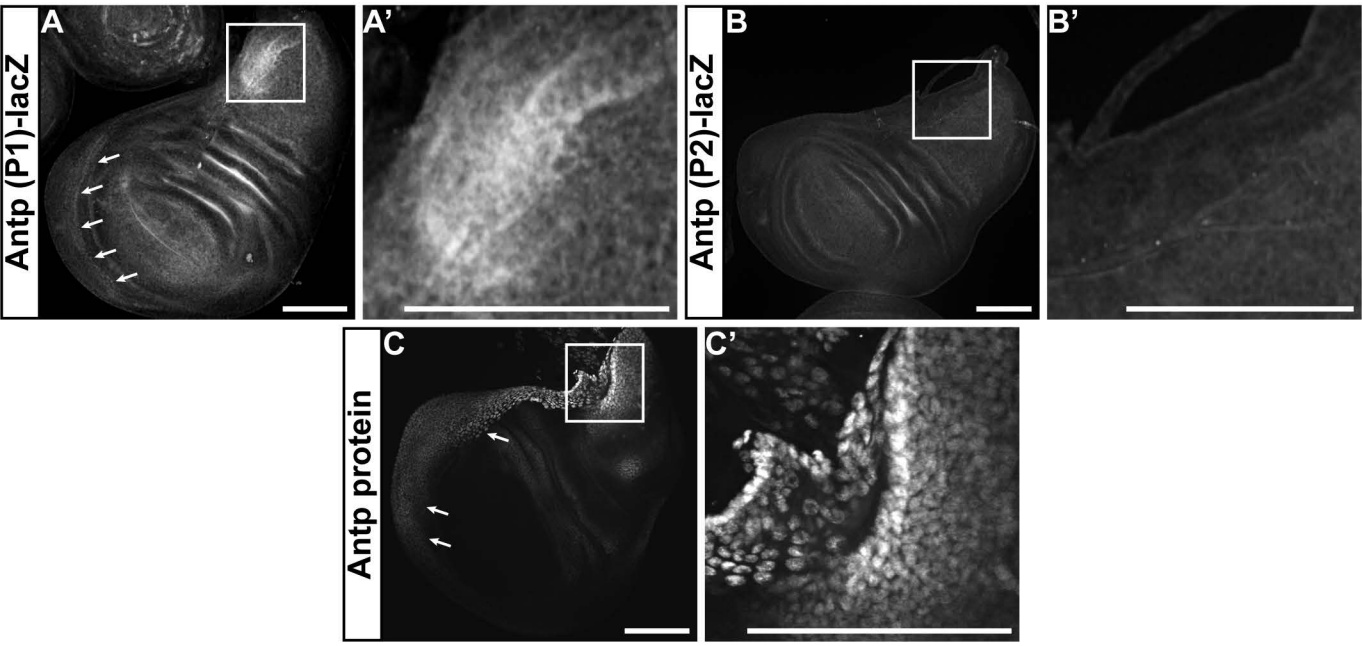

Protein repression (neg. control)

Ay>eGFP

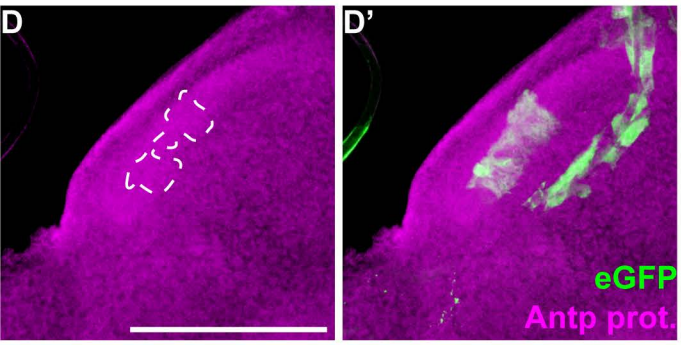

Transcripts repression (neg. control)

Antp (P1)-lacZ, Ay>eGFP

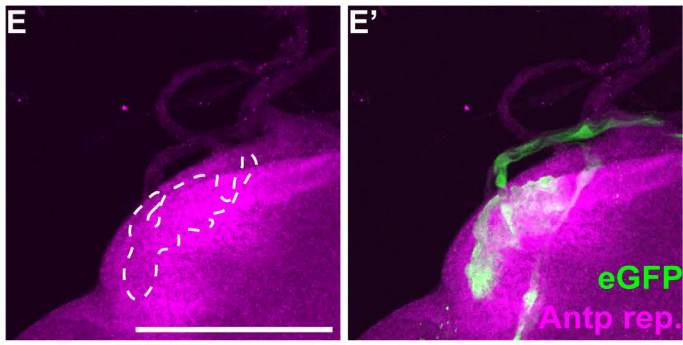

Transcripts repression: Antp-FL

Antp (P1)-lacZ,
Ay>Antp-FL (untagged), eGFP

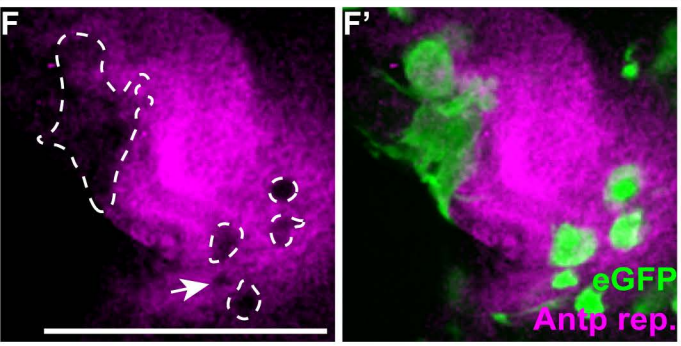

Transcripts activation: Antp-FL

Antp (P1)-lacZ, *Dll* (MD23)>mRFP1 (NLS),
Antp-FL (untagged)

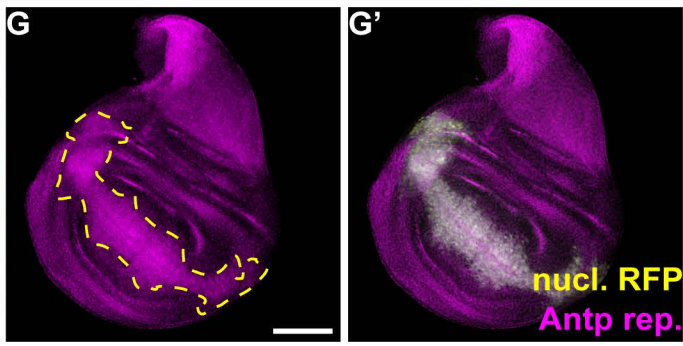

Transcripts activation (neg. control)

Antp (P1)-lacZ, *Dll* (MD23)>mRFP1 (NLS)

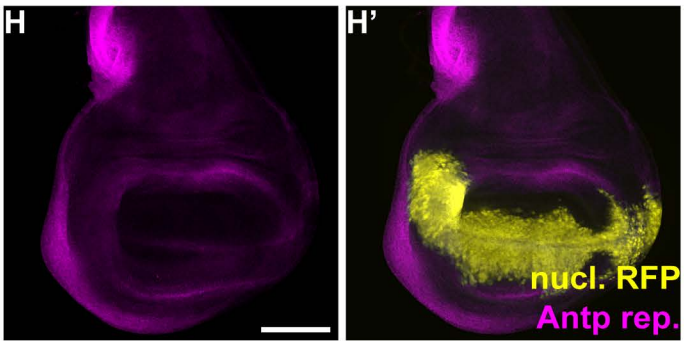

Supplemental Figure S4

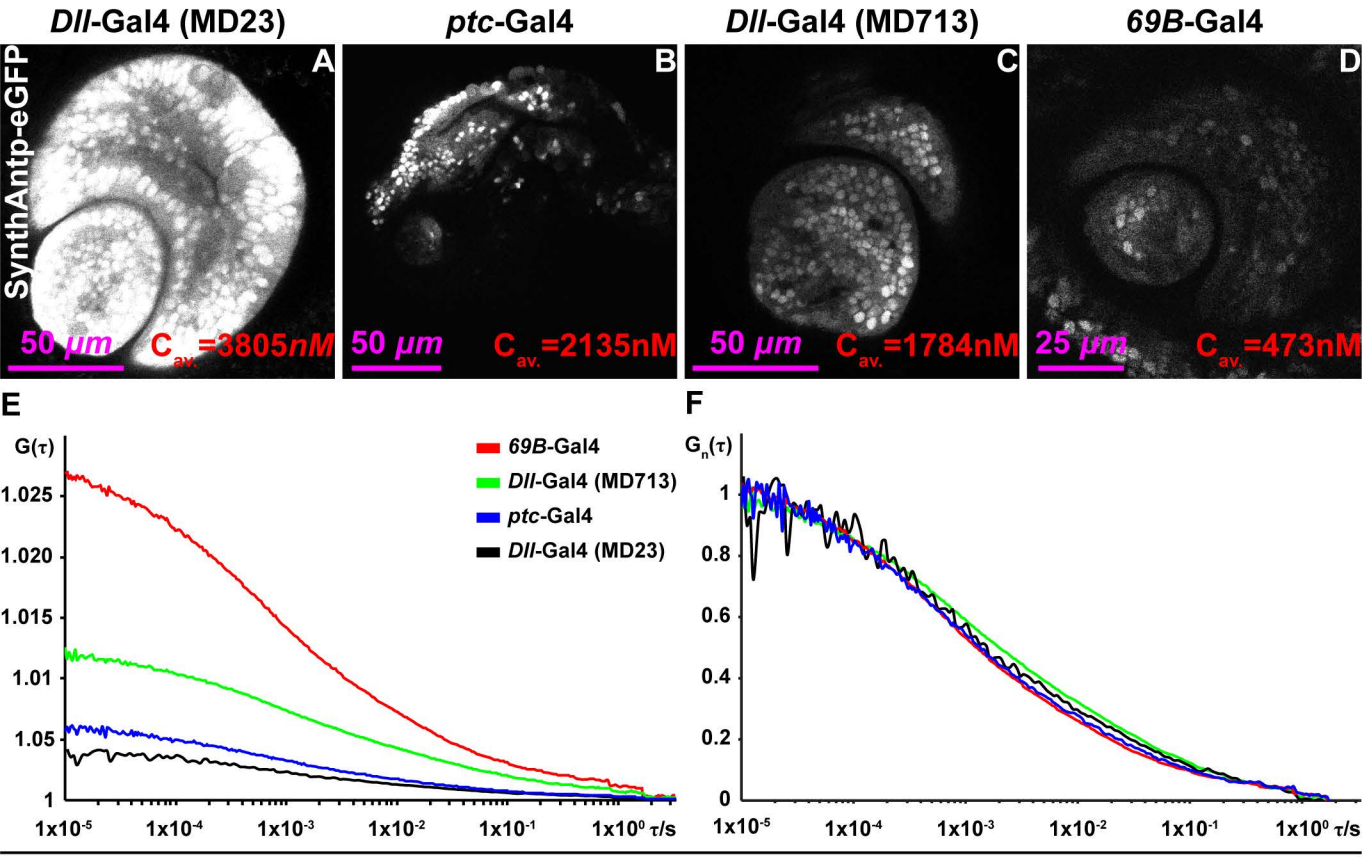

Repression

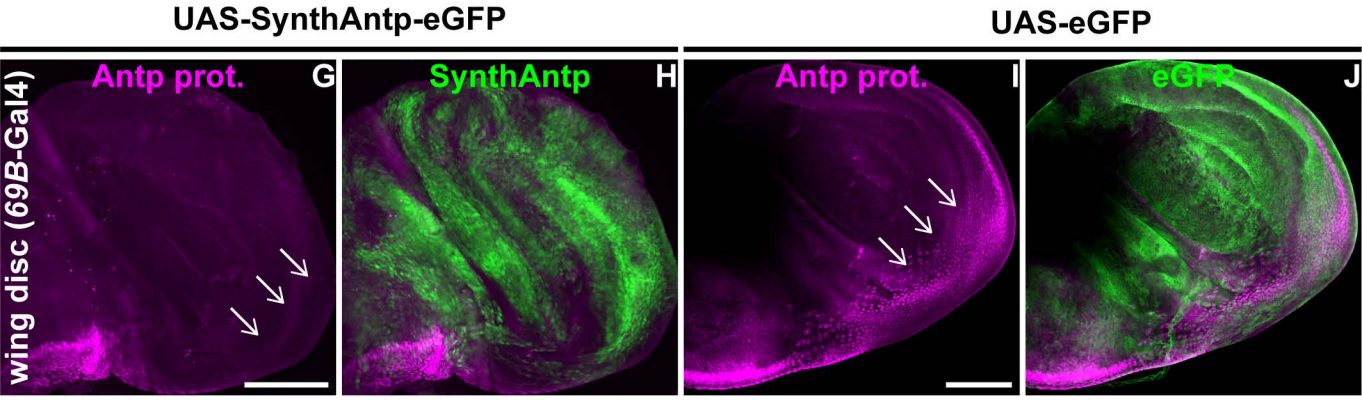

Activation

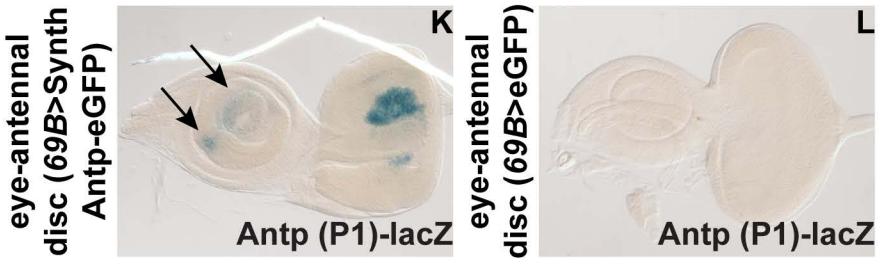

Supplemental Figure S5

Endogenous versus overexpressed

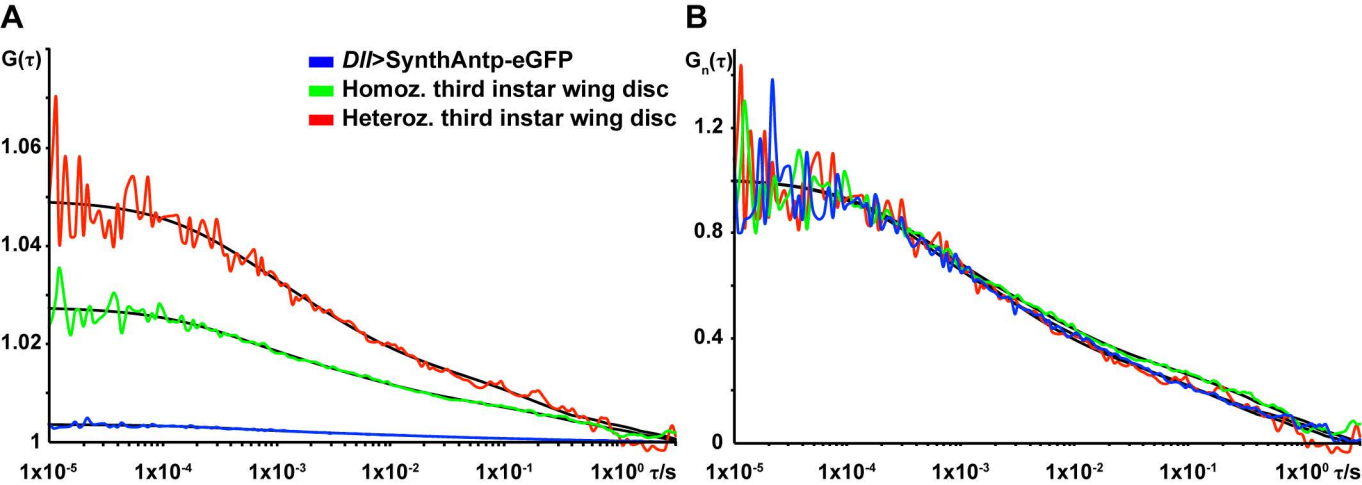

Supplemental Figure S6

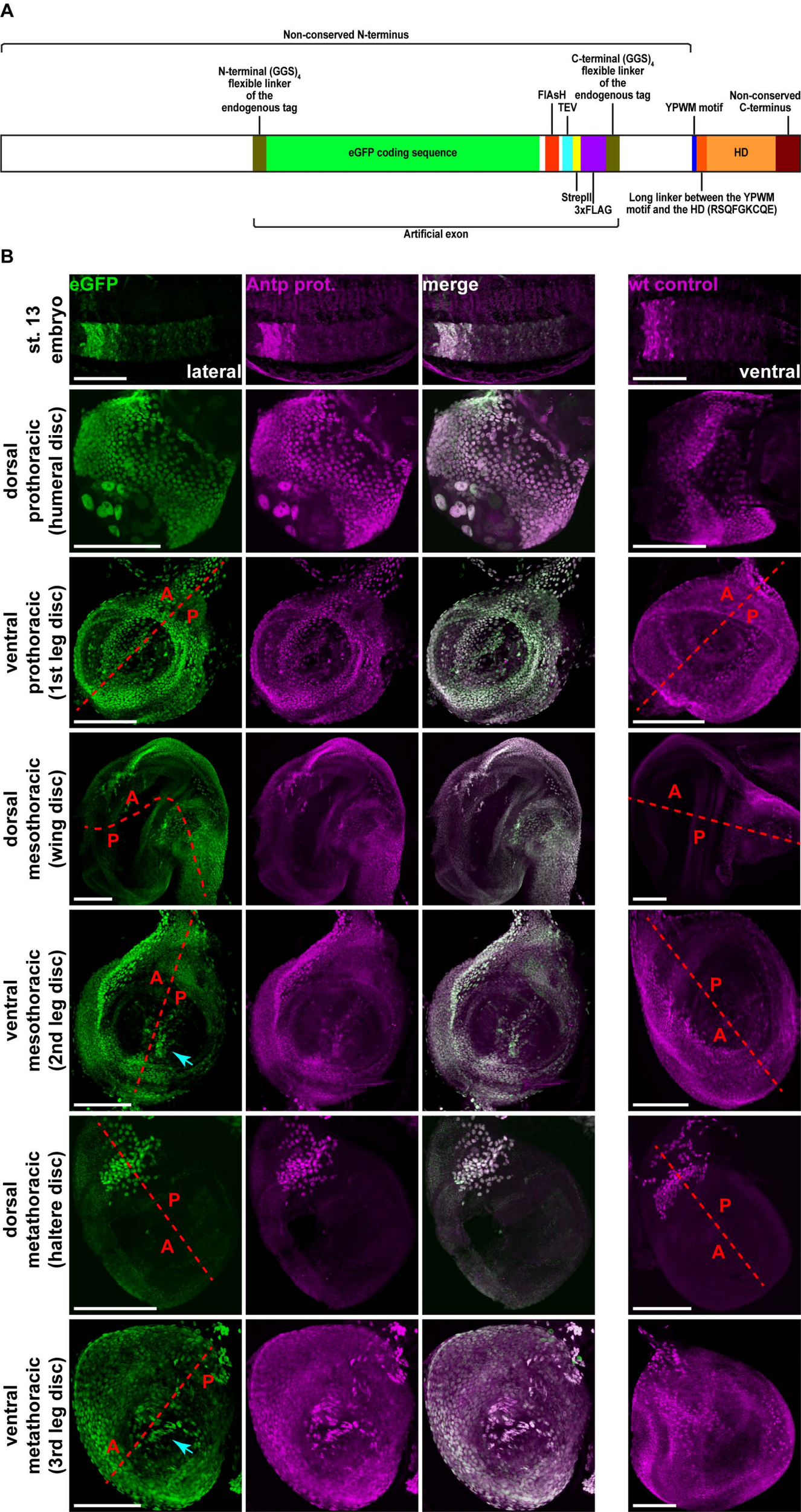

Supplemental Figure S7

Non-induction of overexpression clones

ubi-FRT-mCherry-FRT-Gal4>
Antp-FL (untagged), Antp-eGFP (MiMIC)

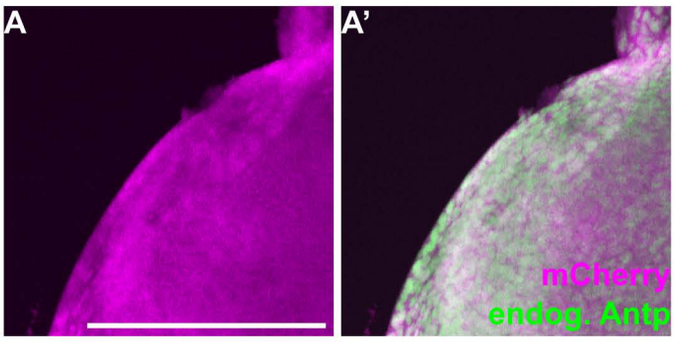

Induction of non-overexpressing clones

Early | Late

ubi-FRT-mCherry-FRT-Gal4, Antp-eGFP (MiMIC)

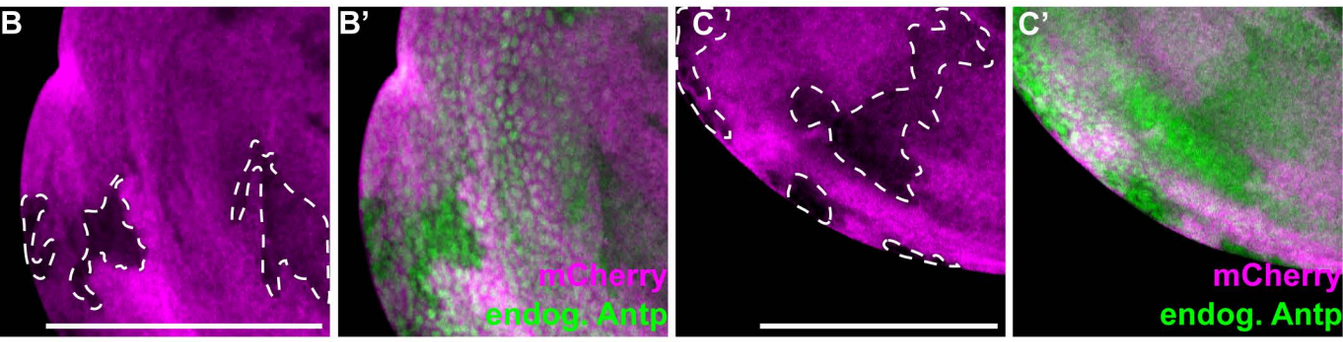

Transcripts activation early

Antp-FL

Antp (P1)-lacZ,
Ay>Antp-FL (untagged), eGFP

SynthAntp

Antp (P1)-lacZ, Ay>SynthAntp-eGFP

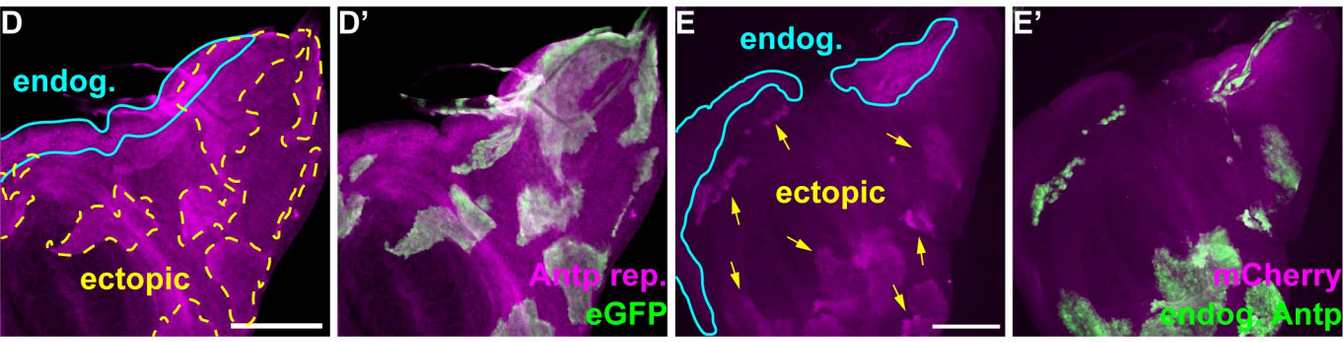

Activation early (neg. control)

Protein

Ay>eGFP

Transcripts

Antp (P1)-lacZ, Ay>eGFP

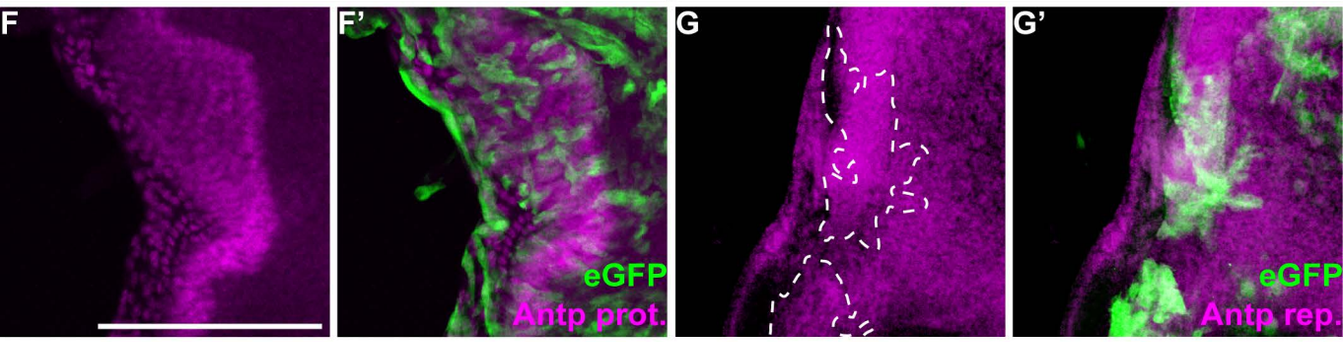

Functionality of the Antp^{RNAi} line

Antp-eGFP (MiMIC); *Ay*>mRFP1 (NLS),
Antp-RNAi

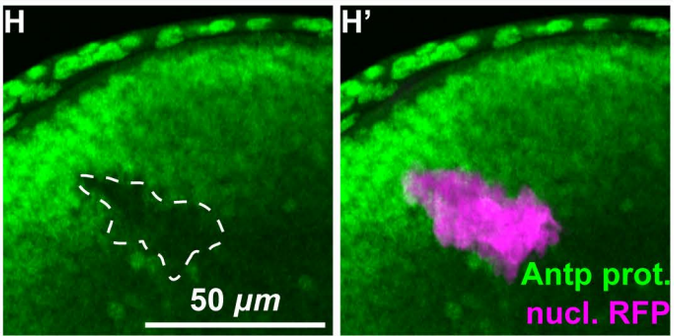

Supplemental Figure S8

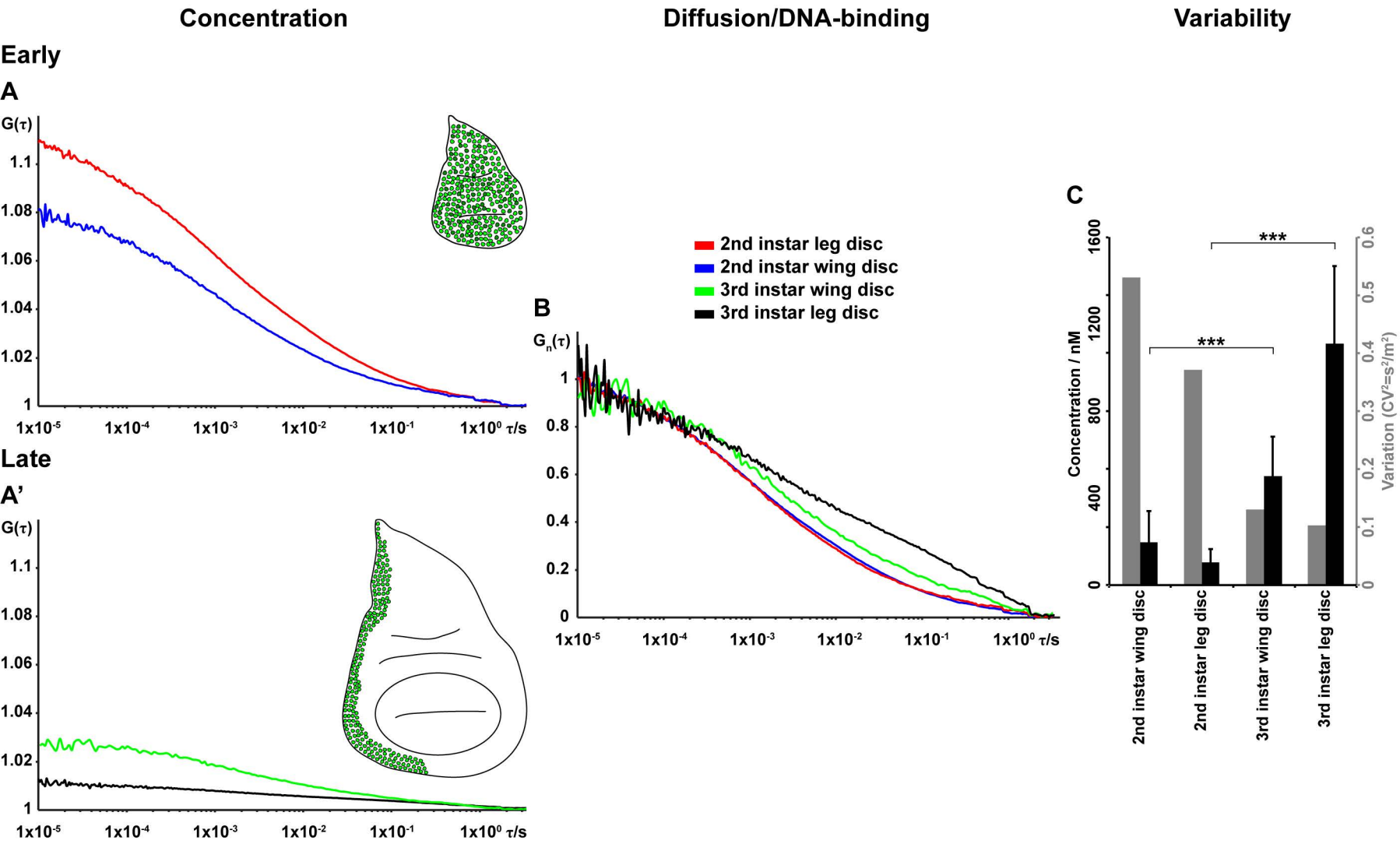

Supplemental Figure S9

Late repression by SynthAntp (short isof.)

Protein

Ay>SynthAntp-eGFP (short isof.)

Transcripts

Antp (P1)-lacZ,
Ay>SynthAntp-eGFP (short isof.)

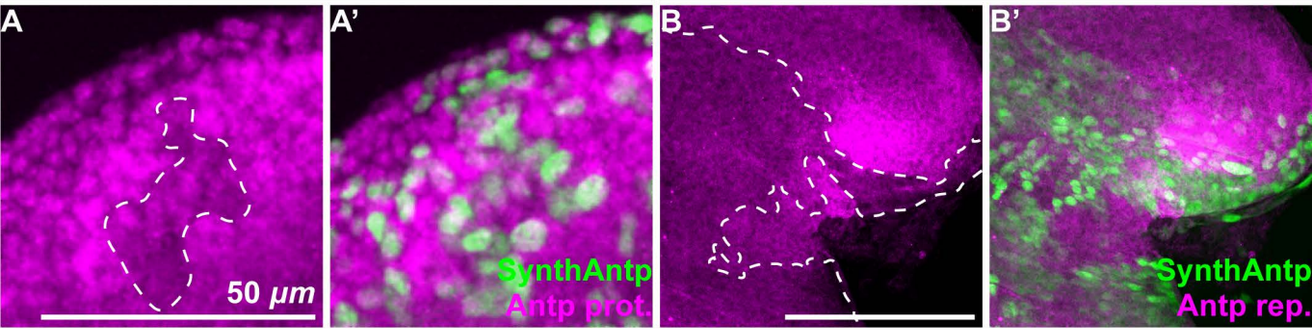

Late repression by Antp-FL (short isof.)

Transcripts

Antp (P1)-lacZ,
Ay>Antp-FL (short isof., untagged), eGFP

Activation by Antp-FL (short isof.)

Transcripts

Antp (P1)-lacZ, *Dll* (MD23)>mRFP1 (NLS),
Antp-FL (short isof., untagged)

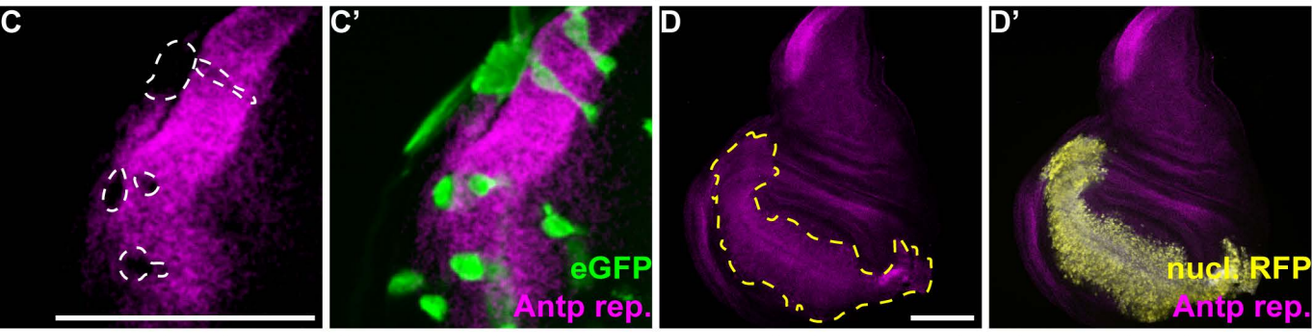

Activation and repression of end. protein by Antp-FL (short isof.)

Early **Late**

ubi-FRT-mCherry-FRT-Gal4>Antp-FL (short isof. untagged), Antp-eGFP (MiMIC)

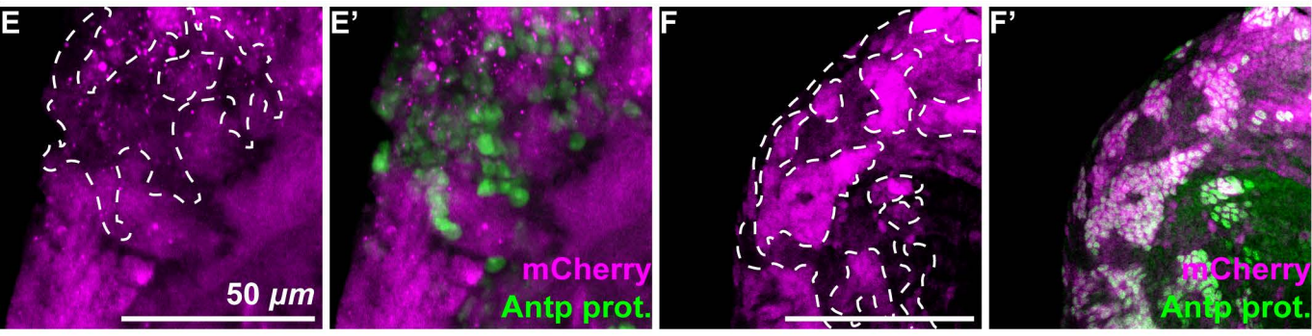

Early activation of transcripts by SynthAntp and Antp-FL (short isof.)

SynthAntp

Antp (P1)-lacZ,
Ay>SynthAntp-eGFP (short isof.)

Antp-FL

Antp (P1)-lacZ,
Ay>Antp-FL (short isof., untagged), eGFP

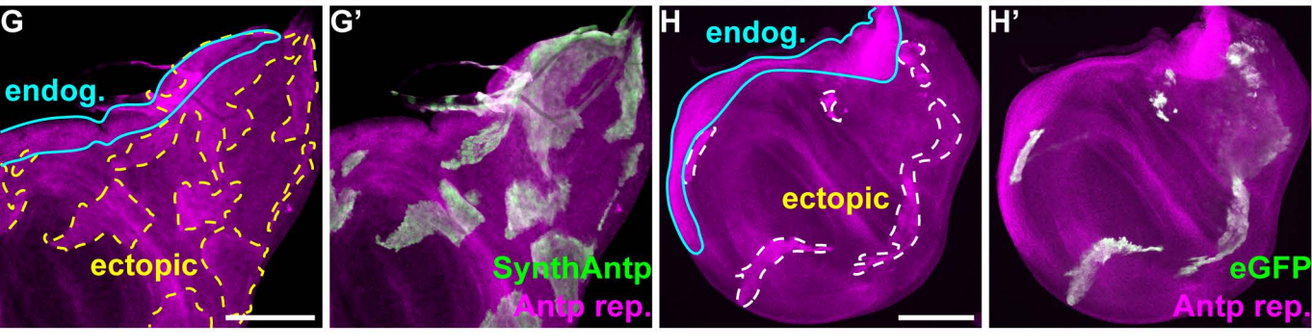

Repression of transcripts by long and short isoforms

Antp (P1)-lacZ,
ptc>SynthAntp-eGFP (long isof.)

Antp (P1)-lacZ,
ptc>SynthAntp-eGFP (short isof.)

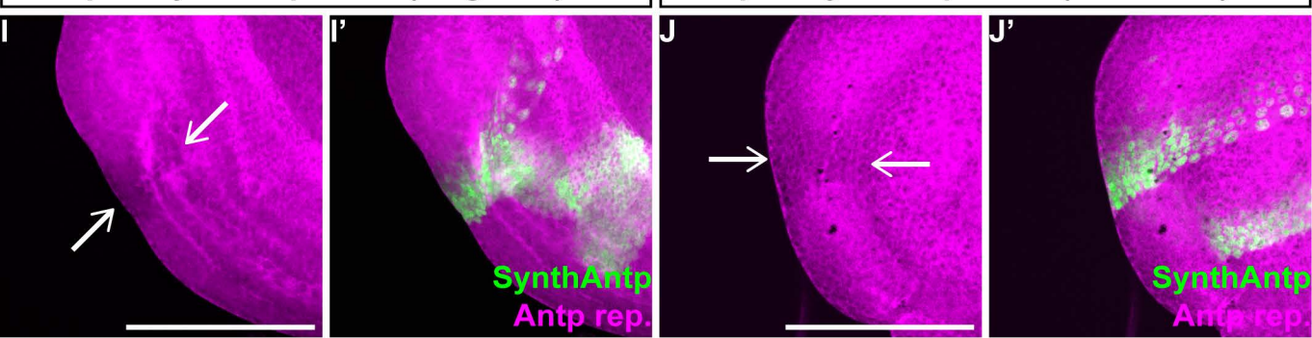

Supplemental Figure S10

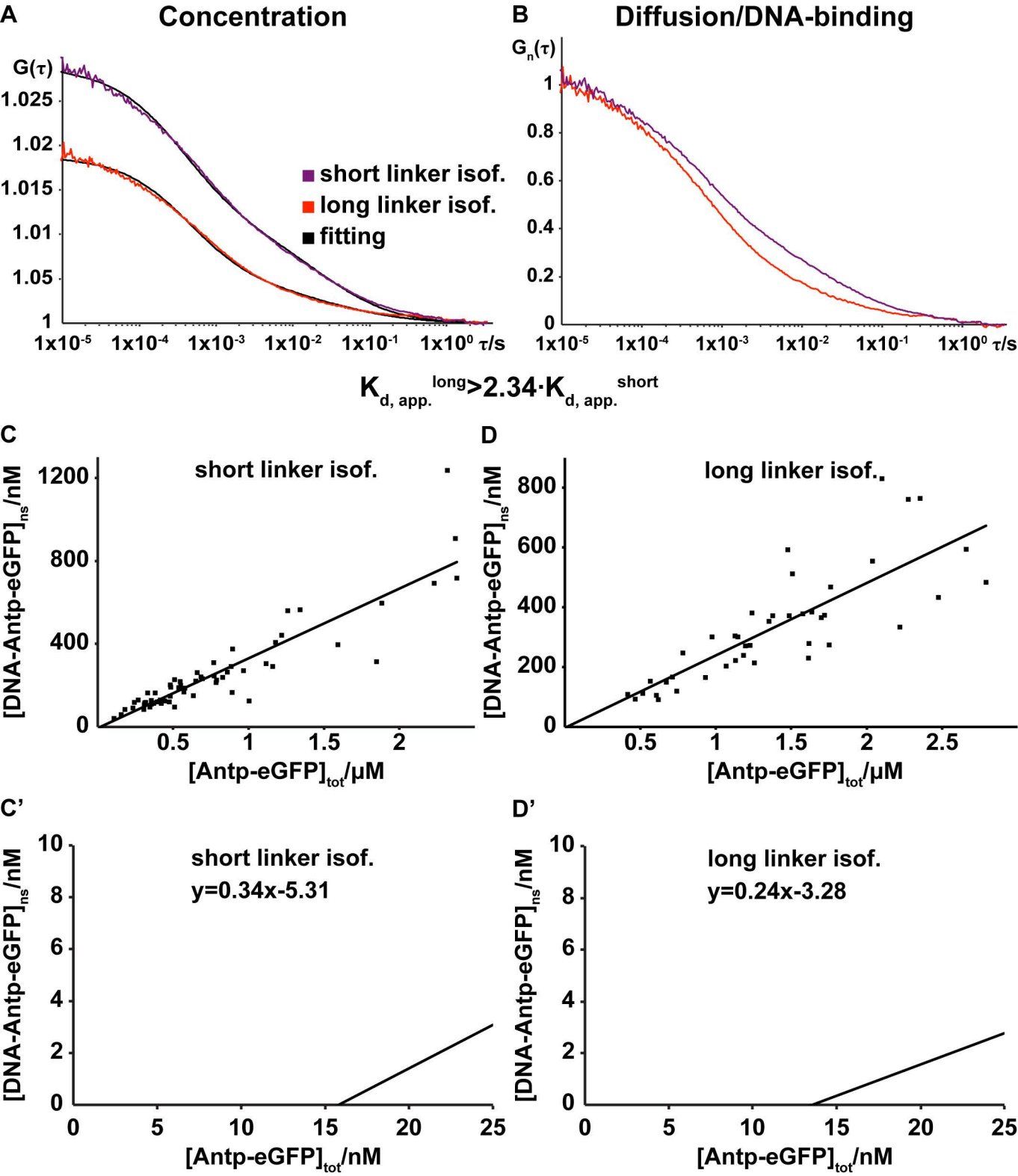

Supplemental Figure S11

***ubi*-mRFP1(NLS), Antp-eGFP (MiMIC)**

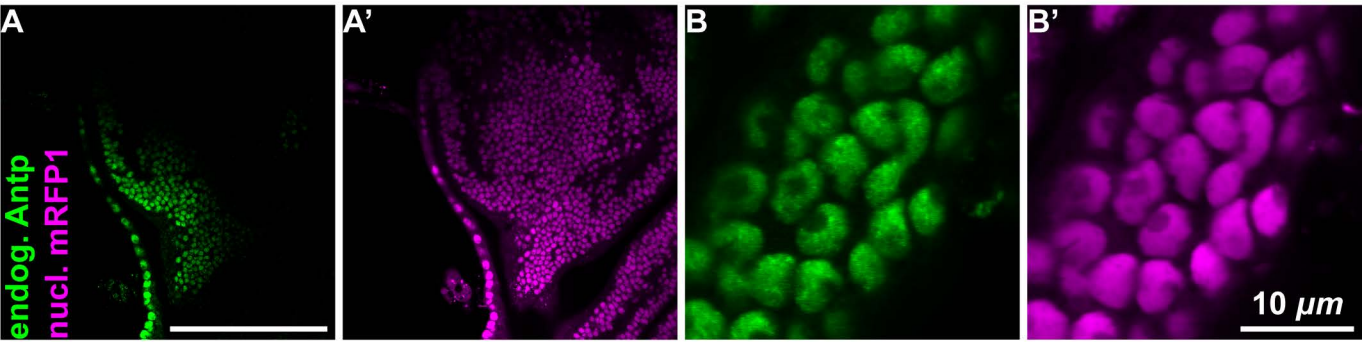

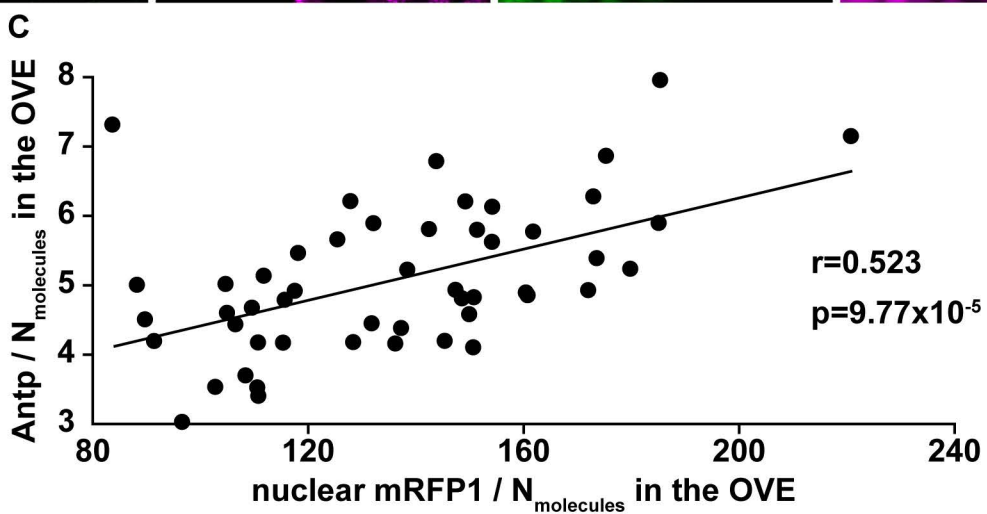

Supplemental Figure S12

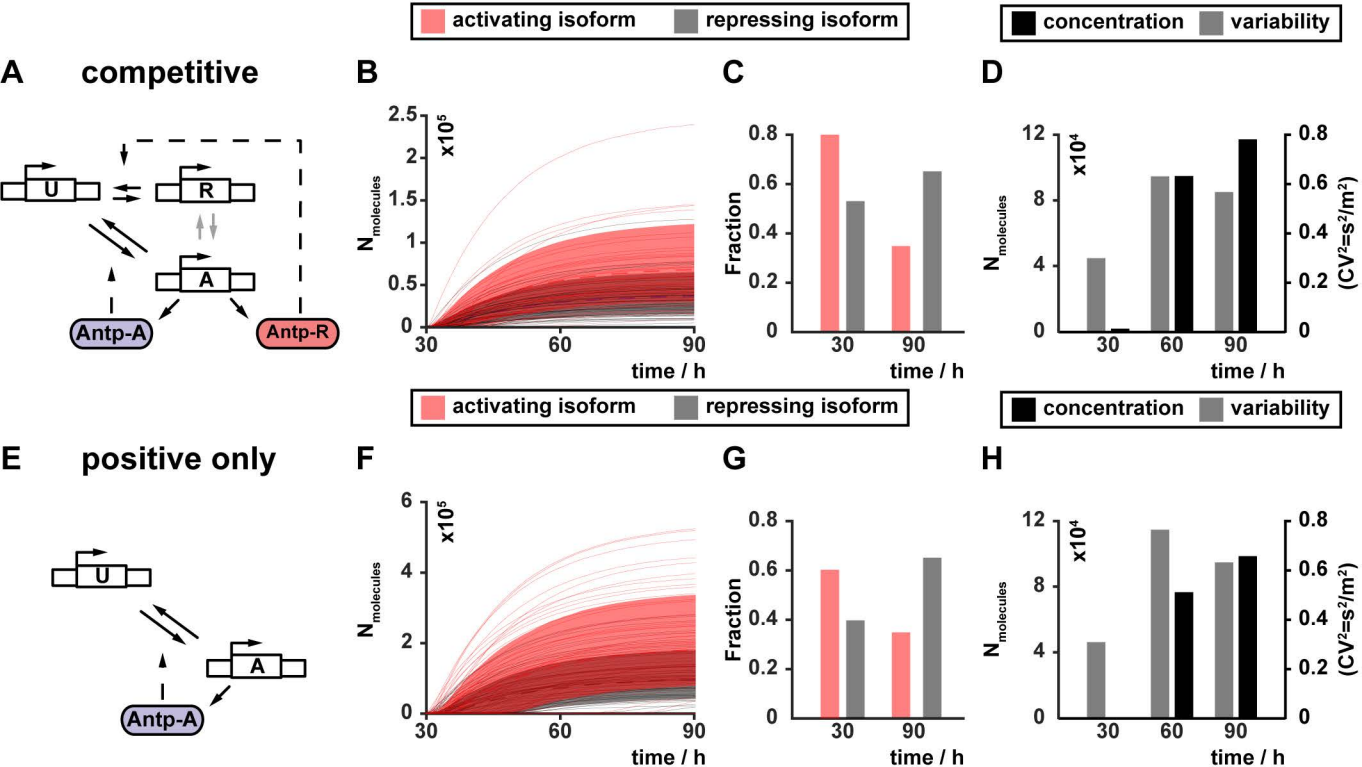
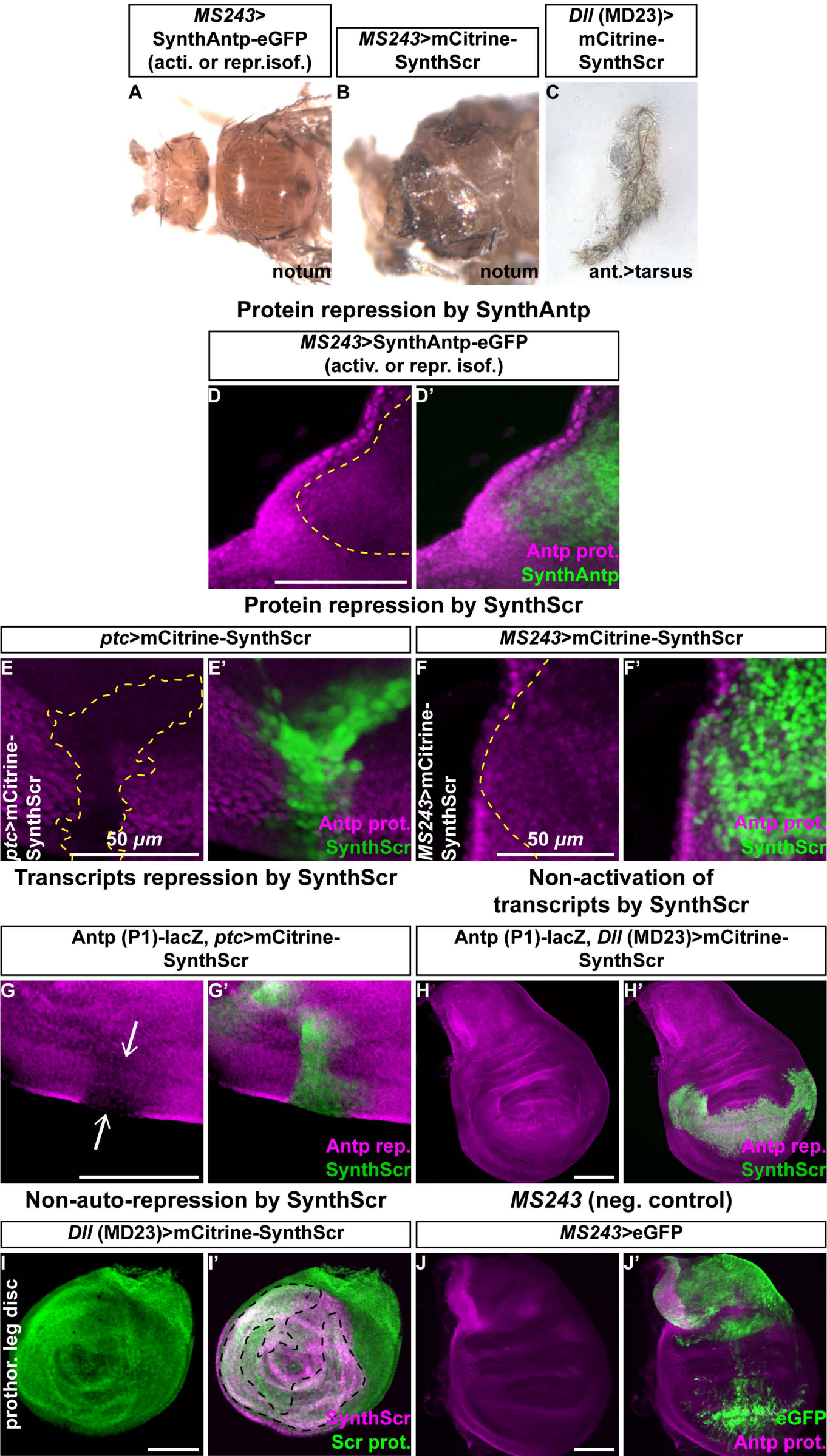
Supplemental Figure S13